IntechOpen

Recent Development in Optoelectronic Devices

Edited by Ruby Srivastava

RECENT DEVELOPMENT IN OPTOELECTRONIC DEVICES

Edited by **Ruby Srivastava**

Recent Development in Optoelectronic Devices
http://dx.doi.org/10.5772/intechopen.72272
Edited by Ruby Srivastava

Contributors

Rajeev Thakur, Gang Liu, Hongwei Tan, Run-Wei Li, J. Hugo García-López, Rider Jaimes-Reátegui, Samuel M. Afanador-Delgado, Ricardo Sevilla-Escoboza, Guillermo Huerta-Cuellar, Didier López-Mancilla, Carlos E. Castañeda-Hernández, Alexander N. Pisarchik, Roger Chiu-Zarate, Alfredo Morales-Sánchez, Mariano Aceves-Mijares, Liliana Palacios, J. Alarcón-Salazar, Alfredo González-Fernández, Hilal Ahmad Reshi, Rayees Zargar, Andreea-Rodica P Sterian (Bobei), Ruby Srivastava

© The Editor(s) and the Author(s) 2018
The rights of the editor(s) and the author(s) have been asserted in accordance with the Copyright, Designs and Patents Act 1988. All rights to the book as a whole are reserved by INTECHOPEN LIMITED. The book as a whole (compilation) cannot be reproduced, distributed or used for commercial or non-commercial purposes without INTECHOPEN LIMITED's written permission. Enquiries concerning the use of the book should be directed to INTECHOPEN LIMITED rights and permissions department (permissions@intechopen.com).
Violations are liable to prosecution under the governing Copyright Law.

Individual chapters of this publication are distributed under the terms of the Creative Commons Attribution 3.0 Unported License which permits commercial use, distribution and reproduction of the individual chapters, provided the original author(s) and source publication are appropriately acknowledged. If so indicated, certain images may not be included under the Creative Commons license. In such cases users will need to obtain permission from the license holder to reproduce the material. More details and guidelines concerning content reuse and adaptation can be foundat http://www.intechopen.com/copyright-policy.html.

Notice

Statements and opinions expressed in the chapters are these of the individual contributors and not necessarily those of the editors or publisher. No responsibility is accepted for the accuracy of information contained in the published chapters. The publisher assumes no responsibility for any damage or injury to persons or property arising out of the use of any materials, instructions, methods or ideas contained in the book.

First published in London, United Kingdom, 2018 by IntechOpen
eBook (PDF) Published by IntechOpen, 2019
IntechOpen is the global imprint of INTECHOPEN LIMITED, registered in England and Wales, registration number: 11086078, The Shard, 25th floor, 32 London Bridge Street
London, SE19SG – United Kingdom
Printed in Croatia

British Library Cataloguing-in-Publication Data
A catalogue record for this book is available from the British Library

Additional hard and PDF copies can be obtained from orders@intechopen.com

Recent Development in Optoelectronic Devices
Edited by Ruby Srivastava

p. cm.

Print ISBN 978-1-78923-602-6

Online ISBN 978-1-78923-603-3

eBook (PDF) ISBN 978-1-83881-672-8

Meet the editor

Dr. Ruby Srivastava, a theoretical physicist, has successfully completed two projects as a principal investigator with CSIR-IICT, Hyderabad, under DST WOS-A scheme. She has worked for 15 years in academics and has contributed several solo author papers and a few book chapters. Her book "Nanostructured Solar Cells" was selected by the Book Citation Index in the Web of Science™ Core Collection (BKCI). One of her publications is rated among the top 1, and another publication was nominated for the Longuet-Higgins Early Career Researcher Prize-2016. As a reviewer to all the leading publishing groups, she is also editing several book projects and is rated among the top 4% of the most read authors by Academia.edu. Her new project will be the theoretical studies on RNA: as an application toward biomedical and green electronics.

Contents

Preface

The authors with whom I have had the pleasure to collaborate have written chapters that report the recent developments in optoelectronics. Specialists from different organizations all over the world have contributed to this book. The latest technological developments have been covered, including the monolithically integrable Si-compatible light sources, multifunctional optoelectronic device based on resistive switching effects, nonlinear dynamics in optoelectronics structures with quantum well, screen printed ZnCdO films for optoelectronic applications, infrared sensors for autonomous vehicles, experimental and numerical study of an optoelectronics flexible logic gate using a chaotic-doped fiber laser, and Perovskite solar cells: the challenging issue for stable power conversion efficiency.

A brief discussion about the chapters is given here.

The introductory chapter is related to the theoretical analysis of iridium complexes as Organic Light Emitting Diodes (OLEDs). The theoretical aspects about the device design are given by various calculated parameters. Furthermore, strategies have been developed for novel nanostructured materials and silicon-rich oxide (SRO) electroluminescent devices to make it fully compatible with complementary metal-oxide-semiconductor (CMOS) techniques. The fabrication and characterization of light emitting capacitors (LECs) that use different substrate treatments and various SRO compositions and configurations were also discussed in an elaborated manner. Multifunctional optoelectronic devices developed on resistive switching effects were made to control the resistance states, offering high-performance information detecting, demodulating, processing, and memorizing. Their performance such as photoresponsivity, on/off ratio, and retention was also investigated in the connecting chapter. In one of the chapters, computational software was discussed to study the nonlinear dynamics (using mathematical modeling and numerical simulations) in optoelectronics structures with quantum well. The values of various optical parameters (refraction index, reflectance, and absorption) were optimized to improve the conversion efficiency of the quantum cell solar cell devices. The screen printed technology using semiconductor devices, monolithic ICs, other discrete devices, and thick films themselves has wide applications in televisions, telephones, calculators, automotive electronics, and so on. The results in this chapter indicate that this material might be practically useful for optoelectronic devices, and the novel structure may find utilizations in clean energy environment. Autonomous vehicles are the latest requirement of the automotive industry, where the sensing, processing, activation, feedback, and control functions have been carried out with the help of electronic equipment. The scientists are working hard in this direction to overcome the challenges coming in the way, so that it can become useful to the society bearing all the safety measurements. Another development was related to the study of optoelectronics flexible logic gate in which an experimental setup was made to realize logic operations, taking advantage of the chaotic-doped fiber laser. Interestingly, these fiber lasers have the ability to change the logic gate type by modifying the threshold control parameter. Apart from that, the challenging issues for stable power consumption efficiency related to the improvement of the stability and durability of perovskite solar cells were also discussed. The authors gave the general insights into the photovoltaics technology of metal halide-perovskites and replacement of lead-free perovskite solar cells without degrading its overall performance.

We have tried to maintain a high level technical overview of the emerging technologies on optoelectronics in this book. It is intended as an introduction to the industrial engineers, professionals, high level researchers, and the professionals who have the technical background and also to every individual who wishes to understand the optical phenomena used in the field of electronics.

I acknowledge all the contributing authors from different organizations (universities and industries) for their support. I am very grateful to Ms. Marina Dusevic, Author Service Manager at IntechOpen, for the prompt response to all the queries and immense support at every level. *Thank you so much Marina*. I wish all the collaborators every success in their future research activities. I acknowledge the DST WOS A (SR/WOS A/CS-1005/2014) project and my mentors Dr. K. Bhanuprakash, chief scientist; Dr. G. Narahari Sastry, Head at the Center for Molecular Modeling, CSIR-Indian Institute of Chemical Technology, and Prof. Neeraj Misra, PhD supervisor, University of Lucknow for the support. Foremost, I would like to thank my husband Mr. Amit Mohan, daughter Arghyaa, son Aryan, and my entire family for continuous encouragement and understanding at every stage to complete this book.

The fluorescent journey of optoelectronics is still not yet fully explored!!!

Dr. Ruby Srivastava
DST Scientist, CMM
CSIR-Indian Institute of Chemical Technology
Hyderabad, India

Section 1

Light Emitters

Introductory Chapter: Iridium Complexes as Organic Light Emitting Diodes (OLEDs): A Theoretical Analysis

Ruby Srivastava

Additional information is available at the end of the chapter

http://dx.doi.org/10.5772/intechopen.78398

1. Introduction

A specific discipline of electronics, which focus on light-emitting or light-detecting devices, the term "Optoelectronics" is used in the broader perspective. Such devices include those that emit light (LEDs and light bulbs), channel light (fiber optic cables), detect light (photodiodes and photoresistors), or are controlled by light (optoisolators and phototransistors). An interesting combination of electronics and optics, Optoelectronics find varied applications in telecommunications, military services, medical field, solid state devices (sensors, IR emitters, and laser emitters), and automatic control systems. The other counterparts as photo resistors and photovoltaic devices are also used for various applications. Nowadays, photodetectors has confronted significant challenges regarding the realization of efficient and sensitive detection with low-noise for the ultraviolet (UV), visible, and infrared regimes of electromagnetic spectrum.

Cyclometalated Ir(III) complexes are used as the organic light emitting diode (OLED) phosphors due to the phosphorescent emission, which spans the whole visible spectrum. These complexes are the most effective and tunable phosphorescent material for OLED devices due to their higher internal quantum efficiency compared to the fluorescent ones (3, 1) [1, 2]. These complexes can be used as photocatalysts for CO_2 reduction, catalysts for chemical reactions. Biological reagents and photo-oxidants: Few parameters which can lead to the success of these complexes are emission, color tunability, stability, strong spin-orbit coupling, triplet quantum yield, and efficiency toward the radiative transitions. Studies on the homoleptic and heteroleptic iridium complexes are carried out in the absorption spectrum, which lies in the UV-visible region (**Figure 1**).

The synthesis and photophysics of Ir(III) complexes have been of great interest as OLEDs as these complexes represent the most effective, tunable, and sublimable phosphorescent materials.

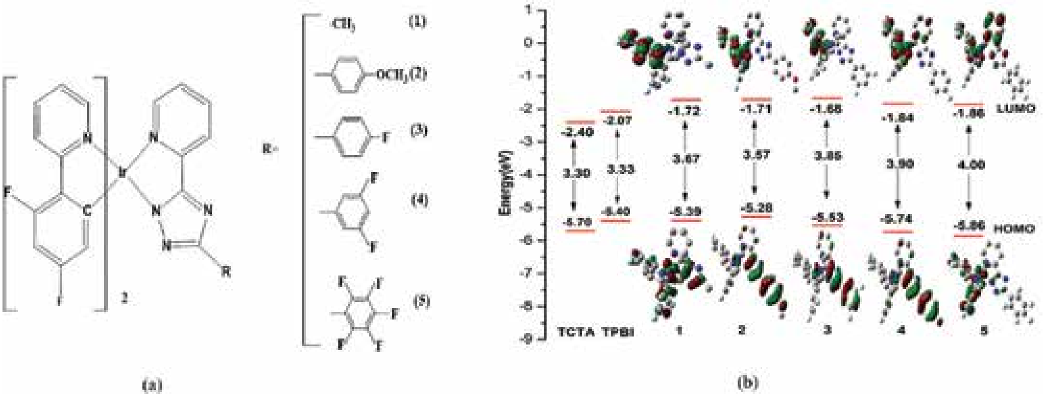

Figure 1. (a) Illustration of five Ir complexes and (b) a pictorial representation of energy highest occupied molecular orbital (HOMO), lowest unoccupied molecular orbital (LUMO) of the given complexes along with the host materials (Tris(4-carbazoyl-9-ylphenyl)amine (TCTA) and 2,2′,2″-1,3,5-Tris(1-phenyl-1H-benzimidazol- 2-yl)benzene (TPBI)).

OLEDs are also utilized as sensors, probes, imaging agents, and photosensitizers for electron and energy transfer. Till now the fabrication of red and green emitting Ir(III) complexes have been successfully fabricated with high-quantum efficiencies, but achieving phosphorescence with high-quantum efficiency for blue light emitting OLEDs is still a challenge. Therefore, several strategies have been developed on how to shift the emission to a blue color. Apart from experimental results theoretical results have been taken to measure the efficiency of blue OLEDs by computational methodologies. Therefore, here we will discuss the theoretical methodology used in design complexes to predict the blue color.

2. Theoretical measurements

The theoretical measures are initialed by the geometrical stability of the electronic structures of these complexes, the nature-type as well as the percentage molecular orbital contributions from the different ligands, absorption spectra in solvent, and the evaluation of excited state lifetimes. Later on, evaluation of the spin-orbital coupling (SOC) matrix element and the predictive measurements are used to calculate the radiative rate constant k_r, and lastly the phosphorescent properties and the better performance of the OLED are discussed, which include the charge injection/transport and balance ability, the energy transfer rate, and triplet exciton confinement for host and guest materials [3]. In some design complexes, two host materials are also suggested for device structure comparing their triplet energies and charge transport properties for the studied guest complexes [4] (**Figure 2**).

The ionization potential (IP), electron affinity (EA), hole extraction potential (HEP), electron extraction potential (EEP), reorganization energy (λ), and HOMO-LUMO gap (HL) HOMO (highest occupied molecular orbital) and LUMO (lowest unoccupied molecular orbital) are calculated by Gaussian and ADF software. The basis sets and functional are used as per requirements of the design complexes.

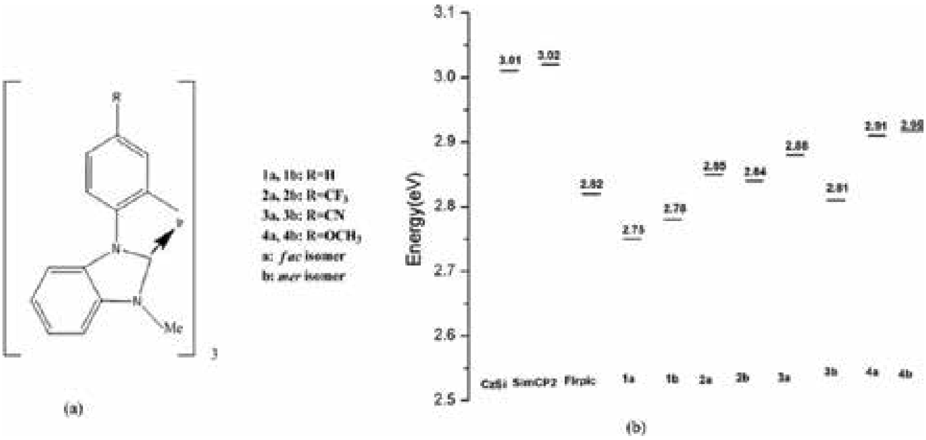

Figure 2. (a) Illustration of eight Ir complexes and (b) triplet energy representation of the eight complexes along with the triplet energy of host materials (CzSi, SimCP2, and FIrpic).

3. Results

The first step is to look into the ground state electronic structures, as the observed differences in the optoelectronic and photophysical properties depend on the electronic structures. Frontier molecular orbital (FMO) also plays a key role in gaining a better understanding of the optical and chemical properties. A detailed examination of the pertinent orbitals is carried out to see the HOMO and LUMO energies. For the singlet-triplet transitions, it is easy to take the first 10 leading excited states (with CI coefficients) and the first triplet energy states. On the basis of the optimized structures in the excited state, the emission spectra of the considered molecules are investigated. The good performance of an OLED device depends on the charge mobilities and a comparable balance between the hole and electron transport, it is necessary to calculate the charge injection properties as ionization potentials (IPs), electron affinities (EAs), HOMO and LUMO, reorganization energy, hole and electron extraction potentials (HEP, EEP). For the photoluminescent materials, it is anticipated that lower the IP of the emitter, the easier the entrance of holes from the hole-transport layer (HTL) to the emitter, and the higher the EA of the emitter, the easier the entrance of electrons from the electron-transport layer (ETL). Solvent polarization energy (SPE) is also used to estimate the self-trapping energies of charge in the materials, which is the energy due to the structural relaxation. The studies of the guest-host relationship are also important as the efficiency of OLEDs is improved on the basis of these investigations. As iridium phosphors have to be widely spread into the host matrix, a relatively long phosphorescence time for metal complexes can cause a long range of exciton diffusion, which may lead to dominant triplet-triplet annihilation. This will get quenched in the adjacent layers of materials in OLEDs. Here it is to mention that an effective host material is very important to achieve efficient electrophosphorescence. Several other requirements for the effective host material are (a) HOMOs and the LUMOs of the host material should match those of neighboring active layers to lower the device driving voltage and reduce the hole and electron injection barrier. (b) The host should possess higher triplet energies than those of the dopant emitters so as to confine the triplet excitons in the emissive layer and to prevent reverse energy transfer from the guest back to the host. (c) The charge carrier transport properties of the host have to be good and it should balance the hole-electron recombination process. Dexter energy transfer also plays a significant role in obtaining the triplet excitons for the guest materials and the corresponding rate is correlated with the changes in Gibbs free energy (triplet energy difference) based on the Marcus electron-transfer theory.

Thus, we can say that though the OLED development is more of an experimental field than being a theoretically determined science. Nevertheless, the key parameters discussed here can be reliably considered in the theory and this knowledge will surely help in the design and fabrication of new phosphorescent OLEDs.

Acknowledgements

I acknowledge the financial assistance by the DST WOS A project (SR/WOS A/CS-1005/2014). I am also thankful to my Mentor Dr. G. Narahari Sastry, Center for Molecular Modeling, CSIR-Indian Institute of Chemical Technology for the support.

Author details

Ruby Srivastava

Address all correspondence to: amitruby1@gmail.com

CSIR-IICT, Hyderabad, India

References

[1] Srivastava R, Laxmikanth Rao J, Kotamarthi B. Theoretical study of electronic structures and opto-electronic properties of iridium(III) complexes containing benzoxazole derivatives and different ancillary β-diketonate ligands. Computational and Theoretical Chemistry. 2014;**1035**:51-59. DOI: 10.1016/j.comptc.2014.02.026

[2] Srivastava R, Kada Y, Kotamarthi B. Theoretical studies of electronic structures and opto-electronic properties of blue emitting heteroleptic Iridium(III) complexes containing 1,1 dithiolates. Computational and Theoretical Chemistry. 2013;**1009**:35-42. DOI: 10.1016/j.comptc.2012.12.032

[3] Srivastava R, Laxmikanth Rao J. The effect of substituted 1,2,4-triazole moiety on the emission, phosphorescent properties of the blue emitting heteroleptic Iridium(III) complexes and the OLED performance: A theoretical study. Physical Chemistry Chemical Physics. 2014;**16**:17284. DOI: 10.1039/c4cp02368d

[4] Srivastava R. The effect of substituted moiety on the optoelectronic and photophysical properties of tris (phenyl benzimidazolinato) Ir(III) carbene complexes and the OLED performance: A theoretical study. Molecular Physics. 2015;**113**(12):1451-1464. DOI: 10.1080/00268976.2014.1002824

Chapter 2

Monolithically Integrable Si-Compatible Light Sources

Jesús Alarcón-Salazar, Liliana Palacios-Huerta,
Alfredo Abelardo González-Fernández,
Alfredo Morales-Sánchez and
Mariano Aceves-Mijares

Additional information is available at the end of the chapter

http://dx.doi.org/10.5772/intechopen.75116

Abstract

On the road to integrated optical circuits, the light emitting device is considered the bottleneck preventing us from arriving to the fully monolithic photonic system. While the development of silicon photonics keeps building momentum, the indirect bandgap nature of silicon represents a major problem for obtaining an integrated light source. Novel nanostructured materials based on silicon, such as silicon-rich oxide (SRO) containing silicon nanoparticles, present intense luminescence due to quantum phenomena. Using this material, electroluminescent devices have already been fabricated and even integrated in monolithic photonic circuits by fully complementary metal oxide semiconductor (CMOS) compatible techniques, opening the door to seamless electronic and photonic integration. The present work discusses some of the strategies used to improve the performance of SRO-based electroluminescent devices fully compatible with CMOS technology. Results from the characterization of devices obtained using different approaches are presented and compared.

Keywords: silicon-rich oxide, silicon nanoparticles, light emitting capacitor, photonic system, monolithic integration

1. Introduction

There are many research groups devoting their efforts to contribute to the development of a fully integrated photonic lab-on-a-chip (LOC) that can take advantage of the use of silicon (Si) as the main material. These are, among others, large availability and low cost of the material, a very well-established fabrication and testing ecosystem, the existence of a fabless model, very large chip fabrication volumes and yields, the possibility of testing using parallel systems, seamless integration with electronics, etc. All these advantages have driven a significant advancement in the past years regarding the development of Si-based LOC systems and, in particular, in silicon photonics. However, there still are important barriers to overcome that have prevented the transition from research to industrialization.

One of the most important limitations to achieve the goal of a monolithic integrated photonic system is the indirect band gap nature of silicon, which impedes the availability of light sources in the complementary metal oxide semiconductor (CMOS) technology. Aside from the integrated light emitting device, most of the rest of the problems regarding Si photonics have been solved, being its lack virtually of the only thing separating us from making monolithic Si-based LOC technology.

Depending on the application, the light source problem can be tackled in different manners. In the specific case of biophotonic applications where visible light is preferred [1], the silicon-rich oxide (SRO) or off stoichiometric oxide can be used to obtain light emitting capacitors (LECs). The SRO-based LECs emit almost in all the visible light range, and they are totally silicon compatible [2]. In fact, the integration of a light source, waveguide, and a sensor has already been theoretically and experimentally demonstrated using standard CMOS technology [3, 4].

The active material in a LEC is a SRO film, which can be obtained implanting Si ions into thermally grown silicon dioxide or using a variety of chemical vapor deposition (CVD) techniques. One of the most popular of the latter is the low-pressure CVD (LPCVD), which is a simple way to produce SRO with different silicon excesses [5, 6]. SRO-LPCVD is characterized by the ratio R_0, defined as

$$R_0 = \frac{P_{N_2O}}{P_{SiH_4}} \tag{1}$$

where P_{N_2O} and P_{SiH_4} are the partial pressures of the nitrous oxide and silane gases, respectively. Under this equation, $R_0 = 3$ produces SRO films with 17% atomic silicon excess, while $R_0 > 100$ produces stoichiometric oxide. R_0 values between 20 and 30 produce SRO with silicon excess between 4 and 5 at.%, which delivers a luminescent material, but with relatively poor electrical conductivity. On the other hand, SRO with $R_0 = 10$ or less presents a lower light emission and higher conductivity than those of the former.

Aside from the SRO-based LECs, there are very few reports on totally Si-compatible integrated photonic circuits, most of which use reverse biased PN junctions as the light source [7–9]. Other proposed solutions include the use of phosphorus doped germanium heterojunctions [10], the coupling to the photonic circuit of optical fibers pig-tailed to lasers [11], or the hybrid approximation, in which external nonsilicon sources such as III–V reflective semiconductor optical amplifiers (RSOAs) are used [12]. All the previous lack the possibility of taking advantage of the current techniques used for the massive production of silicon-integrated circuits (ICs). Finally, another approach uses the implantation of rare-earth elements into silicon oxide to produce light emission in the infrared communication region [13]. Again, such technique is not compatible with the standard silicon IC technology.

Then, SRO-based LECs present themselves as the most promising solution to a fully IC-compatible integrated photonic circuit including the three basic elements, i.e., emitter, waveguide, and detector, as demonstrated in [4]. However, at this point, they work in the edge of electric breakdown and consume larger power than that needed to comply with IC strict standards. Therefore, SRO-based LECs require new strategies or different approaches to improve their performance.

In this work, we review the fabrication and performance of LECs, fabricated by our research group, that use different substrate treatments and a variety of SRO compositions and configurations, as means of discussing the strategies to improve the behavior of these devices.

2. Experimental procedure

SRO-based LECs were fabricated using different structures and conditions, namely, SRO monolayers on polished Si-wafers, SRO monolayers on textured Si substrates, and SRO multilayers (MLs) with gradual and abrupt silicon excess. For reference, LECs with single SRO films and SRO in a multilayered structure will be labeled as S-LEC and M-LEC, respectively. The standard fabrication process used is completely compatible with the CMOS technology. For textured Si substrates, the reactive ion etching (RIE) process was used. In this process, Ar and SF_6 in proportion of 7:3 and power of 300 W were set to roughening surface during 1 min, resulting in conical structures over the surface with a roughness and peak density of 4.0 ± 0.2 nm and 3.7×10^{10} cm^{-2}, respectively.

SRO films (mono- or multilayers) were deposited at 720°C, on N-type or P-type silicon substrates ((100)-oriented) with low resistivity (between 1 and 10 $\Omega \times$ cm) by LPCVD and using the flow ratio (R_0) between N_2O and SiH_4 to vary the silicon excess. R_0 values of 5, 10, 20, 25, and 30 have been used to obtain different silicon excesses. Subscript of SRO labels indicates the R_0 parameter. After deposition, SRO films were thermally annealed at 1100°C for 3 h in nitrogen atmosphere in order to activate their photoluminescent (PL) emission.

For electrical and electroluminescent studies, metal insulator semiconductor (MIS)-like devices were fabricated. A semitransparent n^+ polycrystalline silicon (poly) gate was deposited onto the SRO film by LPCVD. After a photolithography process step, different shaped gates were defined. The backside contacts were obtained by the evaporation of an aluminum layer with thicknesses between 0.6 and 1 μm. Finally, the devices were thermally annealed at 480°C in forming gas in order to assure ohmic contacts.

The thickness of all samples, including multilayer structures, was measured using a null Gaertner L117 null ellipsometer with a He-Ne laser of 632.8 nm wavelength. PL spectra were obtained using a Horiba Yvon Fluoromax-3 spectrometer at room temperature; all the films were excited with UV radiation. Optical filters were used in order to guarantee the wavelength of the excitation beam. For electrical and electroluminescent studies, a source meter Keithley model 2400 was used. Electroluminescence (EL) spectra were obtained by biasing the devices with a constant DC voltage and measuring the emitted light by means of an optical fiber normally aligned to the poly gate surface and connected to the Fluoromax 3 spectrometer. The optical power from the emitted light was measured with a 1400 IL radiometer connected to an UV-VIS GaAsP detector placed in front of the gate. Images from EL were obtained using a digital photographic camera. More specific details of the different characteristics of the studied LECs are addressed in Sections 3.1–3.3.

3. Results and discussion

3.1. SRO monolayers

This section shows the electro-optical properties of SRO films deposited on N-type silicon substrates using R_0 values of 20 (SRO_{20}) and 30 (SRO_{30}) and thicknesses of 70.1 ± 2.3 and 119.3 ± 4.9 nm, respectively. LECs with square-shaped poly gates of 4 mm^2 area and 400 nm thick were defined. To obtain PL spectra, the SRO samples (without poly gate) were excited using a 290 nm radiation.

The R_0 parameter is determinant in the structural, compositional, electrical, and light emitting characteristics of the SRO [14]. Red and blue electroluminescent devices have been obtained using R_0 = 20 and 30, respectively. **Figure 1** shows PL and EL spectra of S-LEC_{20} and S-LEC_{30}. There, it is possible to see that both samples emit red PL, but changes in the emission wavelength are obtained with electrical stimulation, especially for SRO_{30}, where a blue EL band is observed with the main peak at 468 nm. A long spectral shift, blue shift, of almost ~227 nm is observed between the EL and PL bands of the SRO_{30} films (blue dash line). LECs with SRO_{20} films emit a broad EL spectrum in the red region (713 nm), as observed in **Figure 1**. An additional EL peak of low intensity is also observed at 468 nm. There exists also a blue spectral shift of the EL with respect to the PL spectrum in SRO_{20} films but much smaller, remaining in the red side of the spectrum (red dash line), which could indicate that the same luminescent centers are involved in both luminescence types. In both SROs, the EL emission is bright and

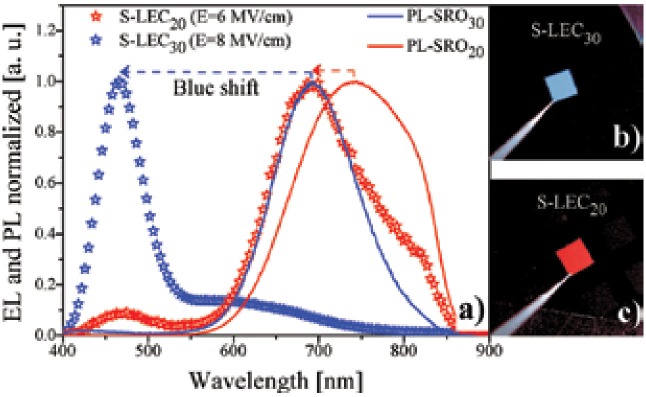

Figure 1. (a) PL (solid line) and EL (symbols) spectra of S-LEC_{20} and S-LEC_{30}. Images of (b) blue (S-LEC_{30}) and (c) red (S-LEC_{20}) bright emission.

observable to the naked eye, as shown in **Figure 1(b)** and **(c)**. Notably, this intense EL is emitted in the whole area of the LEC devices. As expected, the intensity of the full-area emission increases as the applied electric field is increased [15].

Different authors have attributed the spectral shift between PL and EL to three different origins: defects in the SiO_2 matrix, band filling when bipolar injection is achieved, and silicon nanocrystal (Si-nc) size selection by the injected electrons energy [16–18]. In our case, the red EL observed in S-LEC$_{20}$ is ascribed to surface defects on the Si-ncs, which have been observed by transmission electron microscopy (TEM) [14]. While the blue EL in SRO$_{30}$ devices is consistent with the emission related to defects such as oxygen defect centers (ODC), non-bridging oxygen hole centers (NBOHC), and E'_δ centers, which can be either intrinsically present or generated by the electrical stress applied to the SRO matrix [14].

Regarding the electrical behavior, two different electrical behaviors have been obtained from the red and blue LECs. **Figure 2** shows the current density (J) as a function of the electric field (E) of LECs working in accumulation mode (positive bias to the gate).

The S-LEC$_{30}$ shows a high current state (HCS) at low electric fields (<4 MV/cm), followed by a switch by the current to a low conduction state (LCS). Our group has observed this resistive switching (RS) from the HCS to LCS in previous studies and at both forward and reverse biases [14, 15, 19–21]. Such effect was related to the annihilation of conductive paths created by adjacent stable silicon nanoparticles (Si-nps) and unstable silicon nanoclusters (Si-ncls) in which Si-Si bonds can be broken creating some structural changes (defects), including some blue luminescent centers [15, 19, 20]. Recent reports regarding the same electrical switching in SRO films were observed, relating it to the presence of a conductive nanofilament [21–24]. Analysis of TEM imaging showed that the filament is created and annihilated by structural changes due to Joule heating effect produced by the high current flow, which allows the

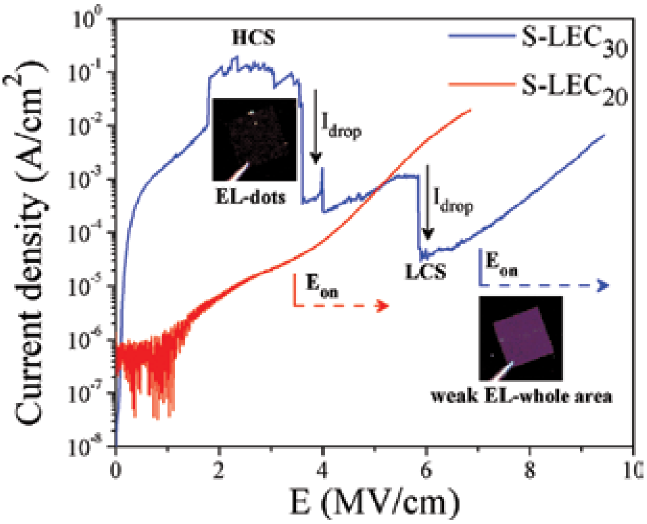

Figure 2. J-E curve from SRO$_{30}$- and SRO$_{20}$-based LECs. Insets are depicting images of EL dots and weak whole area EL.

crystallization (HCS) or amorphization (LCS) of the nanofilament [25]. These observations agree with our asseverations regarding the resistive switching observed in our S-LEC$_{30}$ [24]. During HCS regime, current jumps and drops corresponding to the appearance or disappearance of electroluminescent spots (EL dots) on the LEC surface have been observed (see inset in **Figure 3**) [14, 15, 19, 20]. Once the current fluctuations disappear, through an electrical annealing, the current behavior stabilizes allowing for the whole area EL [2, 14, 19].

On the other hand, the electrical behavior of most of LECs with SRO$_{20}$ films does not show current fluctuations. This effect has been related to the presence of well-separated Si-ncs and observed mainly on samples with a relatively high density of Si-nps [14]. This suggests that a denser network of conductive paths becomes more likely as the Si-ncs density increases, allowing for a uniform charge flow through the whole capacitor area.

In fact, it has been found that the trap-assisted tunneling (TAT) conduction mechanism, through a quasi-continuum of defect traps, predominates in the HCS in the S-LEC$_{30}$ devices, where the trap energy (ϕt) was estimated to be around 1.99 eV [14]. The TAT conduction mechanism has been reported in SRO-based devices where the RS phenomenon has been observed, in agreement with the observation of the devices reported in this work [24]. On the other hand, Poole-Frenkel (P-F) tunneling was found to be the most likely charge transport mechanism in the S-LEC$_{20}$ devices.

Although excellent results have been obtained from light emitting devices based on SRO with Ro = 20 and 30, the turn-on electric field (E$_{on}$) is still higher than desired. As an improvement strategy to obtain devices that emit in a wider range of wavelengths, and at lower E$_{on}$, multilayer structures involving SRO$_{10}$, SRO$_{20}$, and SRO$_{30}$ layers have been designed and fabricated. As it has been shown, both SRO$_{20}$ and SRO$_{30}$ exhibit intense PL. On the other hand, SRO films with higher R$_0$ show lower PL intensity but better conductive characteristics [15, 26]. If the characteristics of each SRO film are preserved in a SRO ML structure, it is possible to improve the charge injection and luminescence properties of SRO-based LECs using the band-gap engineering by the Si-nc size modulation. Under this approach, the composition, structural,

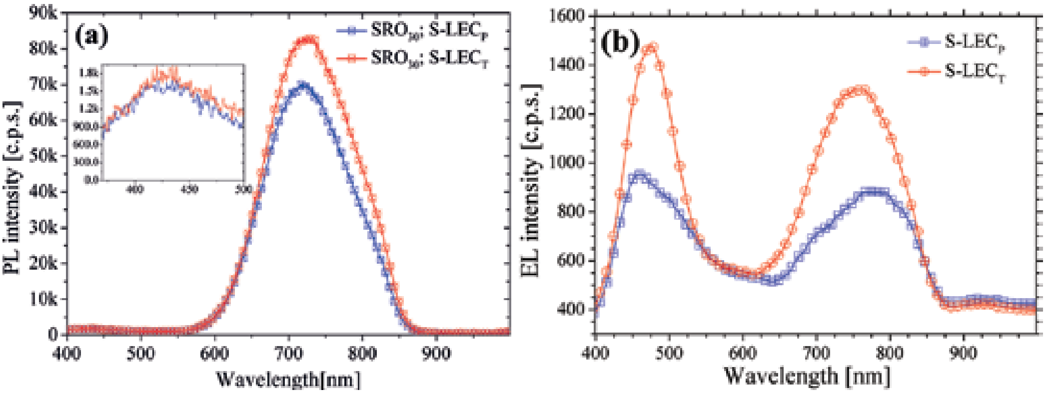

Figure 3. (a) PL spectra from SRO$_{30}$ films of S-LEC$_P$ and S-LEC$_T$. SRO films were excited with λ = 300 nm. (b) EL spectra for S-LEC$_P$ and S-LEC$_T$, when LECs were electrical polarized with 11.5 and 9.8 MV/cm.

and PL emission characteristics of SRO MLs with gradual change of R_0 from 10 to 30, and conversely, have been studied [27]. The Si and O gradual composition profiles in the $SRO_{10–20-30}$ multilayered system have been confirmed by X-ray photoelectron spectroscopy (XPS). The PL emission in these gradual SRO MLs increases when the emissive SRO layers (Ro = 20 and 30) are in the center of the ML. Moreover, the gradual Si-nc size according to the R_0 of each layer was preserved. Nevertheless, the study of the electro-optical characteristics of LECs with such scheme is still being carried out.

3.2. SRO monolayers on textured substrates

To evaluate the performance improvement of LECs on textured substrates (labeled as $S\text{-}LEC_T$), a SRO_{30} film with thickness of about 70 nm was used. The textured process was described in the experimental section. The SRO_{30} film was also deposited on a regular polished substrate, as a reference device, labeled as $S\text{-}LEC_P$. In both cases, the substrate was a P-type silicon wafer with resistivity between 2 and 4 Ω × cm. Over the SRO, a 250-nm thick square gate of poly layer with an area of 1.54 mm^2 was deposited and defined. **Table 1** summarizes characteristics of both S-LECs.

Figure 3(a) shows the PL spectra of the SRO_{30} film present in the S-LECs. Roughening does not appear to significantly affect the emission properties of the active material when it is optically stimulated, as previously demonstrated [28, 29]. As can be observed, there are two peaks, one centered at 725 nm (red band) and a much weaker one at 428 nm (blue band, shown in the inset of **Figure 3(a)**). The emission in blue band is ascribed to non-bridging oxygen defects and oxygen deficiency-related centers [14, 30–34], whereas the red band is attributed to oxygen vacancies caused by the Si excess (720 to 740 nm) [31–33], as well as to interfacial defects in boundaries of silicon nanoclusters with the silicon oxide matrix (810 nm) [35–37].

Figure 3(b) exhibits the EL spectra of the S-LECs. Both LECs show two bands as well: blue and red, as PL. This indicates that PL and EL have the same origin, mainly attributed to SRO-related defects [25, 34, 37]. Since in this case the samples are electrically pumped, electrons are driven through deeper traps, allowing for a larger amount of radiative transitions of higher energy, such that emission in the blue band has comparable intensities to those of the red one. This phenomenon is not observed in PL due to its lower energetic source (UV radiation). $S\text{-}LEC_T$ reached a higher EL intensity than $S\text{-}LEC_P$. Additionally, $S\text{-}LEC_T$ requires less electrical power than $S\text{-}LEC_P$ to achieve its maximum intensity.

Figure 4 displays the J vs. E curve for both textured and non-textured LECs. The J-E curve exhibits the behavior of S-LECs for positive voltage, condition in which EL is observed. Under

ID	Texturing	Roughness [nm]	Peak density [cm^{-2}]	SRO_{30} thickness [nm]
$S\text{-}LEC_P$	No	0.5	0	65.9 ± 0.4
$S\text{-}LEC_T$	Yes	4.0 ± 0.2	$3.7 \pm 1.8 \times 10^{10}$	68.8 ± 1.7

Table 1. Roughening features and SRO_{30} thickness of $S\text{-}LEC_P$ and $S\text{-}LEC_T$.

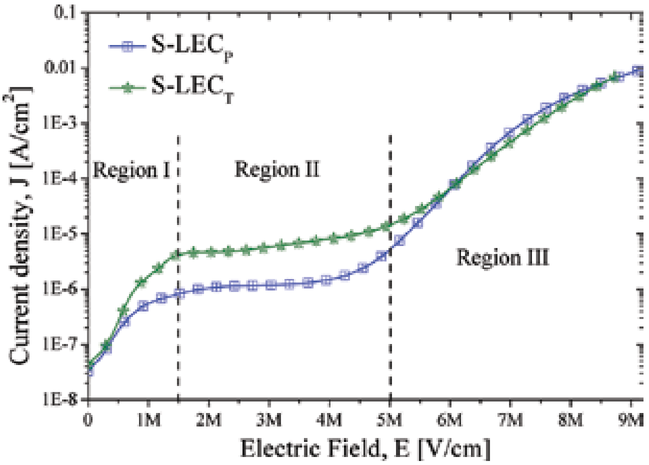

Figure 4. Current density as a function of electric field of S-LECs. Curves are divided in three regions, according to the conduction mechanism for each E range.

this condition, an inversion layer is formed in the SRO/Si-substrate interface. S-LECs presented in this section did not show current jumps, neither the RS from HCS to a LCS, contrary to other reports [14, 15, 19–24]. At low electric fields (region I), the ohmic conduction mechanism dominates the carrier transport; however, roughening of the substrate surface in S-LEC$_T$ propitiates a current increase due to the conical structures in silicon surface, which act as tips highly populated by electrons allowing for higher injection rates through the SRO layer. At medium electric fields (region II), the Fowler-Nordheim tunneling mechanism is responsible for the conduction. In this regimen, the observed current offset between curves of S-LECs is due to the augment of current density at lower electric fields; however, both curves present comparable slope [28]. At the higher electric fields (region III), the trap-assisted tunneling mechanism controls the carrier transport. In this regimen, both S-LEC$_P$ and S-LEC$_T$ present electroluminescence, in agreement with results of the LECs presented in Section 3.1. As can be seen in **Figure 4**, in region III the J-E curves of S-LECs overlap, but even though they have similar electrical responses, S-LEC$_T$ achieves a substantial improvement of electro-optical properties as compared to its counterpart, as it will be shown later.

3.3. SRO multilayers

LECs based on multilayered structures are obtained by a multistep deposition process. While the samples remain in the reactor, the LPCVD system is periodically adjusted to change the R$_0$, modifying the silicon excess in the layer deposited during each period. Two structures were fabricated: M-LEC$_{525}$ and M-LEC$_{1025}$, which alternate four mainly conductive layers (R$_0$ = 5) with three primarily emitting layers (R$_0$ = 25). For both devices, P-type silicon wafers with resistivity between 2 and 4 Ω × cm were used as substrate.

M-LEC$_{525}$ has SRO$_5$ as conductive layer and SRO$_{25}$ as emitting layer, with thickness of 15 and 25 nm, respectively. Meanwhile, M-LEC$_{1025}$ uses the same material for emitting layers but

SRO_{10} instead of SRO_5, with thickness of 10 nm. The nominal thickness of the whole structure is 115 nm approximately. In the top of the multilayer, a semitransparent 250 -nm thick n^+ polycrystalline silicon layer was deposited, and a square gate with an area of 4.05 mm^2 was formed.

Figure 5(a) shows the PL spectra of the SRO multilayers. Two bands are observed: blue and red bands. The shape of PL spectra is quite similar to that of SRO_{30}, which does not have Si-ncs [25], suggesting that, as in SRO_{30}, oxygen defects in the oxide matrix due to the silicon excess are the main cause of PL emission in multilayered structures [34]. As it is reported in [37], Si-ncs are observed in SRO multilayers, and their size and density depend on the features of each layer (silicon excess, thickness, etc.), in agreement with other reports on multilayers [27, 34, 38]. **Table 2** summarizes the Si-nc features of M-LECs. **Figure 5(b)** and **(c)** displays the EL spectra of M-LECs. Again, two luminescent bands are obtained; however, M-LEC_{525} has a more prominent blue band, whereas M-LEC_{1025} achieves higher emission in red band. In [37], this difference is associated with the size and density of Si-ncs embedded in the conductive layers. In M-LEC_{525}, SRO_5 layers allow electrons reach deeper traps (blue emission centers); meanwhile M-LEC_{1025} requires higher electric fields (energy) in order to excite the same emission centers. Thus, conductive layers with bigger size and lower density of Si-ncs produce

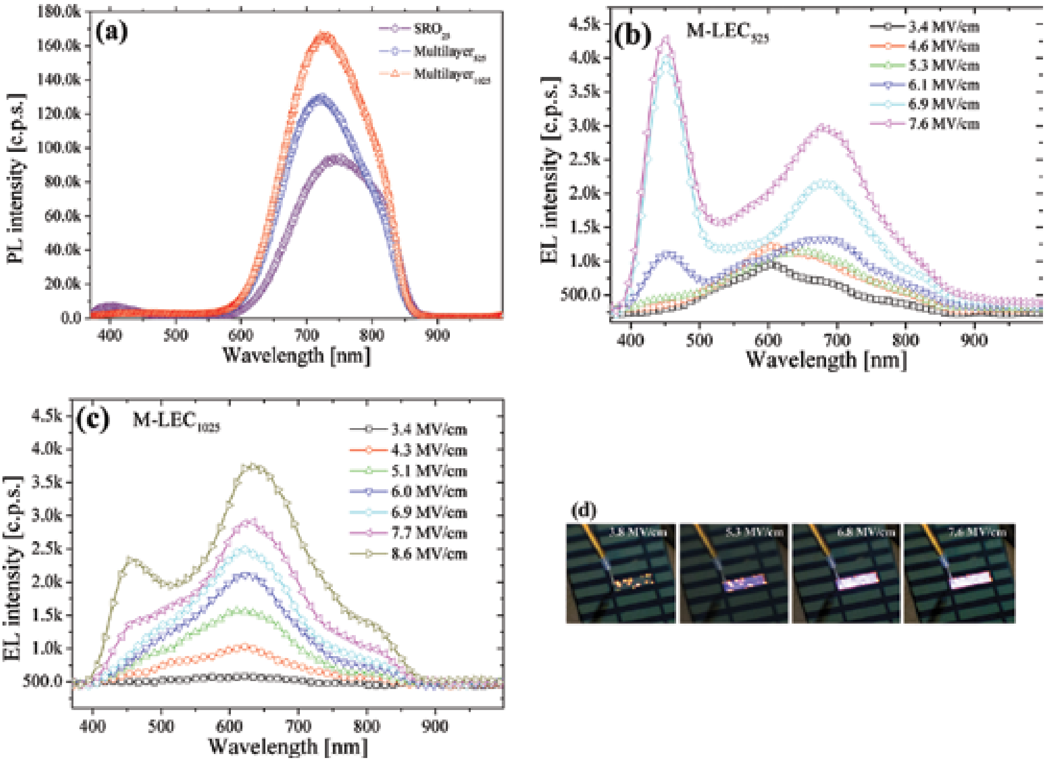

Figure 5. (a) PL spectra of SRO multilayers of M-LECs. SRO mono- and multilayers were excited with λ = 300 nm. EL spectra of (b) M-LEC_{525} and (c) M-LEC_{1025}. (d) EL emission of M-LEC_{525} for different electric fields. Note that whole area emission and localized bright spots can coexist.

ID	Si-nc size of CL* [nm]	Si-nc density in CL [cm^3]	Si-nc size of EmL** [nm]	Si-nc density in EmL [cm^3]	Nominal thickness [nm]
M-LEC$_{525}$	4.0	1.06×10^{12}	2.1	5.76×10^{11}	131.1 ± 7.6
M-LEC$_{1025}$	3.6	1.30×10^{12}	1.8	7.43×10^{11}	116.7 ± 1.6

*CL—conductive layer.

**EmL—emitting layer.

Table 2. Size and density of Si-nc in each layer, as well as nominal thickness of multilayered structure.

M-LECs with brightest blue emission at lower electric fields. **Figure 5(d)** shows digital pictures of the EL emission of M-LEC$_{525}$ biased with different electric fields, where blue color is predominant in the emission.

Figure 6 exhibits J-E characteristics of the M-LECs. In a first test, M-LECs present a LCS, but once they reach a high electric field (E > 5 MV/cm), M-LECs change to a HCS and remain in this regimen for the subsequent measurements, as previously reported in [39] and agreeing with others works [34, 40]. During first current-voltage measurement, Si-ncs are ordered forming conductive trajectories (electroforming) whereby electrons can be easily driven through the SRO multilayers [22, 23]. Across their conductive path, they can impact other electrons not only increasing the current density but also augmenting the number of electrons able to decay at different trap levels, enhancing the emission intensity as well. In [39], it is reported that thermionic emission, Poole-Frenkel, trap-assisted tunneling, and impact ionization conduction mechanisms are responsible for the charge transport. The first two dominate conduction in low (E < 2 MV/cm) and medium (2 MV/cm < E < 4 MV/cm) electric field regimes, respectively. Meanwhile, TAT and impact ionization are responsible for charge transport in

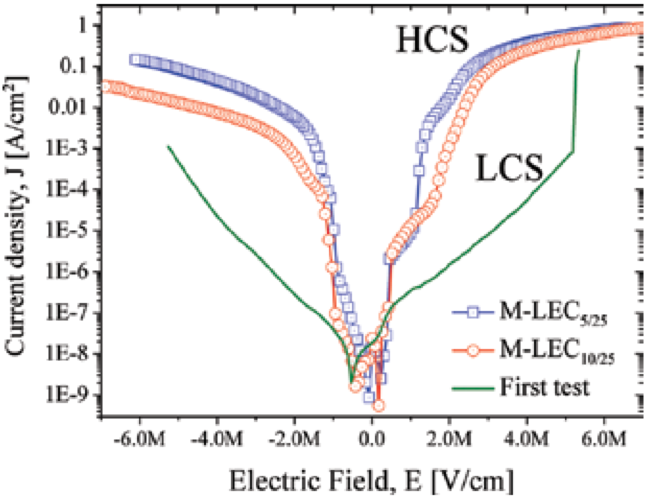

Figure 6. Current density as a function of electric field for M-LECs. In a first sweep, M-LECs present a LCS, but once they achieve a HCS, LECs preserve this behavior maintaining EL emission.

high-energy regime, which is also the region where brightest EL is observed. For E < 6 MV/cm, only TAT mechanism is presented, but once electric field overpass 6 MV/cm, impact ionization takes place, increasing substantially the EL intensity.

4. Discussion

Figure 7(a) and **(b)** shows, respectively, the normalized PL spectra and the J-E curve for S-LEC$_P$, S-LEC$_T$, M-LEC$_{525}$, and M-LEC$_{1025}$ in order to compare single- and multilayer-based LECs. Regarding PL response, multilayer of M-LEC$_{1025}$ records the highest intensity, followed by M-LEC$_{525}$ and single SRO$_{25}$ and SRO$_{30}$ layers. The total PL emission in a multilayered structure has two contributions: emission of SRO$_{25}$ layers, which is the main contribution, and emission from the conductive SRO layers (SRO$_5$ or SRO$_{10}$), which have a smaller contribution [37]. As reported in [26], SRO films with higher density of Si-ncs with size lower than 3 nm have the brighter emission. In these films, defects are formed at the interface between SRO and the Si-ncs, acting as localized states from where electrons decay through ground states, emitting light in the process. Even though conductive SRO layers mainly enhance electrical characteristics in M-LECs, the presence of Si-ncs into SiO$_x$ matrix propitiates a non-negligible contribution to PL emission, and as can be observed in **Table 2**, the highest density with the lowest size of Si-ncs is achieved in M-LEC$_{1025}$, in agreement with PL response.

In **Figure 7(b)**, J-E curves of LECs are presented. A substantial augment of current density in M-LECs with respect to that one in S-LECs can be observed. M-LECs reach the HCS at lower voltages. This improvement of carrier transport in M-LECs is ascribed to the high silicon content in SRO conductive layers. In the electroforming process observed in these M-LECs, which occurs in the first J-E measurement, Si-ncs are connected creating multiple preferential conductive paths between the poly and Si-substrate. Electrons can easily flow through those conductive trajectories in SRO MLs improving the current density. Regarding S-LECs, SRO layer does not have Si-ncs to form conductive paths; however, it has a high density of defects.

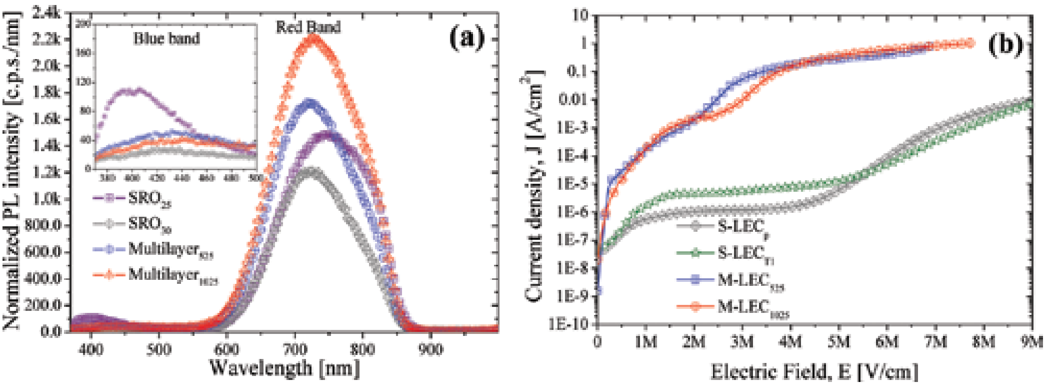

Figure 7. (a) PL spectra normalized with respect to thickness of the SRO single or multilayer. (b) Current density as a function of electric field for S-LECs and M-LECs.

This high content of defects allows that electron transit by a sequence of low energetic traps through the SRO film, named as low resistive trajectories. Even though these trajectories are low resistive, the charge-trapping effect still takes place, such that enhancement of current density is limited and a HCS is not reached. Fabricating S-LECs on textured substrate allow improvement of carrier injection to the SRO film; however, this technique also has results with lower current density improvement than those in a multilayered structure.

Figure 8 displays the integrated EL intensity as a function of electric field for (a) S-LECs on polished substrates and (b) S-LECs on textured substrate and M-LECs. These figures allow comparing LECs by means of two figures of merit: turn-on electric field (E_{on}) and the operation range. The E_{on} is the electric field needed for the EL intensity to overpass the noise level and begin to rise; meanwhile, the operation range is the electric field range in which LECs emit light without electrical damage, and it must go from E_{on} to an E value before dielectric breakdown.

As it can be seen in **Figure 8(a)**, S-LEC$_{20}$ (devices that emit in red) operate on a greater range (from 3.7 to 6 MV/cm) than S-LEC$_{30}$ (devices that emit in blue), which works from 7.0 to 8.3 MV/cm, approximately. The electric field range where it was possible to register EL spectra for S-LEC$_{30}$ is 7.1–8.3 MV/cm and for S-LEC$_{20}$ is 3.7–5.7 MV/cm. As can be noted, a larger electric field is required to obtain the blue emission as compared to the red one. In accordance, the devices without Si-ncs into SRO films and emitting in blue wavelengths require a larger electric field (E > 7MV/cm) to turn on. Additionally, a nearly linear fitting was done to the experimental data. The slope found for each device is slightly different, suggesting that the mechanisms responsible of the EL increase are not the same. A quite similar conclusion was obtained in Section 3.1, where EL emission is observed when TAT and P-F mechanisms dominate the charge transport in S-LEC$_{30}$ and S-LEC$_{20}$, respectively.

In **Figure 8(b)**, it is found that the operation range of S-LEC$_P$ and S-LEC$_T$ is from 8.5 to 11.5 MV/cm and from 7 to 10 MV/cm, respectively. These operation ranges are lower than that one of M-LECs, which have an operation range from 3 to 9 MV/cm, approximately. Thus, M-LECs

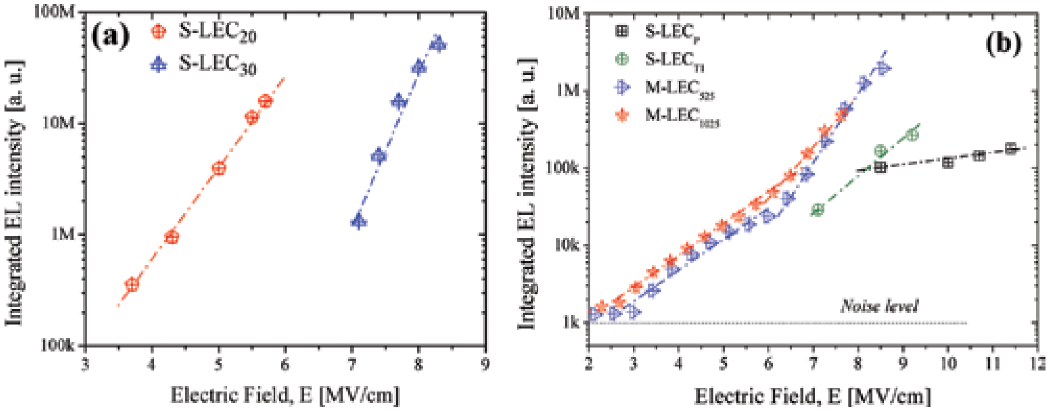

Figure 8. Integrated EL intensity as a function of electric field for (a) single-layer LECS and (b) single-layer LECs on textured substrate and M-LECs. Noise level is used as reference to evaluate EL emission of LECs. Intensities of graph (a) are not comparable with graph (b) because of differences in setup and testing condition.

ID	Voltage [V]	E [MV/cm]	Current [μA]	P_e [mW]	P_{opt} [μW]	η_c [10^{-4} %]
S-LEC$_P$	80	11.4	113	9.04	0.17	18.7
S-LEC$_{T1}$	68	9.7	78	5.30	0.34	64.1
M-LEC$_{525}$	95	7.3	30×10^3	2.85×10^3	2.75	1.0
M-LEC$_{1025}$	95	8.2	37×10^3	3.52×10^3	2.71	0.9

Table 3. Voltage, electric field, electrical power, optical power, and conversion efficiency of LECs: single layer, roughening substrate, and multilayers.

have twice higher operation range than S-LECs. Moreover, the E_{ON} value of M-LECs is lower than that one of S-LECs, and the EL intensity of M-LECs gradually increases as the electric field becomes stronger. In contrast, S-LECs require a higher electric field to emit light, and their transition from turn-off state to turn-on state is abrupt. Hence, M-LECs are better candidates to be integrated in all-silicon photonic circuits due to the lower E_{on} and a wider operation range.

Finally, the conversion efficiency (η_c) is analyzed for each device. The η_c is defined as the ratio of the optical power (P_{opt}) with respect to the electrical power (P_e). The latter power is calculated as $P_e = V*I$, where V is the voltage and I is the electrical current in which a specific P_{opt} is measured. **Table 3** resumes values of voltage, electrical current, P_e, P_{opt}, and conversion efficiency (η_c) of LECs with the different strategies used. These parameters were selected considering the best electro-optical performance. As we can see, the S-LECs are more efficient but have lower values of P_{opt}, while M-LECs are less efficient but achieve a significantly higher P_{opt}. Based only on efficiency and without considering the application, S-LECs would be the best option; however, as is aforementioned, M-LECs have other advantages over S-LECs. A higher operation range, lower E_{on} values, an EL intensity that gradually increases, and a greater P_{opt} are the features that place M-LECs as the best option to be integrated in all-silicon photonic circuit. In [4], it has been demonstrated that S-LECs are enough to guaranty the functionality of all-silicon photonic circuits; however, the LECs operate close to the noise level. Thus, the performance of such system could be improved using M-LECs, which have enhanced electro-optical characteristics.

5. Conclusion(s)

This work was focused on the different strategies used to improve the performance of SRO-based LECs fully compatible with the CMOS technology to be integrated in an all-silicon photonic circuit. We reviewed the fabrication and characterization of LECs that use different substrate treatments and a variety of SRO compositions and configurations. LECs were fabricated with single SRO layers (S-LECs) deposited on polished and textured Si substrates. LECs with SRO in a multilayered structure (M-LECs) involving a conductive SRO layer with an emitting one were also fabricated.

It was found that M-LEC$_{1025}$ emits the highest PL intensity, followed by M-LEC$_{525}$ and finally those with single SRO$_{25}$ and SRO$_{30}$ layers. An improved charge injection observed through an augment of current density was obtained in M-LECs with respect to S-LECs, even though S-LECs use textured silicon substrate to improve carrier injection. M-LECs achieve high conduction state with lower voltages, which is ascribed to the high silicon content in SRO conductive layers, forming conductive trajectories by means of electrons that are easily driven through multilayers.

The electro-optical characterization of different LECs exhibited that M-LECs have twice higher operation range than S-LECs. Moreover, M-LECs emit at lower electric fields and their intensity gradually increases as the electric field becomes stronger. In the opposite, S-LECs require a high electric field to emit light, and their transition from turn-off state to turn-on state is abrupt. Hence, M-LECs perform a better behavior to be integrated in all-silicon photonic circuits based on a lower E_{on} and wider operation range. A higher operation range, lower E_{on}, EL emission that gradually increase, and a greater P_{opt} are the features that place M-LEC as the best option to be integrated in all-silicon photonic circuit.

Acknowledgements

Authors want to thank the financial support from CONACYT. L Palacios-Huerta and A.A. González-Fernández acknowledge CONACYT for the postdoctoral grant. The help of technicians Pablo Alarcon, Victor Aca, and Armando Hernández is also appreciated.

Conflict of interest

Authors declare that there is no conflict of interest.

Author details

Jesús Alarcón-Salazar[1], Liliana Palacios-Huerta[1], Alfredo Abelardo González-Fernández[1], Alfredo Morales-Sánchez[2]* and Mariano Aceves-Mijares[1]*

*Address all correspondence to: alfredo.morales@cimav.edu.mx and maceves@inaoep.mx

1 Electronics Department, National Institute of Astrophysics Optics and Electronics, Tonantzintla, Puebla, Mexico

2 Advanced Materials Research Center (CIMAV), Monterrey-PIIT, Apodaca, Nuevo Leon, Mexico

References

[1] Muñoz P, Micó G, Bru L, Pastor D, Pérez D, Doménech J, Fernández J, Baños R, Gargallo B, Alemany R, Sánchez A, Cirera J, Mas R, Domínguez C. Silicon nitride photonic

integration platforms for visible, near-infrared and mid-infrared applications. Sensors. 2017;**17**(9):2088. DOI: 10.3390/s17092088

[2] Fernández AAG, Mijares MA, Sánchez AM, Leyva KM. Intense whole area electroluminescence from low pressure chemical vapor deposition-silicon-rich oxide based light emitting capacitors. Journal of Applied Physics. 2010;**108**(4):43105. DOI: https://doi.org/10.1063/1.3465335

[3] Alarcón-Salazar J, Zaldívar-Huerta IE, Aceves-Mijares M. An optoelectronic circuit with a light source, an optical waveguide and a sensor all on silicon: Results and analysis of a novel system. Optics & Laser Technology. 2016;**84**:40-47. DOI: https://doi.org/10.1016/j.optlastec.2016.04.013

[4] González-Fernández AA, Juvert J, Aceves-Mijares M, Domínguez C. Monolithic integration of a silicon-based photonic transceiver in a CMOS process. IEEE Photonics Journal. 2016;**8**(1):1-13. DOI: 10.1109/JPHOT.2015.2505144

[5] Dong DRYD, Irene EA. Preparation and some preparation and some properties of chemically vapor-deposited Si-rich SiO and SigN, films D. Journal of the Electrochemical Society (JES) and the ECS Journal of Solid State Science and Technology. 1977;**5**:819-823. DOI: doi: 10.1149/1.2131555

[6] Alarcón-Salazar J, López-Estopier R, Quiroga-González E, Morales-Sánchez A, Pedraza-Chávez J, Zaldívar-Huerta IE, Aceves-Mijares M. Silicon-Rich oxide obtained by low-pressure chemical vapor deposition to develop silicon light sources. In: Sudheer Neralla, editor. Chemical Vapor Deposition - Recent Advances and Applications in Optical, Solar Cells and Solid State Devices. InTech; 2016. DOI: 10.5772/63012. http://dx.doi.org/10.5772/63012

[7] Ogudo KA, Schmieder D, Foty D, Snyman LW. Optical propagation and refraction in silicon complementary metal-oxide-semiconductor structures at 750 nm: Toward on-chip optical links and microphotonic systems. Journal of Micro/Nanolithography, MEMS, and MOEMSournal of Micro/Nanolithography, MEMS, and MOEMS. 2013;**12**(1):13015. DOI: 10.1117/1.JMM.12.1.013015

[8] Xu K, Ning N, Ogudo KA, Polleux J-L, Yu Q, Snyman LW, Light emission in silicon: From device physics to applications. In: Proceedings of the SPIE 9667, International Workshop on Thin Films for Electronics, Electro-Optics, Energy, and Sensors. 2015:966702-1-966702-10. https://doi.org/10.1117/12.2199841

[9] Misiakos K, Petrou PS, Kakabakos SE, Yannoukakos D, Contopanagos H, Knoll T, Nounesis G. Fully integrated monolithic optoelectronic transducer for real-time protein and DNA detection: The NEMOSLAB approach. Biosensors and Bioelectronics. 2010;**26**(4):1528-1535. DOI: https://doi.org/10.1016/j.bios.2010.07.104

[10] Camacho-Aguilera RE, Cai Y, Patel N, Bessette JT, Romagnoli M, Kimerling LC, Michel J. An electrically pumped germanium laser. Optics Express. 2012;**20**(10):11316. DOI: https://doi.org/10.1364/OE.20.011316

[11] Sun C, Wade MT, Lee Y, Orcutt JS, Alloatti L, Georgas MS, Waterman AS, Shainline JM, Avizienis RR, Lin S, Moss BR, Kumar R, Pavanello F, Atabaki AH, Cook HM, Ou AJ, Leu JC,

Chen Y-H, Asanović K, Ram RJ, Popović MA, and Stojanović VM. Single-chip microprocessor that communicates directly using light. Nature. 2015;**528**(7583):534-538. DOI: https://doi.org/10.1038/nature16454

[12] Gonzalez-Fernandez AA, Liles AA, Persheyev S, Debnath K, O'Faolain L. Wavelength-controlled external-cavity laser with a silicon photonic crystal resonant reflector. In: Schröder H, Chen RT, editors. Proc. SPIE 9753, Optical Interconnects XVI, San Francisco, California. 2016. pp. 975317. DOI: https://doi.org/10.1117/12.2213288

[13] Jambois O, Berencen Y, Hijazi K, Wojdak M, Kenyon AJ, Gourbilleau F, Rizk R, Garrido B. Current transport and electroluminescence mechanisms in thin SiO2 films containing Si nanocluster-sensitized erbium ions. Journal of Applied Physics. 2009;**106**(6):063526-063532. DOI: https://doi.org/10.1063/1.3213386

[14] Palacios Huerta L, Cabañas Tay SA, Luna López J-A, Aceves M, Coyopol A, Morales-Sánchez A. Effect of the structure on luminescent characteristics of SRO-based light emitting capacitors. Nanotechnology. 2015;**26**(39):395202. DOI: https://doi.org/10.1088/0957-4484/26/39/395202

[15] Morales-Sánchez A, Monfil-Leyva K, González AA, Aceves-Mijares M, Carrillo J, Luna-López JA, Domínguez C, Barreto J, Flores-Gracia FJ. Strong blue and red luminescence in silicon nanoparticles based light emitting capacitors. Applied Physics Letters. 2011; **99**:171102. DOI: https://doi.org/10.1063/1.3655997

[16] Lai BH, Cheng CH, Lin GR. Electroluminescent wavelength shift of Si-rich SiOx based blue and green MOSLEDs induced by O/Si composition Si-QD size variations. Optical Materials Express. 2013;**3**(2):166. DOI: https://doi.org/10.1364/OME.3.000166

[17] Wang DC, Chen JR, Zhu J, Lu C-T, Lu M. On the spectral difference between electroluminescence and photoluminescence of Si nanocrystals: A mechanism study of electroluminescence. Journal of Nanoparticle Research. 2013;**15**(11):2063. DOI: https://doi.org/10.1007/s11051-013-2063-x

[18] Chen D, Xie ZQ, Wu Q, Zhao YY, Lu M. Electroluminescence of Si nanocrystals-doped SiO_2. Chinese Physics Letters. 2007;**24**(8):2390. DOI: https://doi.org/10.1088/0256-307X/24/8/064

[19] Morales-Sánchez A, Barreto J, Domínguez C, Aceves M, Luna-López JA. The mechanism of electrical annihilation of conductive paths and charge trapping in silico- rich oxides. Nanotechnology. 2009;**20**(4):045201. DOI: https://doi.org/10.1088/0957-4484/20/4/045201

[20] Morales-Sánchez A, Barreto J, Domínguez C, Aceves-Mijares M, Luna-López JA, Perálvarez M, Garrido B. DC and AC electroluminescence in silicon nanoparticles embedded in silicon-rich oxide films. Nanotechnology. 2010;**21**(8):085710. DOI: https://doi.org/10.1088/0957-4484/21/8/085710

[21] Yao J, Sun Z, Zhong L, Natelson D, Tour JM. Resistive switches and memories from silicon oxide. Nano Letters. 2010;**10**(10):4105. DOI: 10.1021/nl102255r

[22] Yao J, Zhong L, Natelson D, Tour JM. In situ imaging of the conducting filament in a silicon oxide resistive switch. Scientific Reports. 2012;**2**(242):1-5. DOI: 10.1038/srep00242

[23] Mehonic A, Vrajitoarea A, Cueff S, Hudziak S, Howe H, Labbé C, Rizk R, Pepper M, Kenyon AJ. Quantum conductance in silicon oxide resistive memory devices. Scientific Reports. 2013;**3**:2708. DOI: 10.1038/srep02708

[24] Mehonic A, Cueff S, Wojdak M, Hudziak S, Labbé C, Rizk R, Kenyon A. Electrically tailored resistance switching in silicon oxide. Nanotechnology. 2012;**23**(45):455201. DOI: https://doi.org/10.1088/0957-4484/23/45/455201

[25] Aceves-Mijares M, González-Fernández AA, López-Estopier R, Luna-López A, Berman-Mendoza D, Morales A, Falcony C, Domínguez C, Murphy-Arteaga R. On the origin of light emission in silicon rich oxide obtained by low-pressure chemical vapor deposition. Journal of Nanomaterials. 2012;**2012**:890701. DOI: http://dx.doi.org/10.1155/2012/890701

[26] Morales-Sánchez A, Barreto J, Domínguez-Horna C, AcevesMijares M, Luna López JA. Optical characterization of silicon rich oxide films. Sensors and Actuators A. 2008;**142**:12-18. DOI: https://doi.org/10.1016/j.sna.2007.03.008

[27] Palacios Huerta L, Cabañas-Tay SA, Cardona Castro MA, Aceves Mijares M, Domínguez Horna C, Morales Sánchez A. Structural and optical properties of silicon rich oxide films in graded-stoichiometric multilayers for optoelectronic devices. Applied Physics Letters. 2016;**109**:031906. DOI: https://doi.org/10.1063/1.4959080

[28] Alarcón-Salazar J, Vásquez-Agustín MA, Quiroga-González E, Zaldívar-Huerta IE, Aceves-Mijares M. Comparison of light emitting capacitors with textured and polished silicon substrates towards the understanding of the emission mechanisms. Submitted to Journal of Luminescence. 2018 (under review)

[29] Alarcón-Salazar J. Analysis, design, fabrication and characterization of the essential devices to integrate an all-silicon photonic circuit [PhD thesis]. INAOE, Puebla, México. April 2017. DOI: http://inaoe.repositorioinstitucional.mx/jspui/handle/1009/343

[30] Spallino L, Vaccaro L, Sciortino L, Agnello S, Buscarino G, Cannas M, Mario Gelardi F. Visible-ultraviolet vibronic emission of silica nanoparticles. Physical Chemistry Chemical Physics. 2014;**16**:22028-22034. DOI: 10.1039/c4cp02995j

[31] Sopinsky M, Khomchenko V. Electroluminescence in SiO_x films and SiO_x-film-based system. Current Opinion in Solid State & Materials Science. 2003;**7**:97-109. DOI: https://doi.org/10.1016/S1359-0286(03)00048-2

[32] López-Estopier R, Aceves-Mijares M, Falcony C. Cathodo- and photo-luminescence of silicon rich oxide films obtained by LPCVD. In: Yamamoto N, editor. Cathodoluminescence. InTech; 2012. pp. 253-272. DOI: 10.5772/34888

[33] Kalnitsky A, Ellul JP, Poindexter EH, Caplan PJ, Lux RA, Boothroyd AR. Rechargeable E′ centers in silicon implanted SiO_2 films. Journal of Applied Physics. 1990;**67**(12):7359-7367. DOI: https://doi.org/10.1063/1.346059

[34] Wang M, Anopchenko A, Marconi A, Moser E, Prezioso S, Pavesi L, Pucker G, Bellutti P, Vanzetti L. Light emitting devices based on nanocrystalline-silicon multilayer structure. Physica E. 2009;**41**:912-915. DOI: https://doi.org/10.1016/j.physe.2008.08.009

[35] Quiroga-González E, Bensch W, Aceves-Mijares M, Yu Z, López-Estopier R, Monfil-Leyva K. On the photoluminescence of multilayer arrays of silicon rich oxide with high silicon content prepared by low pressure chemical vapor deposition. Thin Solid Films. 2014;**519**:8030-8036. DOI: https://doi.org/10.1016/j.tsf.2011.06.020

[36] Vinciguerra V, Franzo G, Priolo F, Iacona F, Spinella C. Quantum confinement and recombination dynamics in silicon nanocrystals embedded in Si/SiO_2 superlattices. Journal of Applied Physics. 2000;**87**:8165. DOI: https://doi.org/10.1063/1.373513

[37] Alarcón-Salazar J, Zaldívar-Huerta IE, Morales-Sánchez A, Domínguez C, Pedraza-Chávez J, Aceves-Mijares M. Enhancing emission and conduction of light emitting capacitors by multilayered structures of silicon rich oxide. Sensors and Actuators A. 2017;**265**:306-312 http://dx.doi.org/10.1016/j.sna.2017.08.047

[38] Limpens R, Lesage A, Fujii M, Gregorkiewicz T. Size confinement of Si nanocrystals in multinanolayer structures. Scientific Reports. 2015;**5**(17289). DOI: 10.1038/srep17289

[39] Alarcón-Salazar J, Zaldívar-Huerta IE, Aceves-Mijares M, Electrical and electroluminescent characterization of nanometric multilayers of SiO_X/SiO_Y obtained by LPCVD including non-normal emission. Journal of Applied Physics. 2016;**119**(21):215101. DOI: https://doi.org/10.1063/1.4952730

[40] Fu S-W, Chen H-J, Wu H-T, Shih C-F. Effect of SiO_2 layers on electroluminescence from Si nanocrystal/SiO_2 superlattices prepared using argon ion beam assisted sputtering. Vacuum. 2016;**126**:59-62. DOI: https://doi.org/10.1016/j.vacuum.2016.01.020

Multifunctional Optoelectronic Device Based on Resistive Switching Effects

Hongwei Tan, Gang Liu and Run-Wei Li

Additional information is available at the end of the chapter

http://dx.doi.org/10.5772/intechopen.74826

Abstract

Optoelectronic resistive switching devices, utilizing optical and electrical hybrid methods to control the resistance states, offer several advantages of both photons and electrons for high-performance information detecting, demodulating, processing, and memorizing. In the past decades, optoelectronic resistive switching devices have been widely discussed and studied due to the potential for parallel information transmission and processing. In this chapter, recent progresses on the optoelectronic resistive switching mechanism, materials, and devices will be introduced. Then, their performance such as photoresponsivity, on/off ratio, as well as retention will be investigated. Furthermore, possible applications of the optoelectronic resistive switching considering logic, memory, neuromorphic, and image-processing devices will be summarized. In the end, the challenges and possible solutions of optoelectronic resistive switching devices for the next-generation information technology will be discussed and prospected.

Keywords: optoelectronic, resistive switching, memristor, memory, logic, neuromorphic

1. Introduction

The great success of transistor-based integrated circuits for modern computing provided exponential development of the way we live, work, and communicate. In the past decades, device scaling-down was an effective approach to maintain the continuous development of computing capabilities. However, the current semiconductor technology is facing the physical scale limitation and bandwidth bottleneck between memory and central processing unit (CPU) in modern-computing architectures, as shown in **Figure 1a**. Therefore, new devices, new architectures, and even new computing principles are eagerly desired to further enhance computing efficiency and capability in the post-Moore era.

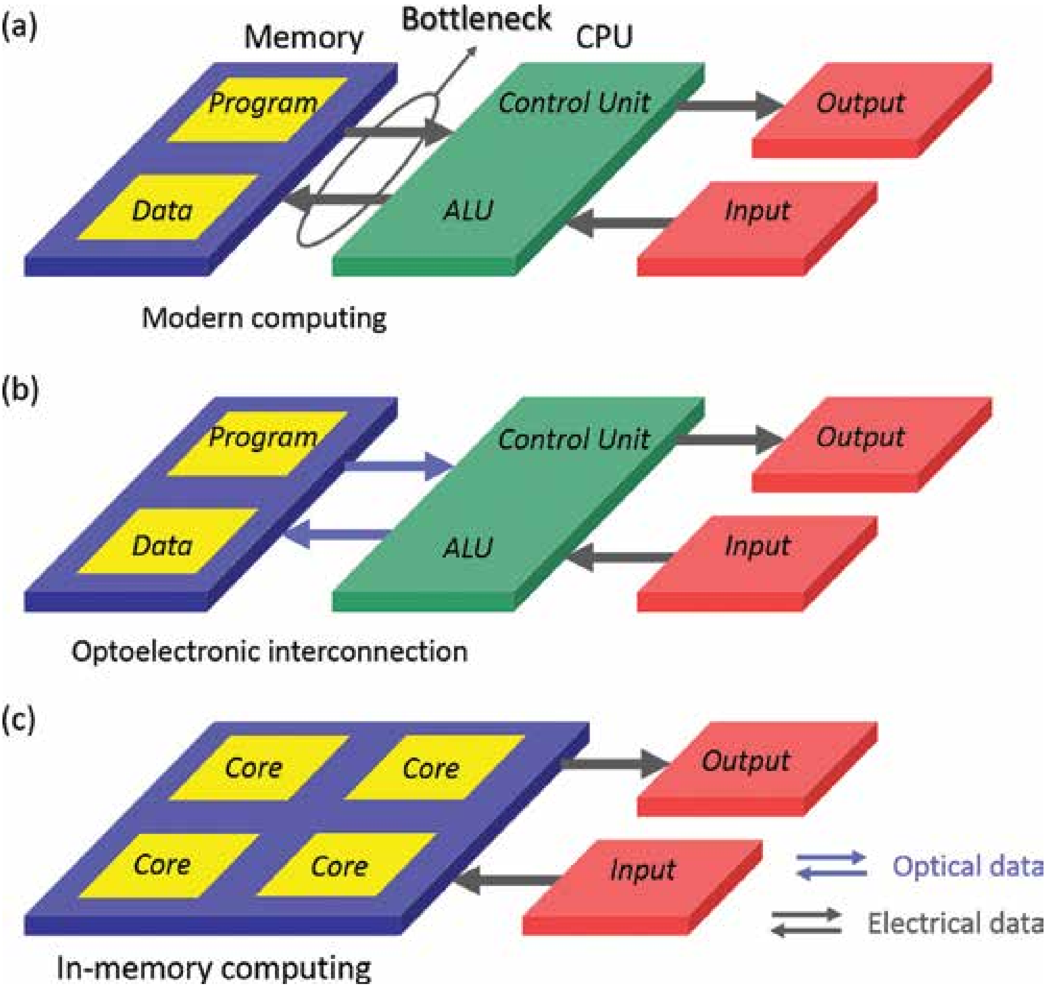

Figure 1. Possible approaches to optimize computing architectures. (a) Modern von Neumann-computing architecture. The separated memory and CPU are connected by data bus, which has frequency limitation. This architecture has low efficiency in data processing between memory and CPU. (b) Optical communication between memory and CPU will overcome the frequency limitation and increase its efficiency. (c) Parallel data processing and memory using memristor-based architecture.

Optoelectronic interconnection is a feasible method to overcome the bottleneck by transmitting data between memory and CPU *via* photons, which have a much faster transporting speed, a higher bandwidth, no Joule heat, and no interference over electrons [1–10]. As shown in **Figure 1b**, optical communication between CPU and memory will fully meet the demands of modern-computing architecture in high-frequency data communicating and processing [1–10]. On the other hand, memristor (memory + resistor), a simple two-terminal electrical switch with nonvolatile reconfigurable resistance states, has been considered as one of the promising approaches to construct new architecture with the novel in-memory computing (**Figure 1c**) [11–20]. Due to the arbitrary nonvolatile resistance states, memristor-based architectures provide the high potential for integrating processor and memory together, which eliminates the bottleneck between memory and processor in the modern von Neumann-computing architecture, thus allowing high parallel data processing [21–26]. However, the electronic memristor-based architecture still has bandwidth limitation in high-frequency data communicating between different modulators.

The combination of photons and memristor-based circuits will integrate the advantages of photons in a high-speed data transmission and memristors in parallel in-memory computing and may open up a new era for future computing owing to the high bandwidth and low-power consumption. Moreover, the optoelectronic-based memristive system will extend the application of memristor-based architecture to image or visual information processing. As shown in **Figure 2**, with the increasing demands of mobile computing in human daily life, wearable devices, health-care devices, and human-machine interacting devices including intelligent image sensor, video monitor, invisible touch screen, electronic eyes, wearable heart or blood monitoring and display devices, smart processor, and even brain-implantable devices will be more and more important for an efficient and comfortable way for our better life, body health, daily work, and communication [27–32]. The optoelectronic memristor-based architecture, wherein both photons and electrons are used for parallel data processing and communicating between input-output (I/O) devices and the in-memory processor, may provide such a platform for the mobile computing.

In this chapter, recent developments on optoelectronic memristor materials and devices, and applications including logic, memory, memristor, and neuromorphic devices will be summarized, then their capability in future optoelectronic on-chip interconnection, in-memory computing, brain-inspired computing, and visual information processing will be evaluated.

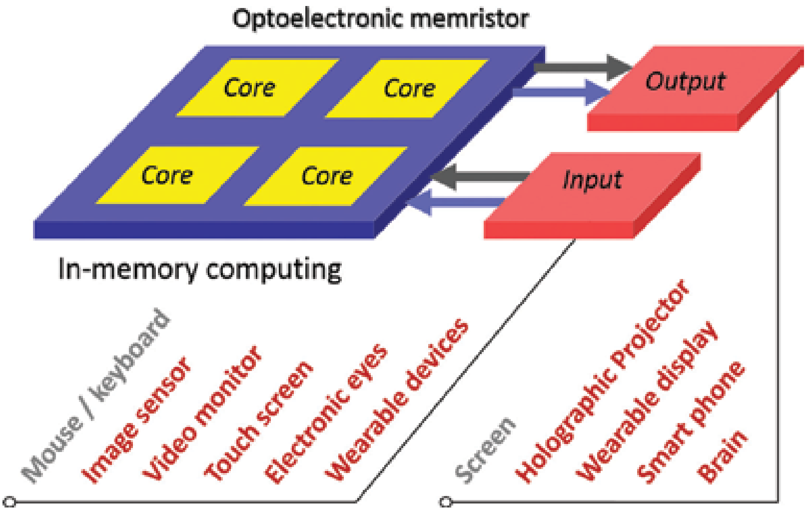

Figure 2. Possible optoelectronic memristor-based-computing architecture. In the in-memory processing unit, a core has the ability to process and store data *in situ*. Both photons and electrons can achieve the communication between the cores and I/O devices.

These optoelectronic approaches may help to overcome the limitations and bottleneck in the current computing devices and architectures, as well as contribute to efficient data analysis, cognitive computation, and artificial intelligence.

2. Optoelectronic resistive switching materials and devices

Resistive switching memory (memristor) is a simple two-terminal device with three-layered structure—two electrode layers for electrical signals input and output, and a "memory" layer in between. The resistance of the "memory" layer can be dynamically reconfigured by voltage- or current-induced ion implantation, interfacial charge accumulation, and so on. Usually, the electrodes are metal or oxide, such as Ag, Au, Pt, Ta, Ir, Cu, ITO, and so on, which will affect the resistive switching behavior by their different work function, electron affinity, electrochemical energy, and so on [33, 34]. For the "memory" layer, various kinds of materials have been used, including binary oxide, nitride, perovskite, low-dimensional materials, and organic materials [35–45]. Due to the simple structure and excellent performance including high-density integration, high-speed, and low-cost fabrication for logic, memory, and neuromorphic applications, memristor has been considered as one of the most promising next-generation information technologies [19, 20, 46].

Meanwhile, optical interconnection with high data transmission speed and no Joule heat or interference has proved to be another effective approach to overcome the data transmission bottleneck between memory and processor. Moreover, combining the advantages of photons and electrons in an optoelectronic memristor will allow highly parallel data transmission and processing, as well as extending the application for image recognition and visual information processing. In the optoelectronic memristor (**Figure 3**), both optical and electrical signals are able to modulate the resistance states of a "memory" layer, which is sensitive to both electrical

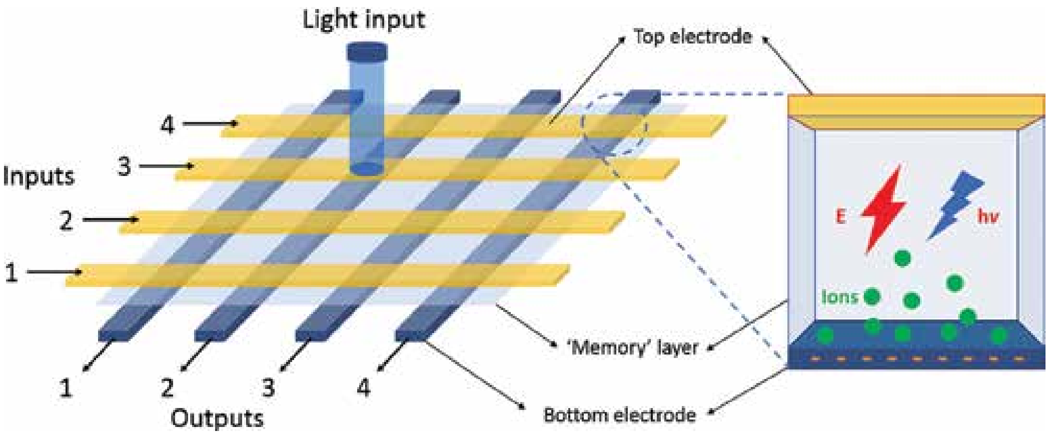

Figure 3. Optoelectronic memristor structure and mechanism.

and optical signals. Therefore, photosensitive semiconductor materials will meet the demands of the "memory" layer, such as silicon, cerium oxide, zinc oxide, perovskite, low-dimensional materials and organic materials, and so on [47–52].

In 2012, Ungureanu et al. reported a reversible light-controlled resistive switching memory in metal/Al_2O_3/SiO_2/Si structure, with the photogenerated electrons injection from Si to Al_2O_3 at sufficient positive bias and charge removal at negative bias [53]. In this work, the light pulses with different wavelength and intensity were utilized to study the photoresponsive behavior of the memory, as well as to achieve multilevel and multifunctional optoelectronic resistive switching memory. This work proved that the metal/Al_2O_3/SiO_2/Si-structured device can work as a multifunctional optoelectronic device including information storage and light sensing, meanwhile, offering the possibility for extra optical degree to be exploited in resistive switching memory devices.

Besides Si, ZnO is another kind of typical photosensitive semiconductor and has been widely studied for UV detectors, as well as resistive switching memories [35, 49]. Based on the semiconducting and photosensing properties of ZnO, Bera et al. combined the resistive switching and persistent photoconductivity (PPC) together in ZnO/NSTO Schottky junction in 2013 [54]. The photo-induced interfacial positive oxygen vacancies movement under electric field can lower the interfacial barrier and modulate the nonvolatile multilevel resistance states, thus realizing persistent photoconductivity and resistive switching. Annealing process was able to erase the PPC to its initial state. The results in this work provided a general route to achieve multifunctional devices by integrating functional materials.

Most recently, two-dimensional materials, such as graphene and MoS_2, have drawn much more attention due to their promising properties for the next-generation information technology. In 2014, Roy et al. reported a multifunctional photoresponsive memory based on graphene-MoS_2 hybrid three-terminal structure, wherein a gate was used to maintain and erase the trapped charges, thus achieving erasable persistent photoconductivity for optoelectronic memory devices (**Figure 4**) [55]. In addition, different gate amplitudes and light intensities were used to achieve multilevel memory. This work showed that the novel two-dimensional materials are promising for multifunctional optoelectronic memory.

Besides, organic materials have many advantages including low-cost fabrication, flexibility, and bandgap tunability, which are promising for optoelectronic memory devices. In 2012, Ye reported an optoelectronic multilevel resistive switching memory shown in **Figure 5** using a metal-conjugated donor-bridge-acceptor (DBA) molecule, which is responsive to both optical and electrical stimuli [56]. Under dark condition, the Al/metal-conjugated DBA/ITO-structured devices showed a bi-stable resistive switching behavior. When illuminated by UV light, a middle state was induced by the sub-step charge transfer process through the cooperation of UV light and electric field. This work may open up new opportunities of organic materials for designing multifunctional optoelectronic memory.

In a short summary, photo-induced charge trapping and detrapping play the key role in optoelectronic resistive switching effect. Other than the materials stated earlier, carbon nanotube, complex oxide, perovskite, quantum dots, and so on, also show optoelectronic resistive

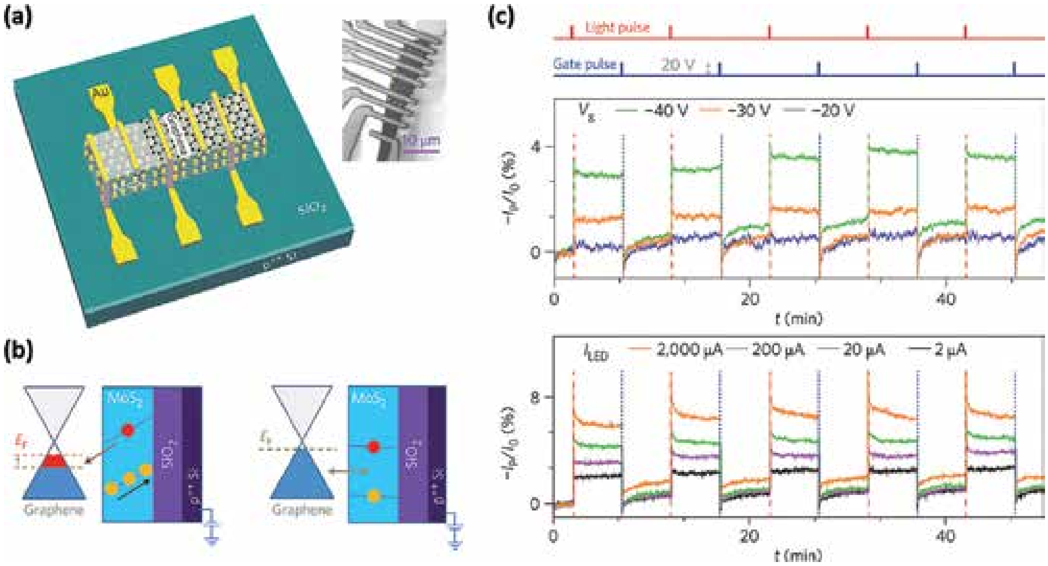

Figure 4. Photosensitive memory based on MoS_2/graphene hybrid structure. (a) Materials and devices structure. (b) Photoresponse mechanism. (c) Multilevel optoelectronic memory via modulating gate bias and light intensity. Reproduced with permission from Ref. [55]. Copyright 2014 Nature Publishing Group.

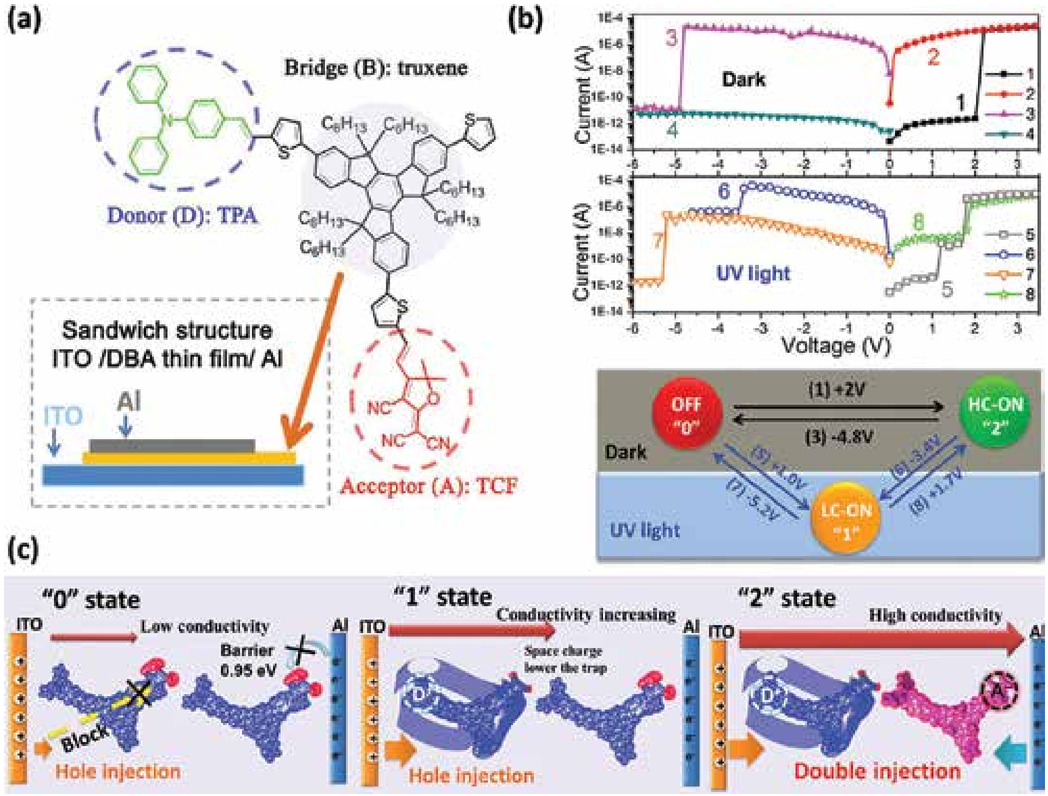

Figure 5. Organic optoelectronic resistive switching memory. (a) Materials and devices structure. (b) Resistive switching behaviors under dark and UV light illuminations. (c) Optoelectronic switching mechanism. Reproduced with permission from Ref. [56]. Copyright 2012 American Chemical Society.

switching effects [57–60]. The applications of optoelectronic memristor including logic, memory, neuromorphic devices, and their performance will be discussed in the following sections.

3. Multifunctional optoelectronic logic and memory

Optoelectronic memristors, allowing electrical and optical signals to modulate the states, are capable of functioning as sensor, decoder, arithmetic unite, logic, and memory devices for data communication, integrated photonics, in-memory computing, and brain-like computing. In this section, optoelectronic logic and memory devices will be discussed and their performance will be evaluated.

Logic is one of basic and most important functions in the integrated circuits [61–65]. Therefore, the realization of optical and electrical-mixed logic is the first step for optoelectronic circuits. For example, Kim et al. reported a series of optoelectronic logic devices based on single-walled carbon nanotube (SWNTs)/silicon junctions [57]. As shown in **Figure 6a**, in the SWNTs/Si junction, voltage and light pulse are inputs and currents are outputs. Due to the photoresponse under voltage bias, the output current is much higher (logical "1") when both voltage and light are applied to the junction than the current when only one or neither is applied (logical "0"), thus functioning as an "AND" gate (**Figure 6b**). Similarly, "OR" gate and 2-bit adder functions were also achieved using two junctions. Furthermore, utilizing four junctions with specialized

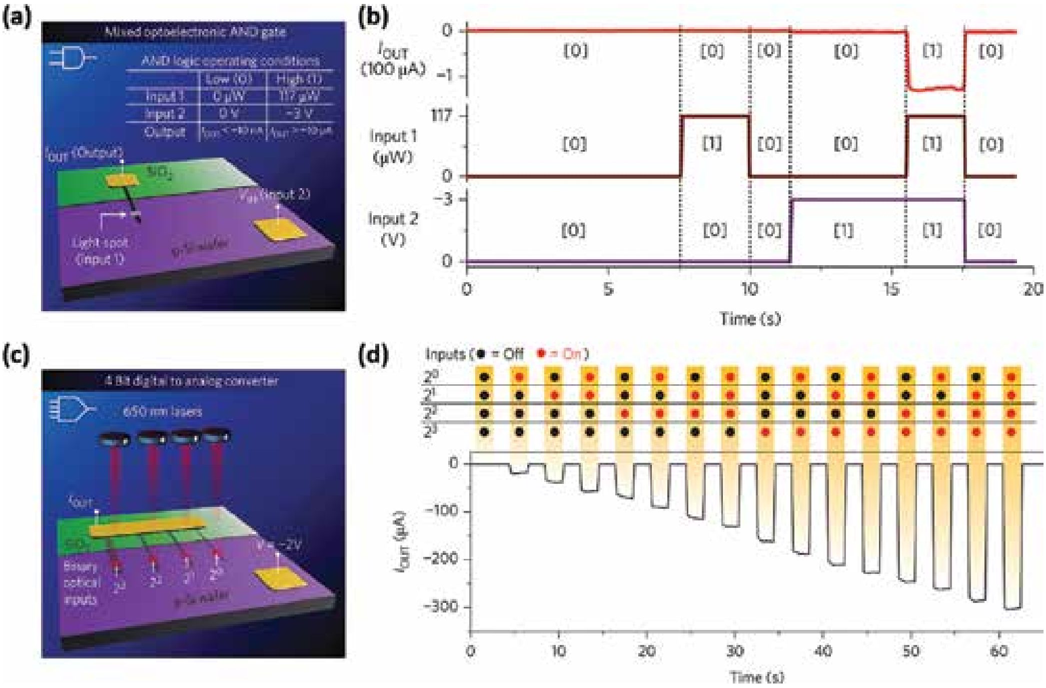

Figure 6. Optoelectronic logic gates. (a) "AND" logic with one light input, one voltage input, and a current output. (b) Output current value of the "AND" gate. (c) 4-bit digital-to-analog converter with light illuminating on four junctions with different areas. (d) Output current value of the 4-bit digital-to-analog converter. Reproduced with permission from Ref. [57]. Copyright 2014 Nature Publishing Group.

active areas, a 4-bit digital-to-analog converter (DAC) was demonstrated, as shown in **Figure 6c** and **d**.

Memory is another basic and important function in integrated circuits. If an optoelectronic memory device can integrate other specific functions such as photo signal detection, demodulation, arithmetic, and even logic in a single device, where the processed data can be stored *in situ*, then it will lower the complexity of integrated circuits and allow highly parallel computation. To achieve this goal, in 2015, we studied the ITO/CeO_{2-x}/AlO_y/Al-structured photoresponsible junction and designed a multifunctional optoelectronic resistive switching memory (OE-memory) with integrated photodetection, demodulation, and arithmetic [66]. As shown in **Figure 7**, CeO_{2-x} works as a photon-absorbing layer, and the electrons trapped in the defects in the CeO_{2-x} layer near the interface can be excited by photons and leaving positively charged oxygen vacancies, which will lower the effective barrier and decrease the resistance of the junction persistently with a thinner barrier. At the CeO_{2-x} and Al interfaces, a 5-nm native oxide layer formed and acted as an insulating layer to decrease the dark current. ITO works as a transparent and conductive top electrode and Al is the bottom electrode. In this simple two-terminal structure, persistent photoconductivity was observed as shown in **Figure 8**. The nonvolatile resistance states can be reversibly switched between high resistance state (HRS) and low resistance state (LRS) by visible light pulse and voltage, thus acting as an optical-write and electrical-erase memory.

Further study of this optoelectronic memory showed the wavelength and intensity-dependent photoresponse, which was utilized to design an optical signal detector and demodulator. As shown in **Figure 9**, with two-digit information (wavelength and intensity) per light pulse, four pulses with blue or green and 4 or 6 pW/μm^2 are capable of carrying

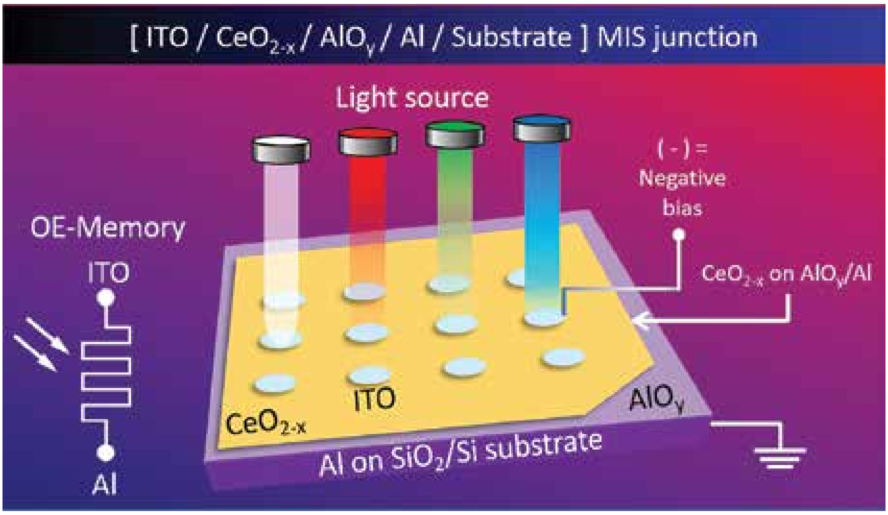

Figure 7. Schematic illustration of the optoelectronic memory (OE-memory) based on the ITO/CeO_{2-x}/AlO_y/Al junction and its operation principle. Reproduced with permission from Ref. [66]. Copyright 2015 WILEY-VCH Verlag GmbH & Co. KGaA, Weinheim.

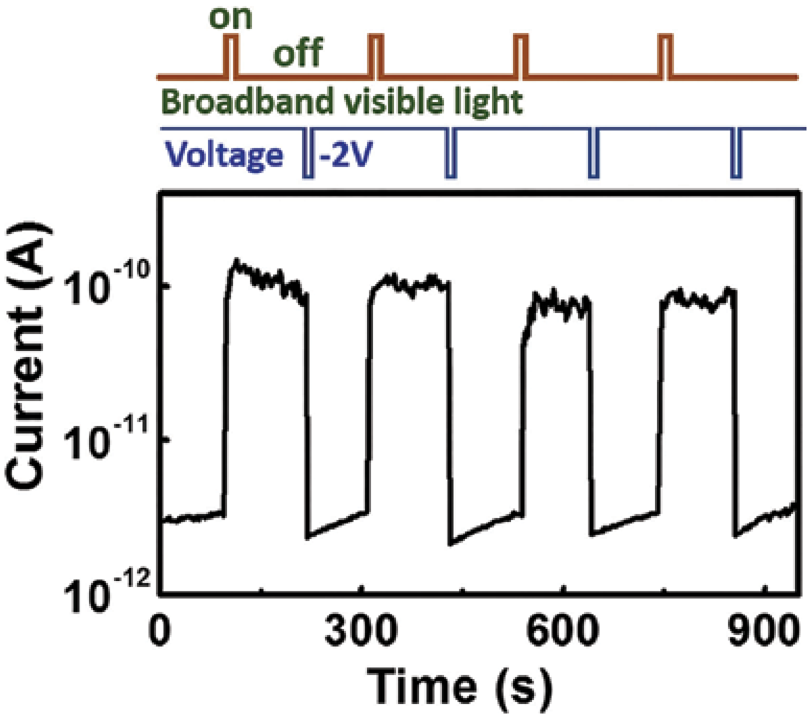

Figure 8. Reversible nonvolatile optoelectronic resistive switching behavior. A visible light pulse switches the structure from HRS to LRS and a voltage pulse switches the structure from LRS to HRS. Reproduced with permission from Ref. [66]. Copyright 2015 WILEY-VCH Verlag GmbH & Co. KGaA, Weinheim.

8-digit information, which is one letter according to the ASCII code, and can be demodulated and stored into four resistance states. Therefore, optical signal detecting and demodulating functions have been achieved in this simple optoelectronic memory. Furthermore, the photoconductance is increasing linearly with light pulse number (**Figure 10a**). Based on this linear relationship between photocurrent and the number of light pulses, counter and adder of the number of light pulses can be realized and the details are shown in **Figure 10b**. Meanwhile, the output results after counting or adding the pulse number can be stored as resistance states, thus allowing the integration of simple arithmetic and memory functions in a single cell. To evaluate the memory retention performance, multilevel resistance states were measured continuously, and after 10^4 s, the resistance states remain distinguishable (**Figure 11**). Above all, the simple optoelectronic structure is capable of functioning as optical signal detection, demodulation, arithmetic, and storage. These results demonstrate the possibility of using multifunctional optoelectronic devices for future integrated photonics, parallel processing, and in-memory computing [66].

In our recent work, to further exploit the integration of logic functions into the memory [67], electrically resistive switching and the persistent photoconductivity are combined to modulate the resistance states (**Figure 12**) [68].

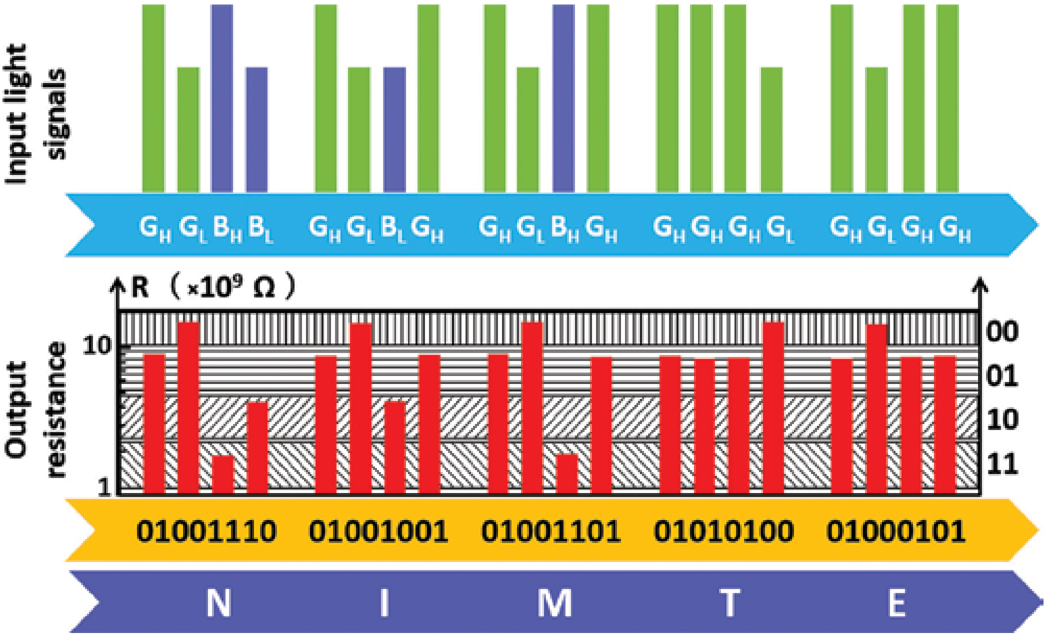

Figure 9. Proof-of-concept demonstration of demodulating function. The work "NIMTE" encoded in light pulses according to ASCII code can be demodulated and stored into nonvolatile resistance states.

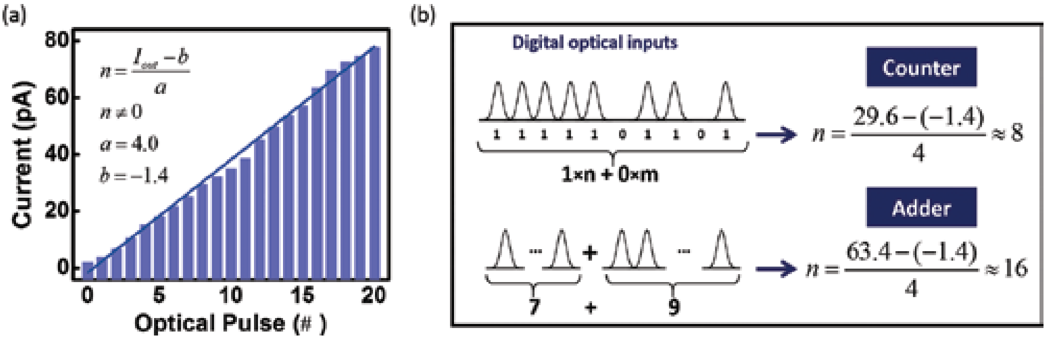

Figure 10. Optoelectronic arithmetic function in the OE-memory. (a) Photocurrent after a series of identical light pulses. (b) Simple counter and adder functions demonstration based on the linear relationship between photocurrent and light pulse number shown in (a). Reproduced with permission from Ref. [66]. Copyright 2015 WILEY-VCH Verlag GmbH & Co. KGaA, Weinheim.

Using one light pulse and one voltage pulse as logical inputs and current as logical output, an "AND" gate was achieved. Only when both a light pulse and a voltage pulse are present, the output value is larger than 150 nA, which is logical "1," otherwise, the output current is lower than 150 nA, which is logical "0." Furthermore, the "AND" gate can be reconfigured to "OR" gate when a light-write pulse applied before logic operations, thus allowing the OE-memory functioning as an optoelectronic nonvolatile reconfigurable logic gate (**Figure 13**). Besides the reconfigurable "AND" and "OR" logic functions, "NOT" operation and a complicated logic operation were achieved by introducing another electrical-erase pulse, as well as optical adder

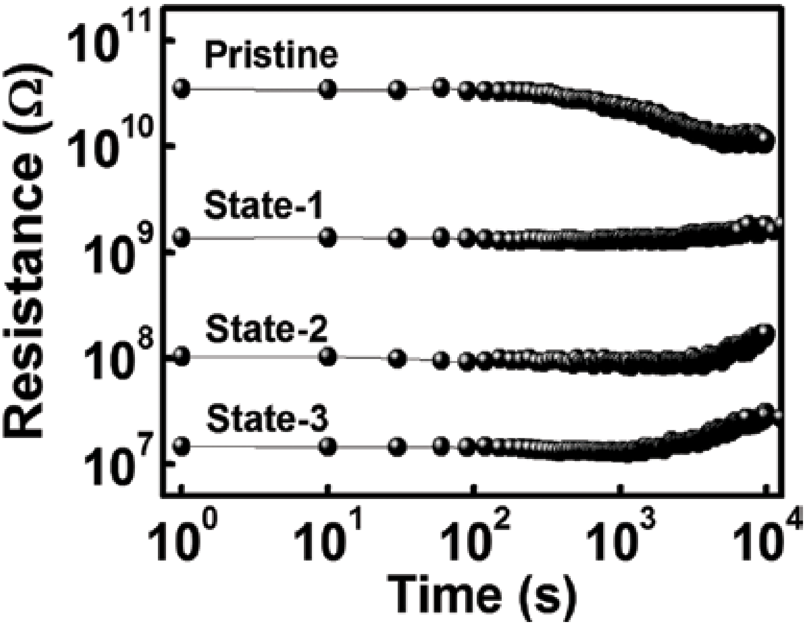

Figure 11. Retention characteristic of four states programmed by light pulses with different intensities. Reproduced with permission from Ref. [66]. Copyright 2015 WILEY-VCH Verlag GmbH & Co. KGaA, Weinheim.

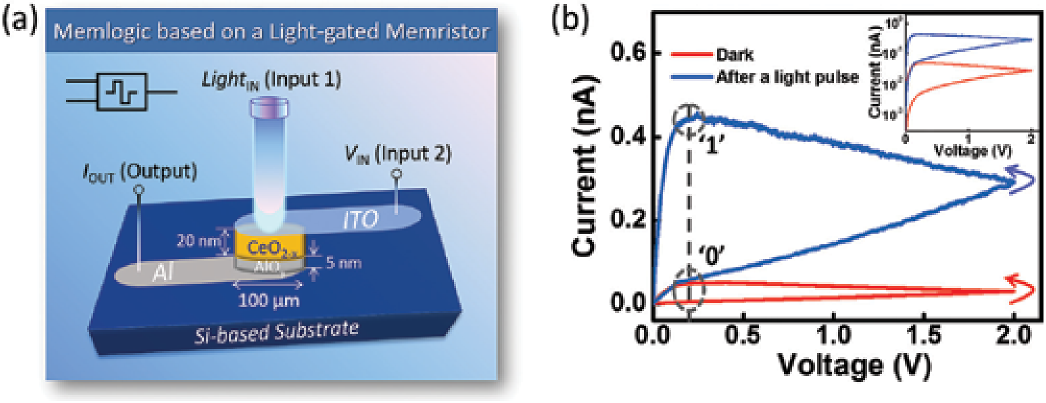

Figure 12. Schematic illustration of the structure (a) and optoelectronic resistive switching behaviors (b) of the memlogic. Reproduced with permission from Ref. [68]. Copyright 2017 American Chemical Society.

and digital-to-analog converter (DAC) functions were achieved by using two light pulses as inputs. We name this nonvolatile reconfigurable logic gate as "memlogic," memory of logic operations and outputs.

Based on the optoelectronic reconfigurable logic functions, a proof-of-concept reconfigurable image-processing and memorizing functions were demonstrated, as shown in **Figure 14**. Two images with "X" and "Y" shapes of visible light pulses are used as inputs into a 5 by 5 memlogic array and current map as output (**Figure 14a**). When all the cells were reset to "AND" logic state,

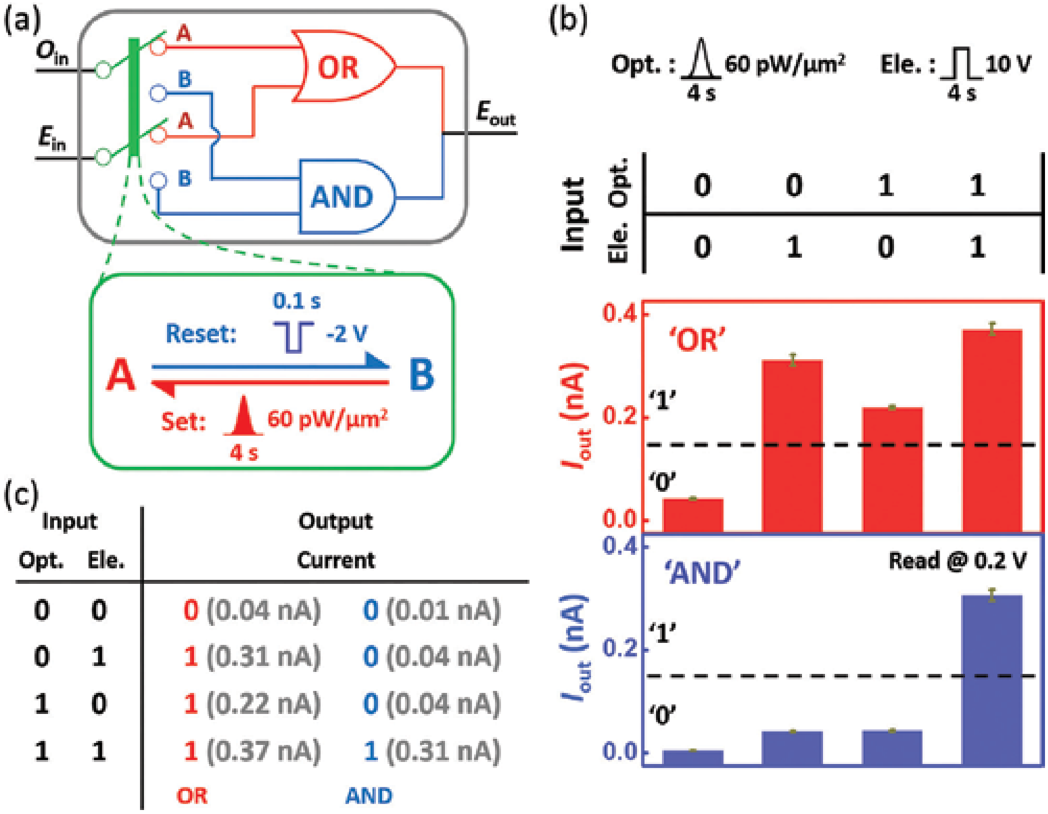

Input		Output	
Opt.	Ele.	Current	
0	0	0 (0.04 nA)	0 (0.01 nA)
0	1	1 (0.31 nA)	0 (0.04 nA)
1	0	1 (0.22 nA)	0 (0.04 nA)
1	1	1 (0.37 nA)	1 (0.31 nA)
		OR	AND

Figure 13. Memlogic operation of reconfigurable "AND" and "OR" gates. (a) Reconfiguration operation of "AND" and "OR" gates. (b) Output current value of the memlogic. (c) Truth table of the memlogic. Reproduced with permission from Ref. [68]. Copyright 2017 American Chemical Society.

the processor can find the same part in different images and we named it SAME FINDER (**Figure 14b**). When all the cells were set to "OR" states, the processor can find the parts either in 'X" or "Y" images and we named it as ALL FINDER (**Figure 14c**). Therefore, the single memlogic array can realize two different image processing, as well as image storage functions.

Above all, the memlogic is capable of performing different reconfigurable logic functions and nonvolatile memory and may provide a new method for reconfigurable in-memory computing, integrated photonics, and artificial intelligence [68].

In summary, for information technology application, these optoelectronic resistive switching devices need to be optimized to improve their performance including the photoresponsivity, speed, memory window, retention time, endurance, fabrication cost, reliability, yield, and so on. Here, the summary of some basic parameters is shown in **Table 1**. The photoresponsivity measures the input–output gain in a photoresponsive system and means the electrical output per optical input. On/off means the memory window. Speed represents how fast the device can work. For memory or logic applications, the speed needs to be at ns level. Here, the speed of these optoelectronic resistive switching devices is not enough and needs to be improved exponentially. Possible methods will be increasing the build-in electric field to accelerate the

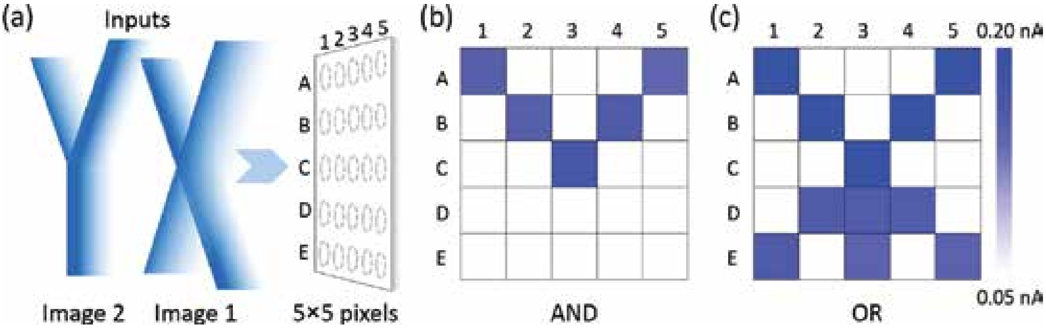

Figure 14. Proof-of-concept demonstration of reconfigurable image processing. (a) 'X' and 'Y″ shape of light image were inputs and current map was the output. (b) Image same finding function when all the memlogic cells are at HRS and (c) image all finding functions when all the memlogic cells are at LRS. Reproduced with permission from Ref. [68]. Copyright 2017 American Chemical Society.

Structure	PPC/PC/PR	Responsivity	On/off	Speed	Retention	References
$Pd/Al_2O_3/SiO_2/Si$	PC	_	10^3	_	_	[53]
Ti/ZnO/NSTO	PPC	_	$>10^3$	~100 s	$>10^4$ s	[54]
Al/Organic/ITO	PR	_	10^6	_	5×10^4 s	[56]
$ITO/CeO_{2-x}/AlO_y/Al$	PPC	1 A/W	10^3	~10 s	$\sim10^4$	[66, 68]

Notes: PPC, persistent photoconductivity; PC, photoconductivity; PR, photoresponse.

Table 1. Characteristics of the typical photoresponsive memristors.

photo-induced charge separation by using electrodes with a higher work function or increasing the defects concentration. Retention means how long the state can maintain. From this table, we can see that the performance especially the speed should be improved immediately.

4. Optoelectronic neuromorphic devices

Artificial neural network is one of the most promising ways to achieve brain-like computing and has been an attractive area especially for memristors as the similar ionics-based mechanisms and stochastic dynamics with neurons [69–87]. Optoelectronic memristors provide another degree of freedom by light to control their states, which means light pulse can be utilized as stimuli to control artificial synapse weight and proceed with synaptic behaviors simulation. Moreover, optoelectronic memristor-based networks allow optical communications among nodes and will reduce power consumption, increase communicating speed, and efficiency. Recently, several research groups have proposed optoelectronic artificial synaptic devices based on persistent photoconductivity for neuromorphic computing. In 2010, Agnus et al. reported an adaptive architecture based on optically gated carbon nanotube transistors, which allow optical write and electrical program processes to control the resistance states [88]. The programmed states are nonvolatile and can be used to store synapse weight in adaptive architectures. More specific synaptic behaviors simulation such as short-term memory (STM), long-term memory (LTM), facilitation, and spike-timing-dependent plasticity (STDP) have been achieved in IGZO-based persistent photoconductive devices by Lee in 2017. They also showed the photoenergy and frequency-dependent plasticity. These basic synaptic behaviors simulation will promote the development of optoelectronic artificial neuro-network [88].

As we all know, human eyes are the most important media to receive visual information from surroundings and provide humans with the ability to recognize objects. In human visual system, the eyes receive light signal and convert it to electrical pulses signal, which can be detected by visual neuron and analyzed or memorized by visual cortex in the brain. In general, two parts for sensing and processing of visual information form the visual system. In recent years, inspired by human visual system, several kinds of artificial visual systems have been proposed to simulate eyes for visual information processing, retinopathy therapy, and reproduction of visual system [27, 89–91]. Usually, photodetector array acts as the retina to sense the light that converts it to electrical signal for image processor, visual neuron, and cortex. For example, as shown in **Figure 15**, Mathieson et al. reported a photovoltaic retinal prosthesis, which is capable of detecting light signal, imaging on silicon photodiode array, and processing the detected image. The demonstration of fully integrated wireless implant may reproduce the vision to the patients with retina diseases [27]. However, this photodiode-based system lacks the function of memorizing of image information. Therefore, memristor may be applicable for image memory. In 2017, Chen et al. reported an artificial visual memory system consisting of an imager and a memory. The UV image can be detected by In_2O_3-based imaging system and stored by Al_2O_3-based

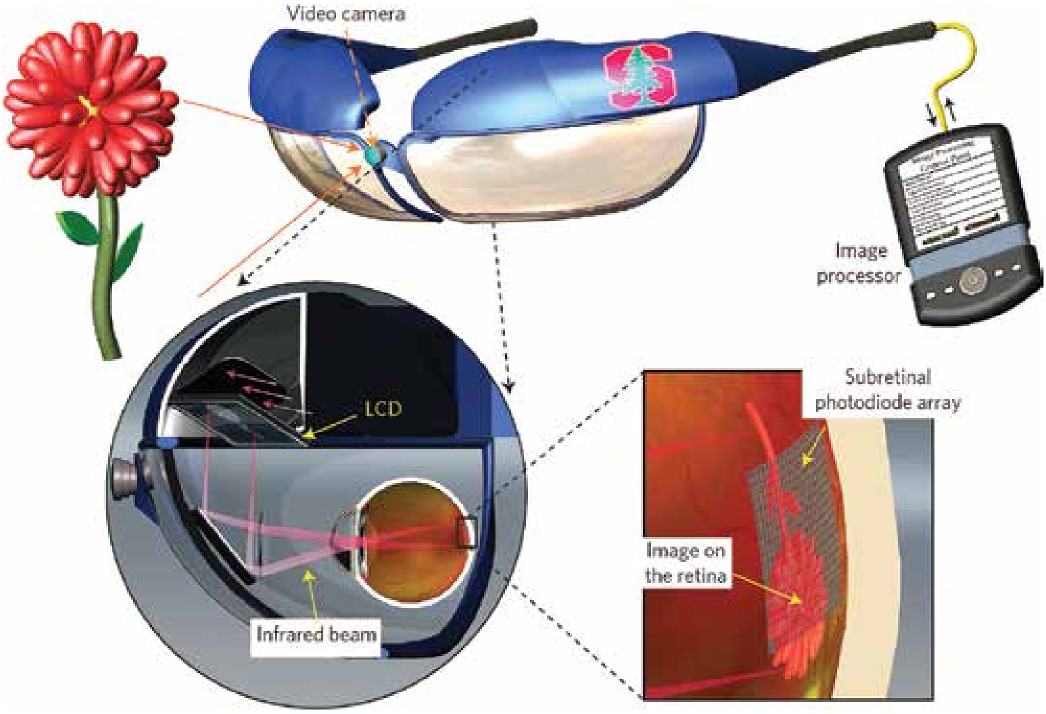

Figure 15. An artificial visual system based on silicon photodiode. Reproduced with permission from Ref. [27]. Copyright 2012 Nature Publishing Group.

processing and memory system [92]. The design of this artificial visual system provides a novel approach to integrate different devices to achieve more multifunctional bioinspired systems.

Thanks to the reported works, these novel promising optoelectronic synaptic devices have been proposed and achieved and will be the first step for optoelectronic neural networks. Optoelectronic artificial neural networks provide the additional advantage of optical communication into memristor-based neuromorphic architectures. Based on the previous research, the next plan should focus on improving their performance, exploiting optoelectronic artificial neural networks, and optogenetic neural networks.

5. Other approaches for multifunctional resistive switching

Besides the optical-based resistive switching memories, electrical- and magnetic-based resistive switching devices are also interesting and attractive due to their important and promising physical properties and applications [93].

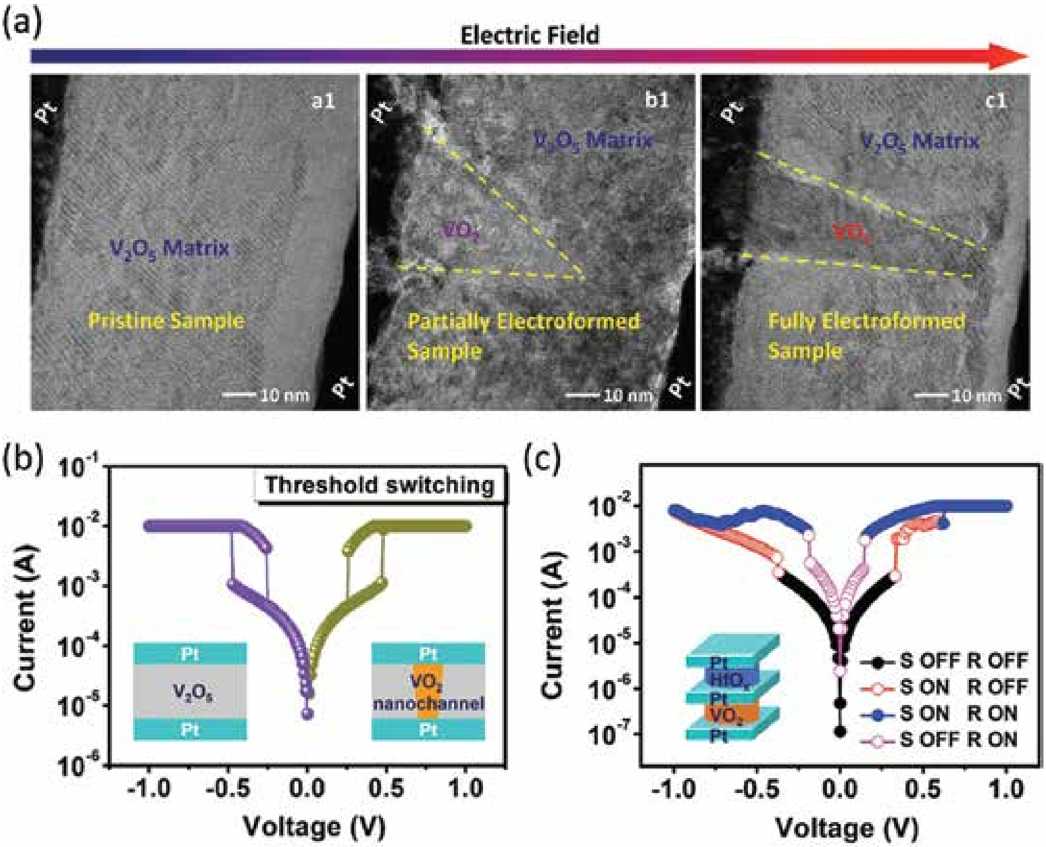

Figure 16. Nanochannel-based selector mechanism and its performance. (a) Transmission electron microscopic (TEM) image proved the electric field-induced VO_2 nanochannel formation in V_2O_5 matrix. (b) Threshold switching behavior. (c) Resistive switching behavior of the 1S1R structure. Reproduced with permission from Ref. [94]. Copyright 2017 WILEY-VCH Verlag GmbH & Co. KGaA, Weinheim.

Recently in our group, a nanochannel device was designed in V_2O_5-based selector via electric field-induced ion migration [94]. As shown in **Figure 16**, this electric field-induced nanochannel demonstrates a sharp and reliable metal–insulator transition (MIT) with a 17 ns switching speed, an 8 pJ energy consumption, and less than 4.3% variability. By combining with one HfO_x-based memristor, the 1S1R structure device can ensure the correct reading of the memory states continuously for 10^7 cycles, therefore demonstrating its great possibility to overcome the crosstalk problem in high-density crossbar memory. This work proved that electric-field-induced ion migration at the nanoscale is an effective approach to optimize device performance or design novel conceptual devices.

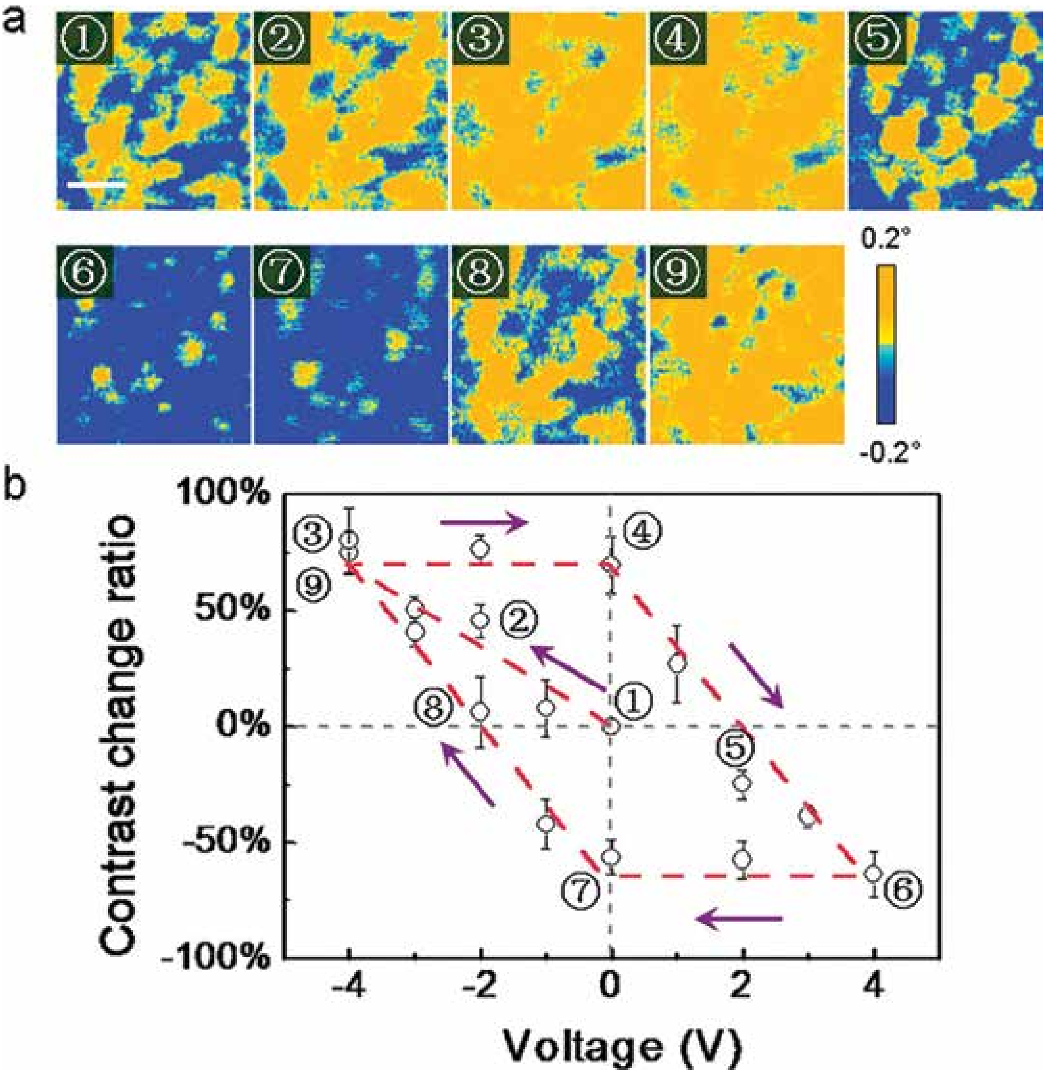

Figure 17. Electric field-controlled magnetization reversal. (a) Magnetic force microscope (MFM) images of the CFO at initial states and after voltage bias. (b) Evolution of the contrast change ratio after being subjected to various biased voltages. Reproduced with permission from Ref. [95]. Copyright 2015 American Chemical Society.

With the electric field-induced ion migration method, our group also achieved nanoscale magnetization reversal in cobalt ferrite (CFO) thin film (**Figure 17**) [95, 96]. The electric field-induced migration and redistribution of Co^{2+} between Fe vacancies induced the unidirectional magnetic anisotropy of the sample along the <110> directions. The reported magnetization reversal is nonvolatile and reversible, which can be controlled by tuning the electric field polarity and amplitude. Such a nanoscale magnetization modulation by nanoionics may provide a novel approach to manipulate the magnetization of magnetic materials for low-power magnetic memory and spintronics.

6. Challenges and possible approaches

Thanks to the efforts of scientific researchers and engineers from all over the world, the optoelectronic resistive switching has achieved great progress. However, there are still some challenges in the way of further development of optoelectronic memristors currently as follows:

1. Mechanism: the widely accepted mechanism of PPC is the photo-induced charge trapping and detrapping in defects. However, due to the technique limitation of directly mapping photo-generated carriers' distribution under light illumination, it is hard to clarify the PPC at electron scale.
2. Materials and performances: many materials are photoresponsive and resistance switchable. Therefore, finding a durable, reliable, and CMOS-compatible material with excellent optoelectronic resistive switching performances is still a challenge, and the performance especially the speed is more challenge due to defects-related process.
3. Spatial design of the optoelectronic neural networks: optoelectronic platform will need to integrate light source to the integrated circuits. Therefore, the devices' surface and physical position should be accessible for light source. Then the best way to route the light source to devices' surface is a critical issue.

Possible approaches include the following:

1. Mechanism: light-integrated TEM is a possible method to observe the light-controlled physical properties. In my current group in Finland, an *in situ* TEM under external electric field and light sources is ready, and there may be some promising results about optoelectronics in the following years [97].
2. Materials and performance: the direct and effective way to find a suitable material is trying and trying. One promising material has to be tested, optimized, and improved repeatedly before the product, and what we can do is to just be patient. The performance requirement depends on the application, so performance is negotiable [17].
3. Spatial design of the optoelectronic neural networks: with the development of nanophotonics and nanolasers, in the near future, integrated photonics will provide efficient and feasible approach to address the spatial design of optoelectronic artificial neural networks [6].

7. Conclusions and prospects

In this chapter, recent progress on optoelectronic resistive switching are introduced and summarized. Due to the photosensitive media in memristor, light can be used as another degree of freedom to control the resistive switching behavior for multifunctional optoelectronic devices. Here, the main mechanism is the photo-induced carriers trapping and de-trapping in defects in the semiconductor "memory" layer. To further promote the development of the multi-functional optoelectronic devices, their performance should be improved to meet different applications considering image sensor, memory, logic, and neuromorphic devices.

Optoelectronic memristor-based neuromorphic devices, integrating the functions of information storage, processing, image detection, and memory together, may provide high potential for intelligent image sensor and optoelectronic in-memory computation. Based on the integrated photonics [1–10], optoelectronics [47–60], and optogenetics [98–100], an optoelectronic artificial neural network may play a key role in future human-machine interactive devices.

Acknowledgements

This work was supported by the National Key R&D Program of China (2017YFB0405604), the National Natural Science Foundation of China (61722407, 61674152, 51525103, 11474295), the Natural Science Foundation of Zhejiang Province (LR17E020001), and the Youth Innovation Promotion Association of the Chinese Academy of Sciences (2014261).

Conflict of interest

The authors declare no conflict of interest.

Author details

Hongwei Tan[1], Gang Liu[2,3]* and Run-Wei Li[2,3]

*Address all correspondence to: liug@nimte.ac.cn

1 Nanospin, Department of Applied Physics, Aalto University School of Science, Aalto, Finland

2 CAS Key Laboratory of Magnetic Materials and Devices, Ningbo Institute of Materials Technology and Engineering, Chinese Academy of Sciences, Ningbo, P.R. China

3 Zhejiang Province Key Laboratory of Magnetic Materials and Application Technology, Ningbo Institute of Materials Technology and Engineering, Chinese Academy of Sciences, Ningbo, P.R. China

References

[1] Assefa S, Xia F, Vlasov YA. Reinventing germanium avalanche photodetector for nanophotonic on-chip optical interconnects. Nature. 2010;**464**:80-84. DOI: 10.1038/nature 08813

[2] Assefa S, Shank S, Green W, Khater M, Kiewra E, Reinholm C, Kamlapurkar S, Rylyakov A, Schow C, Horst F, Pan H, Topuria T, Rice P, Gill D M, Rosenberg J, Barwicz T, Yang M, Proesel J, Hofrichter J, Offrein B, Gu X, Haensch W, Ellis-Monaghan J, Vlasov Y. A 90 nm CMOS integrated nano-photonics technology for 25 Gbps WDM optical communication applications. In: IEEE International Electron Devices Meeting (IEDM); Dec 10–13, 2012; San Francisco. Indianapolis, Indiana, U.S.: IBM Press, IEEE; 2012. pp. 33.8.1-33.8.3

[3] Xu Q, Schmidt B, Pradhan S, Lipson M. Micrometre-scale silicon electro-optic modulator. Nature. 2005;**435**:325-327. DOI: 10.1038/nature03569

[4] Liu M, Yin X, Ulin-Avila E, Geng B, Zentgraf T, Ju L, Wang F, Zhang X. A graphene-based broadband optical modulator. Nature. 2011;**474**:64-67. DOI: 10.1038/nature10067

[5] Hosseini P, Wright CD, Bhaskaran H. An optoelectronic framework enabled by low-dimensional phase-change film. Nature. 2014;**511**:206-211. DOI: 10.1038/nature13487

[6] Sun C, Wade MT, Lee Y, Orcutt JS, Alloatti L, Georgas MS, Waterman AS, Shainline JM, Avizienis RR, Lin S, Moss BR, Kumar R, Pavanello F, Atabaki AH, Cook FM, Ou AJ, Leu JC, Chen Y, Asanović K, Ram RJ, Popcvic MA, Stojanović VM. Single-chip microprocessor that communicates directly using light. Nature;**528**:534-538. DOI: 10.1038/nature16454

[7] Sorianello V, Midrio M, Contestabile G, Asselberghs I, Van Campenhout J, Huyghebaert C, Goykhman I, Ott AK, Ferrari AC, Romagnoli M. Graphene-silicon phase modulators with gigahertz bandwidth. Nature Photonics. 2018;**12**:40-44. DOI: 10.1038/s41566-017-0071-6

[8] Ríos C, Stegmaier M, Hosseini P, Wang D, Scherer T, Wright CD, Bhaskaran H, Pernice WHP. Integrated all-photonic non-volatile multi-level memory. Nature Photonics. 2015; **9**:725-732. DOI: 10.1038/NPHOTON.2015.182

[9] Bruck R, Mills B, Troia B, Thomson DJ, Gardes FY, Hu Y, Mashanovich GZ, Passaro VMN, Reed GT, Muskens OL. Device-level characterization of the flow of light in integrated photonics circuits using ultrafast photomodulation spectroscopy. Nature Photonics. 2015;**9**:54-60. DOI: 10.1038/NPHOTON.2014.274

[10] Liu L, Kumar R, Huybrechts K, Spuesens T, Roelkens G, Geluk E, Vries T, Regreny P, Van Thourout D, Baets R, Morthier G. An ultra-small, low-power, all-optical flip-flop memory on a silicon chip. Nature Photonics. 2010;**4**:182-187. DOI: 10.1038/NPHOTON.2009.268

[11] Chua LO. Memristor – The missing circuit element. IEEE Transaction on Circuit Theory. 1971;**18**:507-519

[12] Chua LO, Kang SM. Memristive devices and system. Proceedings of the IEEE. 1976;**64**: 209-223

[13] Strukov DB, Snider GS, Stewart DR, Williams RS. The missing memristor found. Nature. 2008;**453**:80-83. DOI: 10.1038/nature06932

[14] Yang JJ, Pickett MD, Li X, Ohlberg DAA, Stewart DR, Williams RS. Memristive switching mechanism for metal/oxide/metal nanodevices. Nature Nanotechnology. 2008;**3**:429-433. DOI: 10.1038/nnano.2008.160

[15] Szot K, Speier W, Bihlmayer G, Waser R. Switching the electrical resistance of individual dislocation in single-crystalline $SrTiO_3$. Nature Materials. 2006;**5**:312-320. DOI: 10.1038/nmat1614

[16] Waser R, Aono M. Nanoionics-based resistive switching memories. Nature Materials. 2007;**6**:833-840. DOI: 10.1038/nmat2023

[17] Ynag JJ, Strukov DB, Stewart DR. Memristive devices for computing. Nature Nanotechnology. 2013;**8**:13-24. DOI: 10.1038/NNANO.2012.240

[18] Bessonov AA, Kirikova MN, Petukhov DI, Allen M, Ryhänen T, Bailey MJA. Layered memristive and memcapacitive switches for printable electronics. Nature Materials. 2015;**14**:199-204. DOI: 10.1038/NMAT4135

[19] Pan F, Gao S, Chen C, Song C, Zeng F. Recent progress in resistive random access memories: Materials, switching mechanism, and performance. Materials Science and Engineering R. 2014;**83**:1-59. DOI: 10.1016/j.mser.2014.06.002

[20] Zidan MA, Strachan JP, Lu WD. The future of electronics based on memristive systems. Nature Electronics. 2018;**1**:22-29. DOI: 10.1038/s41928-017-0006-8

[21] Borghetti J, Snider GS, Kuekes PJ, Yang JJ, Stewart DR, Williams RS. 'Memristive' switches enable 'stateful' logic operations via materials implication. Nature. 2010;**464**:873-876. DOI: 10.1038/nature08940

[22] You T, Shuai Y, Luo W, Du N, Bürger D, Skorupa I, Hübner R, Henker S, Mayr C, Schüffny R, Mikolajick T, Schmidt OG, Schmidt H. Exploiting memristive $BiFeO_3$ bilayer structures for compact sequential logics. Advanced Functional Materials. 2014;**24**:3357-3365. DOI: 10.1002/adfm.201303365

[23] Xia Q, Robinett W, Cumbie MW, Banerjee N, Cardinali TJ, Yang JJ, Wu W, Li X, Tong WM, Strukov DB, Snider GS, Medeiros-Ribeiro G, Williams RS. Memristor-CMOS hybrid integrated circuits for reconfigurable logic. Nano Letters. 2009;**9**:3640-3645. DOI: 10.1021/nl901874j

[24] Prinz GA. Magnetoelectronics. Science. 1998;**282**:1660-1663. DOI: 10.1126/science.282.5394.1660

[25] Zhou Y, Li Y, Xu L, Zhong S, Sun H, Miao X. 16 Boolean logics in three steps with two anti-aerially connected memristors. Applied Physics Letters. 2015;**106**:233502. DOI: 10.1063/1.4922344

[26] Gao S, Zeng F, Wang M, Wang G, Song C, Pan F. Implementation of complete Boolean logic functions in single complementary resistive switch. Scientific Reports. 2015;**5**:15467. DOI: 10.1038/srep15467

[27] Mathieson K, Loudin J, Goetz G, Huie P, Wang L, Kamins TI, Galambos L, Smith R, Harris JS, Sher A, Palanker D. Photovoltaic retinal prosthesis with high pixel density. Nature Photonics. 2012;**6**:391-397. DOI: 10.1038/NPHOTON.2012.104

[28] Tee BCK, Chortos A, Berndt A, Nguyen AK, Tom A, McGuire A, Lin ZC, Tien K, Bae W, Wang H, Mei P, Chou H, Cui B, Deisseroth K, Ng TN, Bao Z. A skin-inspired organic digital mechanoreceptor. Science. 2015;**350**:313-316. DOI: 10.1126/science.aaa9306

[29] Li H, Zhan Q, Liu Y, Liu L, Yang H, Zuo Z, Shang T, Wang B, Li R-W. Stretchable spin valve with stable magnetic field sensitivity by ribbon-patterned periodic wrinkles. ACS Nano. 2016;**10**:4403-4409. DOI: 10.1021/acsnano.6b00034

[30] Qi D, Liu Z, Liu Y, Jiang Y, Leow WR, Pal M, Pan S, Yang H, Wang Y, Zhang X, Yu J, Li B, Yu Z, Wang W, Chen X. Highly stretchable, compliant, polymeric microelectrode arrays for in vivo electrophysiological interfacing. Advanced Materials. 2017;**29**:1702800. DOI: 10.1002/adma.201702800

[31] Son D, Lee J, Qiao S, Ghaffari R, Kim J, Lee JE, Song C, Kim SJ, Lee DJ, Jun SW, Yan S, Park M, Shin J, Do K, Lee M, Kang K, Hwang CS, Lu N, Hyeon T, Kim D-H. Multifunctional wearable devices for diagnosis and therapy of movement disorders. Nature Nanotechnology. 2014;**9**:397-404. DOI: 10.1038/NNANO.2014.38

[32] Pan C, Dong L, Zhu G, Niu S, Yu R, Yang Q, Liu Y, Wang ZL. High-resolution electroluminescent imaging of pressure distribution using a piezoelectric nanowire LED array. Nature Photonics. 2013;**7**:752-758. DOI: 10.1038/NPHOTON.2013.191

[33] Xue W, Xiao W, Shang J, Chen X, Zhu X, Pan L, Tan H, Zhang W, Ji Z, Liu G, Xu X, Ding J, Li R-W. Intrinsic and interfacial effect of electrode metals on the resistive switching behaviors of zinc oxide films. Nanotechnology. 2014;**25**:425204. DOI: 10.1088/0957-4484/25/42/425204

[34] Majumdar S, Chen B, Qin QH, Majumdar HS, van Dijken S. Electrode dependence of tunneling electroresistance and switching stability in organic ferroelectric P(VDF-TrFE)-based tunnel junctions. Advanced Functional Materials. 2017:1703273. DOI: 10.1002/adfm.201703273

[35] Zhu X, Su W, Liu Y, Hu B, Pan L, Lu W, Zhang J, Li R-W. Observation of conductance quantization in oxide-based resistive switching memory. Advanced Materials. 2012;**24**:3941-3946. DOI: 10.1002/adma.201201506

[36] Peng S, Zhuge F, Chen X, Zhu X, Hu B, Pan L, Chen B, Li R-W. Mechanism for resistive switching in an oxide-based electrochemical metallization memory. Applied Physics Letters. 2012;**100**:072101. DOI: 10.1063/1.3683523

[37] Hu B, Quhe R, Chen C, Zhuge F, Zhu X, Peng S, Chen X, Pan L, Wu Y, Zheng W, Yan Q, Lu J, Li R-W. Electrically controlled electron transfer and resistance switching in reduced graphene oxide noncovalently functionalized with thionine. Journal of Materials Chemistry. 2012;**22**:16422-16430. DOI: 10.1039/c2jm32121a

[38] Hu B, Zhu X, Chen X, Pan L, Peng S, Wu Y, Shang J, Liu G, Yan Q, Li R-W. A multilevel memory based on proton-doped polyazomethine with an excellent uniformity in

resistive switching. Journal of the American Chemical Society. 2012;**134**:17408-17411. DOI: 10.1021/ja307933t

[39] Zhu X, Shang J, Li R-W. Resistive switching effects in oxide sandwiched structures. Frontier of Materials Science. 2012;**6**:183-206. DOI: 10.1007/s11706-012-0170-8

[40] Shang J, Liu G, Yang H, Zhu X, Chen X, Tan H, Hu B, Pan L, Xue W, Li R-W. Thermally stable transparent resistive random access memory based on all-oxide heterostructures. Advanced Functional Materials. 2014;**24**:2171-2179. DOI: 10.1002/adfm.201303274

[41] Pan L, Ji Z, Yi X, Zhu X, Chen X, Shang J, Liu G, Li R-W. Metal-organic framework Nanofilm for mechanically flexible information storage applications. Advanced Functional Materials. 2015;**25**:2677-2685. DOI: 10.1002/adfm.201500449

[42] Pan L, Liu G, Li H, Meng S, Han L, Shang J, Chen B, Platero-Prats AE, Lu W, Zou X, Li R-W. A resistance-switchable and ferroelectric metal−organic framework. Journal of the American Chemical Society. 2014;**136**:17477-17483. DOI: 10.1021/ja508592f

[43] Chen C, Gao S, Tang G, Fu H, Wang G, Song C, Zeng F, Pan F. Effect of electrode materials on AlN-based bipolar and complementary resistive switching. ACS Applied Materials & Interfaces. 2013;**5**:1793-1799. DOI: 10.1021/am303128h

[44] Zhu X, Lee J, Lu WD. Iodine vacancy redistribution in organic–inorganic halide perovskite films and resistive switching effects. Advanced Materials. 2017;**29**:1700527. DOI: 0.1002/adma.201700527

[45] Zhu X, Lu WD. Optogenetics-inspired tunable synaptic functions in memristors. ACS Nano. 2018;**12**:1242-1249. DOI: 10.1021/acsnano.7b07317

[46] Lee M, Lee CB, Lee D, Lee SR, Chang M, Hur JH, Kim Y, Kim C, Seo DH, Seo S, Chung U, Yoo I, Kim K. A fast, high-endurance and scalable non-volatile memory device made from asymmetric Ta_2O_{5-x}/TaO_{2-x} bilayer structures. Nature Materials. 2011;**10**:625-630. DOI: 10.1038/NMAT3070

[47] Feng P, Mönch I, Harazim S, Huang G, Mei Y, Schmidt OG. Giant persistent photoconductivity in rough silicon nanomembranes. Nano Letters. 2009;**9**:3453-3459. DOI: 10.1021/nl9016557

[48] Corma A, Atienzar P, García H, Chane-Ching J. Hierarchically mesostructured doped CeO_2 with potential for solar-cell use. Nature Materials. 2004;**3**:394-397. DOI: 10.1038/nmat1129

[49] Peng L, Hu L, Fang X. Low-dimensional nanostructure ultraviolet photodetectors. Advanced Materials. 2013;**25**:321-5328. DOI: 10.1002/adma.201301802

[50] Chen J, Chiu Y, Li Y, Chueh C, Chen W. Nonvolatile perovskite-based photomemory with a multilevel memory behavior. Advanced Materials. 2017;**29**:1702217. DOI: 10.1002/adma.201702217

[51] Xia F, Wang H, Xiao D, Dubey M, Ramasubramaniam A. Two-dimensional material nanophotonics. Nature Photonics. 2014;**8**:899-907. DOI: 10.1038/NPHOTON.2010.271

[52] Nie R, Deng X, Feng L, Hu G, Wang Y, Yu G, Xu J. Highly sensitive and broadband organic Photodetectors with fast speed gain and large linear dynamic range at low forward bias. Small. 2017;**13**:1603260. DOI: 10.1002/smll.201603260

[53] Ungureanu M, ZazpeR, Golmar F, Stoliar P, Llopis R, Casanova F, Hueso LE. A light-controlled resistive switching memory. Advanced Materials 2012; 24: 2496–2500. DOI: 10.1002/adma.201200382

[54] Bera A, Peng H, Lourembam J, Shen Y, Sun XW, Wu T. A versatile light-switchable nanorod memory: Wurtzite ZnO on Perovskite $SrTiO_3$. Advanced Functional Materials. 2013;**23**:4977-4984. DOI: 10.1002/adfm.201300509

[55] Roy K, Padmanabhan M, Goswami S, Sai TP, Ramalingam G, Raghavan S, Ghosh A. Graphene–MoS_2 hybrid structures for multifunctional photoresponsive memory devices. Nature Nanotechnology. 2013;**8**:826-830. DOI: 10.1038/NNANO.2013.206

[56] Ye C, Peng Q, Li M, Luo J, Tang Z, Pei J, Chen J, Shuai Z, Jiang L, Song Y. Multilevel conductance switching of memory device through photoelectric effect. Journal of the American Chemical Society. 2012;**134**:20053-20059. DOI: 10.1021/ja305354y

[57] Kim YL, Jung HY, Park S, Li B, Liu F, Hao J, Kwon Y, Jung Y, Kar S. Voltage-switchable photocurrents in single-walled carbon nanotube–silicon junctions for analog and digital optoelectronics. Nature Photonics. 2014;**8**:239-243. DOI: 10.1038/NPHOTON.2014.1

[58] Lejman M, Vaudel G, Infante IC, Gemeiner P, Gusev VE, Dkhil B, Ruello P. Giant ultrafast photo-induced shear strain in ferroelectric $BiFeO_3$. Nature Communications. 2014;**5**:4301. DOI: 10.1038/ncomms5301

[59] Ahmadi M, Wu T, Hu B. A review on organic–inorganic halide perovskite photodetectors: Device engineering and fundamental physics. Advanced Materials. 2017;**29**: 1605242. DOI: 10.1002/adma.201605242

[60] Maier P, Hartmann F, Emmerling M, Schneider C, Kamp M, Höfling S, Worschech L. Electro-photo-sensitive memristor for neuromorphic and arithmetic computing. Physical Review Applied. 2016;**5**:054011. DOI: 10.1103/PhysRevApplied.5.054011

[61] Huang Y, Duan X, Cui Y, Lauhon LJ, Kim K, Lieber CM. Logic gates and computation from assembled nanowire building blocks. Science. 2001;**294**:1313-1317. DOI: 10.1126/science.1066192

[62] Bachtold A, Hadley P, Nakanishi T, Dekker C. Logic circuits with carbon nanotube transistors. Science. 2001;**294**:1317-1320. DOI: 10.1126/science.1065824

[63] Joo S, Kim T, Shin SH, Lim JY, Hong J, Song JD, Chang J, Lee H, Rhie K, Han SH, Shin K, Johnson M. Magnetic-field-controlled reconfigurable semiconductor logic. Nature. 2013; **494**:72-76. DOI: 10.1038/nature11817

[64] Terabe K, Hasegawa T, Nakayama T, Aono M. Quantized conductance atomic switch. Nature. 2005;**433**:47-50. DOI: 10.1038/nature03190

[65] Dery H, Dalal P, Cywiski L, Sham LJ. Spin-based logic in semiconductors for reconfigurable large-scale circuits. Nature. 2007;**447**:573-576. DOI: 10.1038/nature05833

[66] Tan H, Liu G, Zhu X, Yang H, Chen B, Chen X, Shang J, Lu WD, Wu Y, Li R-W. An optoelectronic resistive switching memory with integrated demodulating and arithmetic functions. Advanced Materials. 2015;**27**:2797-2803. DOI: 10.1002/adma.201500039

[67] Ney A, Pampuch C, Koch R, Ploog KH. Programmable computing with a single magnetoresistive element. Nature. 2003;**425**:485-487. DOI: 10.1038/nature02014

[68] Tan H, Liu G, Yang H, Yi X, Pan L, Shang J, Long S, Liu M, Wu Y, Li R-W. Light-gated memristor with integrated logic and memory functions. ACS Nano. 2017;**11**:11298-11305. DOI: 10.1021/acsnano.7b05762

[69] Thakoor S, Moopenn A, Daud T, Thakoor AP. Solid-state thin-film memistor for electronic neural networks. Journal of Applied Physics. 1990;**67**:3132-3135. DOI: 0.1063/1.345390

[70] Jo AH, Chang T, Ebong I, Bhadviya BB, Mazumder P, Lu W. Nanoscale memristor device as synapse in neuromorphic systems. Nano Letters. 2010;**10**:1297-1301. DOI: 10.1021/nl904092h

[71] Chang T, Jo S, Lu W. Short-term memory to long-term memory transition in a nanoscale memristor. ACS Nano. 2011;**9**:7669-7676. DOI: 10.1021/nn202983n

[72] Ohno T, Hasegawa T, Tsuruoka T, Terabe K, Gimzewski JK, Aono M. Short-term plasticity and long-term potentiation mimicked in single inorganic synapses. Nature Materials. 2011;**10**:591-595. DOI: 10.1038/NMAT3054

[73] Alibart F, Pleutin S, Bichler O, Gamrat C, Serrano-Gotarredona T, Linares-Barranco B, Vuillaume DA. Memristive nanoparticle/organic hybrid synapstor for neuroinspired computing. Advanced Functional Materials. 2012;**22**:609-616. DOI: 10.100./adfm.20111935

[74] Wang ZQ, Xu HY, Li XH, Yu H, Liu YC, Zhu XJ. Synaptic learning and memory functions achieved using oxygen ion migration/diffusion in an amorphous InGaZnO memristor. Advanced Functional Materials. 2012;**22**:2759-2765. DOI: 10.1002/adfm.201103148

[75] Yu S, Gao B, Fang Z, Yu H, Kang J, Wong HSP. A low energy oxide-based electronic synaptic device for neuromorphic visual systems with tolerance to device variation. Advanced Materials. 2013;**25**:1774-1779. DOI: 10.1002/adma.201203680

[76] Zhu LQ, Wan CJ, Guo LQ, Shi Y, Wan Q. Artificial synapse network on inorganic proton conductor for neuromorphic systems. Nature Communications. 2014;**5**:3158. DOI: 10.1038/ncomms4158

[77] Pickett MD, Medeiros-Ribeiro G, Williams RS. A scalable neuristor built with Mott memristors. Nature Materials. 2013;**12**:114-117. DOI: 10.1038/NMAT3510

[78] Neftci E, Binas J, Rutishauser U, Chicca E, Indiveri G, Douglas RJ. Synthesizing cognition in neuromorphic electronic systems. Proceedings of the National Academy of Sciences of the United States of America. 2013;**110**:E3468-E3476. DOI: 10.1073/pnas.1212083110

[79] Barbera SL, Vuillaume D, Alibart F. Filamentary switching: Synaptic plasticity through device volatility. ACS Nano. 2015;**9**:941-949. DOI: 10.1021/nn506735m

[80] Yang Y, Chen B, Lu WD. Memristive physically evolving networks enabling the emulation of heterosynaptic plasticity. Advanced Materials. 2015;**27**:7720-7727. DOI: 10.1002/adma.201503202

[81] Ignatov M, Ziegler M, Hansen M, Kohlstedt H. Memristive stochastic plasticity enablesmimicking of neural synchrony: Memristive circuit emulates an optical illusion. Science Advances. 2017;**3**:e1700849. DOI: 10.1126/sciadv.1700849

[82] Prezioso M, Merrikh-Bayat F, Hoskins BD, Adam GC, Likharev KK, Strukov DB. Training andoperation of an integrated neuromorphic network based on metal-oxide memristors. Nature. 2015;**521**:61-64. DOI: 10.1038/nature14441

[83] Tan Z, Yang R, Terabe K, Yin X, Zhang X, Guo X. Synaptic metaplasticity realized in oxide memristive devices. Advanced Materials. 2016;**28**:377-384. DOI: 10.1002/adma.201503575

[84] Tuma T, Pantazi A, Gallo ML, Sebastian A, Eleftheriou E. Stochastic phase-change neurons. Nature Nanotechnology. 2016;**11**:693-699. DOI: 10.1038/NNANO.2016.70

[85] Wang Z, Josh S, Savel'ev SE, Jiang H, Midya R, Lin P, Hu M, Ge N, Strachan JP, Li Z, Wu Q, Barnell M, Li G, Xin HL, Williams RS, Xia Q, Yang JJ. Memristors with diffusive dynamics as synaptic emulators for neuromorphic computing. Nature Materials. 2017;**16**:101-108. DOI: 10.1038/NMAT4756

[86] Sheridan PM, Cai F, Du C, Ma W, Zhang Z, Lu WD. Sparse coding with memristor networks. Nature Nanotechnology. 2017;**12**:784-789. DOI: 10.1038/NNANO.2017.83

[87] Kumar S, Strachan JP, Williams RS. Chaotic dynamics in nanoscale NbO_2 Mott memristors for analogue computing. Nature. 2017;**548**:318-321. DOI: 10.1038/nature23307

[88] Lee M, Lee W, Choi S, Jo J, Kim J, Park SK, Kim Y. Brain-inspired photonic neuromorphic devices using photodynamic amorphous oxide semiconductors and their persistent photoconductivity. Advanced Materials. 2017;**29**:1700951. DOI: 10.1002/adma.201700951

[89] Choi C, Choi MK, Liu S, Kim MS, Park OK, Im C, Kim J, Qin X, Lee GJ, Cho KW, Kim M, Joh E, Lee J, Son D, Kwon S, Jeon NL, Song YM, Lu N, Kim D. Human eye-inspired soft optoelectronic device using high-density MoS_2-graphene curved image sensor array. Nature Communications. 2017;**8**:1664. DOI: 10.1038/s41467-017-01824-6

[90] Maya-Vetencourt JF, Ghezzi D, Antognazza MR, Colombo E, Mete M, Feyen P, Desii A, Buschiazzo A, Paolo MD, Marco SD, Ticconi F, Emionite L, Shmal D, Marini C, Donelli I, Freddi G, Maccarone R, Bisti S, Sambuceti G, Pertile G, Lanzani G, Benfenati F. A fully organic retinal prosthesis restores vision in a rat model of degenerative blindness. Nature Materials. 2017;**16**:681-689. DOI: 10.1038/NMAT4874

[91] Ko HC, Stoykovich MP, Song J, Malyarchuk V, Cho WM, Yu C, Geddes III JB, Xiao J, Wang S, Huang Y, Rogers JA. A hemispherical electronic eye camera based on compressible silicon optoelectronics. Nature. 2008;**454**:748-753. DOI: 10.1038/nature07113

[92] Chen S, Lou Z, Chen D, Shen G. An artificial flexible visual memory system based on an UV-motivated memristor. Advanced Materials. 2017;**29**:1705400. DOI: 10.1002/adma.201705400

[93] Yang H, Wang B, Zhu X, Shang J, Chen B, Li R-W. Modulation of physical properties of oxide thin films by multiple fields. Chinese Physics B. 2016;**25**:067303. DOI: 10.1088/1674-1056/25/6/067303

[94] Xue W, Liu G, Zhong Z, Dai Y, Shang J, Liu Y, Yang H, Yi X, Tan H, Pan L, Gao S, Ding J, Xu X-H, Li R-W. A 1D vanadium dioxide nanochannel constructed via electric-field-induced ion transport and its superior metal–insulator transition. Advanced Materials. 2017;**29**:1702162. DOI: 10.1002/adma.201702162

[95] Chen X, Zhu X, Xiao W, Liu G, Feng YP, Ding J, Li R-W. Nanoscale magnetization reversal caused by electric field-induced ion migration and redistribution in cobalt ferrite thin films. ACS Nano. 2015;**9**:4210-4218. DOI: 10.1021/acsnano.5b00456

[96] Zhu X, Zhou J, Chen L, Guo S, Liu G, Li R-W, Lu WD. In situ nanoscale electric field control of magnetism by nanoionics. Advanced Materials. 2016;**28**:7658-7665. DOI: 10.1002/adma.201601425

[97] Yao L, Inkinen S, van Dijken S. Direct observation of oxygen vacancy-driven structural and resistive phase transitions in $La_{2/3}Sr_{1/3}MnO_3$. Nature Communications. 2017;**8**:14544. DOI: 10.1038/ncomms14544

[98] Kim T, McCall JG, Jung YH, Huang X, Siuda ER, Li Y, Song J, Song YM, Pao HA, Kim R, Lu C, Lee SD, Song I, Shin G, Al-Hasani R, Kim S, Tan MP, Huang Y, Omenetto FG, Rogers JA, Bruchas MR. Injectable, cellular-scale optoelectronics with applications for wireless optogenetics. Science. 2013;**340**:211-216. DOI: 10.1126/science.1232437

[99] Wu F, Stark E, Ku P, Wise KD, Buzsaki G, Yoon E. Monolithically integrated uLEDs on silicon neural probes for high-resolution optogenetic studies in behaving animals. Neuron. 2015;**88**:1136-1148. DOI: 10.1016/j.neuron.2015.10.032

[100] Canales A, Jia X, Froriep UP, Koppes RA, Tringides CM, Selvidge J, Lu C, Hou C, Wei L, Flink Y, Anikeeva P. Multifunctional fibers for simultaneous optical, electrical and chemical interrogation of neural circuits *in vivo*. Nature Biotechnology. 2015;**33**:277-284. DOI: 10.1038/nbt.3093

Chapter 4

Nonlinear Dynamics in Optoelectronics Structures with Quantum Well

Andreea Rodica Sterian

Additional information is available at the end of the chapter

http://dx.doi.org/10.5772/intechopen.74557

Abstract

The author presents some results on nonlinear dynamics in optoelectronics nanostructures as lasers with quantum wells and quantum well solar cells using mathematical modeling and numerical simulations of the phenomena which take place in such kinds of structures. The nonlinear dynamics takes the complexity of the phenomena into account, which govern the field-substance interaction. Computational software was elaborated to study the nonlinear phenomena in such quantum devices, which put into evidence their complex nonlinear dynamics, characterized by bifurcation points and chaos, and the critical values of the parameters being determined. The mathematical modeling and numerical simulations for the quantum well solar cells for optimizing the values of their optical parameters (refraction index, reflectance, and absorption) were also analyzed, so that the conversion efficiency of the devices can be improved. Although in our study we have considered only rectangular quantum wells, the hybrid model allows computing the optimum values of the parameters whatsoever the form of the quantum wells. The developed numerical models and the obtained results are consistent with the existing data in the literature for the optoelectronics of quantum well structures, having important implications in the applications.

Keywords: quantum well laser, quantum well solar cell, hybrid model, bifurcation diagram, chaotic state, quantum engineering, chaos masking

1. Introduction

The nonlinear dynamics is treated taking into account the complexity of the phenomena which govern the field-substance interaction including the dissipative phenomena [1–6]. Computational software was elaborated to study the nonlinear phenomena in such kinds of quantum devices [7–9].

A quantum well (QW) structure improves the functioning characteristics of laser diodes and of the solar cells as the emitted wavelength depends on nanostructure dimension (quantum size effect) [3, 10–13]. Such a structure is one in which the active region of the device is so narrow that quantum confinement occurs, according to quantum mechanics. The wavelength of the light emitted by a quantum well laser is determined by the width of the active region rather than just the band gap of the material from which the device is realized. Consequently, much shorter wavelengths can be obtained from quantum well lasers than from conventional laser diodes using a particular semiconductor material. The realization of quantum well structures represents cutting-edge technological advances in the field of semiconductor optoelectronics structures. These devices, unlike the classic ones, have the active area in the form of a periodic structure of semiconductor layers having different forbidden energy bands. These layers have very small thicknesses (nanometer units), their deposition being possible using advanced technologies and special deposition techniques.

In this chapter, first, we shall recall different forms of the rate equations used to take into account the complexity of the phenomena which govern the field-substance interaction. Based on computational software which was elaborated for the rate equation models presented, the phenomena were numerically studied in such a kind of quantum devices, and the utility of these models on some very simple examples and applications by different methods of simulations [14–21] was illustrated.

Second, we treat the complex nonlinear dynamics, characterized by bifurcation points and chaos, the critical values of the parameters being determined. The work emphasizes the variety of dynamical modes of operation of a semiconductor laser as a result of modulation of the injection current [22–28].

The third part of the chapter is dedicated to the particularities of the quantum well solar cells. The simulation results for the optical parameters (refraction index, reflectance, absorption coefficient) are presented as well as those for the optimization of the quantum efficiency of QW solar cells [21, 29–34].

Finally, as the application of the chaotic dynamics, an optical communications channel with chaotic laser signals is presented to demonstrate the important implications of these kinds of systems in quantum engineering and for transmission and processing of the optical information [35–40].

2. Modeling methods and techniques for quantum well lasers

2.1. Standard rate equations

Several levels of descriptions and modeling of field-substance interaction are known in the theory of lasers, depending on the classical or quantum character of the evolution equations, describing the two subsystems in interaction, the substance and the electromagnetic field, the laser system being a dissipative structure which takes on self-organizing phenomena, far from equilibrium. Besides the phenomenological description of lasers owing to Einstein, who discovered the stimulated emission in 1016, which makes the amplification of coherent radiation in lasers possible, the theories developed for laser phenomena description are *the thermodynamic* theory, based on the equations of the rates as equations of balance for the populations of the laser levels and the density of the photons in the laser cavity, considering the dissipation; *the semi-classical* theory (or *semi-quantum)* in which the population equations are quantum, established as motion equations for the quantum operators corresponding to the populations of the levels involved and the field equation which is the classical equation describing the electromagnetic field in the laser medium, polarization of the medium being the source of the field; and *the quantum* theory in which both the substance and the electromagnetic field are described by quantum equations of evolution. The abovementioned theories are complementary to each other and are used according to the phenomena whose description is being followed in the studied issue or application.

As a system, the laser is described by the equations of two nonlinear coupled oscillators, a quantum oscillator represented by the polarization of the active medium and a classical oscillator which is the electromagnetic field from the optical resonant cavity. By pumping, the system receives external energy to realize the population inversion. Above the threshold, the oscillation condition being accomplished, the energy accumulated in the active medium is liberated through stimulated emission, under the form of the coherent light beam of laser.

The main quantum well laser model used in this chapter is based on the description of semiconductor lasers using the thermodynamic theory of the rate equations [14].

While the first models were based on one pair of equations to describe the density of photons and carriers in the active region, recent approaches include additional rate equations to take into account, and carriers transport between the active region and the adjacent layers of the structure as in Ref.s [15–18].

It can be observed that in most cases, the rate equations lead to multiple solutions, although only one solution is correct. Javro and Kang [19] showed that incorrect solutions or without physical sense can be eliminated or avoided through a change of variables in the rate equations. However, the transformations used are available under certain conditions, and for some cases, they give unrealistic solutions. These shortcomings are caused mainly due to the linear character of the gain-saturation coefficient. A more general expression of the gain-saturation coefficient, proposed by Channin, can be used to obtain models for operation regimes having a solution unique. Agrawal suggests another expression for this coefficient, which is also suitable. As is shown, any of these two forms of the gain-saturation coefficient can be used to obtain models with a solution unique to the operation regime.

2.1.1. The model with linear gain saturation

One of the prevailing laser diode models is based on a set of rate equations. The rigorous derivation of these equations originates from Maxwell equations with a quantum mechanical approach for the induced polarization. However, the rate equations could also be derived by considering physical phenomena described as in [3].

The population equation is as follows:

$$\frac{dN}{dt} = \frac{I}{qV_{act}} - g_0(N - N_0)(1 - \varepsilon S)S - \frac{N}{\tau_p} + \frac{N_e}{\tau_n} \tag{1}$$

Similarly, the photon density equation is written as.

$$\frac{dS}{dt} = \Gamma g_0(N - N_0)(1 - \varepsilon S)S + \frac{\Gamma \beta N}{\tau_n} - \frac{S}{\tau_p} \tag{2}$$

The photon density S reported the output power Pf as described by Eq. (3):

$$\frac{S}{P_f} = \frac{\Gamma \tau_p \lambda_0}{V_{act} \eta hc} = \vartheta \tag{3}$$

Eq. (1) relates the rate of change in carrier concentration N to the drive current I, the carrier combination rate and the stimulated-emission rate S. Eq. (2) relates the rate of change in photon density S to photon loss, the rate of coupled recombination into the lasing mode, and the stimulated-emission rate. The photon density S to the output power P_f is described by Eq. (3). The other parameters used have well-known significances as in Ref. [14]. This simple model can be directly implemented with Matlab Simulink.

2.1.2. *The model with nonlinear gain saturation*

An alternate version of the standard rate equations ensures us that for a nonnegative injection current, one nonnegative solution exists for density of both carriers and photons. The equations treated henceforth are the more generalized versions of Eqs. (1) and (2) with the linear gain-saturation term replaced by the term proposed by either Channin or Agrawal. The new equations are shown below as in Ref. [20]:

$$\frac{dN}{dt} = \frac{\eta_i I}{qN_w V_{act}} - R_w(N) - \Gamma_c v_{gr} \frac{\alpha(N)}{\Phi(S)} S \tag{4}$$

$$\frac{dS}{dt} = -\frac{S}{\tau_p} + N_w R_{w\beta}(N) + N_w \Gamma_c v_{gr} \frac{\alpha(N)}{\Phi(S)} S \tag{5}$$

$$\frac{S}{P_f} = \frac{\lambda \tau_p}{\eta_c V_{act} hc} = \vartheta \tag{6}$$

Eq. (4) relates the rate of change in carrier concentration N with the injection current, the carrier recombination rate and the stimulated-emission rate. In order to account for different recombination mechanisms, it considers $R_w(N) = AN + BN^2 + CN^3$, where A, B, and C are the unimolecular, radiative, and Auger recombination coefficient, respectively. Eq. (5) relates the rate of change in photon density to photon loss, the rate of coupled recombination into the lasing mode, and the stimulated-emission rate. In the above equations, the two gain-saturation terms are

$$\alpha(N) = G_0 \ln\left(\frac{R_w(N)}{R_w(N_0)}\right) \tag{7}$$

$$\alpha(N) = g_l G_0 \left(\frac{N}{N_0} - 1\right) \tag{8}$$

where G_0 is the gain coefficient per quantum well, N_0 is the optical transparency density, and g_l is a factor obtained when linearizing the logarithmic gain around N_0. Specifically,

$$g_l = \frac{AN_0 + 2BN_0{}^2 + 3CN_0{}^3}{AN_0 + BN_0{}^2 + CN_0{}^3} \tag{9}$$

The gain-saturation function can take on one of the following two forms:

$$\phi^{-1}(S) = \frac{1}{1 + \varepsilon\Gamma_c S} \tag{10}$$

$$\phi^{-1}(S) = \frac{1}{\sqrt{1 + \varepsilon\Gamma_c S}} \tag{11}$$

Using the approach taken in [11, 18, 20], an equivalent circuit model based on the above equations can be implemented in SPICE. Unlike models based on the rate equations that use a linear gain-saturation term, this circuit model is applicable for all nonnegative values of injection current.

2.2. Numerical experiments in MathCad

A comparative study of the models presented above for quantum well lasers is possible by numerical integration in MathCad of the corresponding equations to find the response for different types of pumping signals. The model with linear gain saturation, given by Eqs. (1) and (2), was integrated for a constant injection current, the corresponding waveforms for the optical output power being illustrated in [10]. The nonlinear gain-saturation model of Eqs. (4) and (6) was integrated for an injection current rectangular (**Figure 1**), which for some periods can be written under the form.

$$\begin{aligned} I_i(t) = 10^{-8} + 0{,}01 + 0{,}25 I_i\left(t - 2\cdot 10^{-9}\right) + \\ + 0{,}25 I_i\left(t - 7\cdot 10^{-9}\right) + 0{,}25 I_i\left(t - 12\cdot 10^{-9}\right). \end{aligned} \tag{12}$$

In general, all models studied give satisfactory results for the study of the transient and dynamic regime at low injection levels. At high injection rates, the numerical results obtained show the specific limits of each model, being consistent with the theoretical analysis.

2.3. Methods of modeling solutions of the rate equations

In this section, the two methods of modeling the solutions of the rate equations analyzed in [14] are presented. The first modeling technique is based on standard rate equations with a set

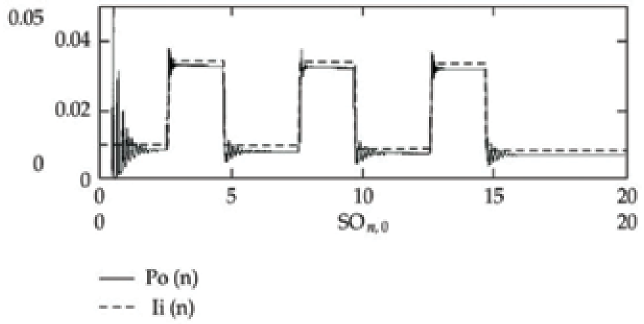

Figure 1. The waveforms of optical output power for an injection current rectangular in the model with nonlinear gain saturation.

of parameters given directly in Simulink. The second model is based on the standard rate equations that use a gain-saturation term and can be implemented in SPICE.

2.3.1. The Simulink modeling technique

This simple model can be directly implemented with Simulink like in **Figure 2**.

The input parameter from a signal generator is *I*, while *S*, *N* and *Pf* are the output parameters. All the parameters in the rate equations can be modified before the simulation starts as in all specialized papers [14–16].

With the above model, different signals can be used as input current for the quantum well laser. They show that the theoretical response of the equations is good when compared with real results that are expected in applications. Signals like saw tooth and sine types are used as input. The results are shown in **Figure 3**. They show very fast response at a low level of the current. Low threshold current is the main feature of quantum well lasers, and it is directly shown for the basic form of rate equation. The simulation is not perfect, and this is because of negative solutions for *N* and *S* and high power solution of the equations.

2.3.2. The SPICE modeling technique

In an alternate version of the rate equations, the linear gain-saturation term is replaced by the term proposed by either Channin or Agrawal [10, 15, 20]. Using the approach taken in [11, 14], an equivalent circuit model based on the above equations can be implemented in SPICE. Unlike models based on the rate equations that use a linear gain-saturation term, this circuit model is applicable for all nonnegative values of injection current.

In **Figure 4**, the circuit implementation is shown. This equivalent circuit can be obtained through suitable handling of the rate equations and by the transformations of variables. Diodes D1 and D2 and current sources Ic1 and Ic2 are modeling the linear recombination and charge storage in the device, while Br1 and Bs1 are modeling the effects of additional recombination mechanisms and stimulated emission, respectively, on the charges carrier density.

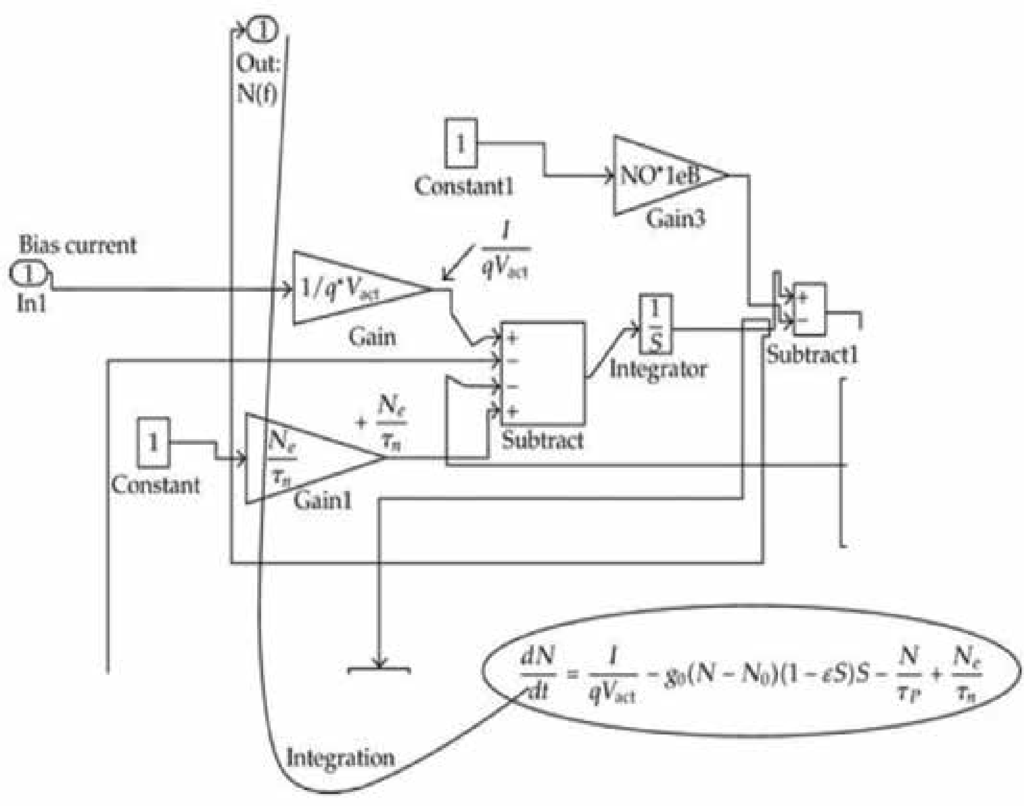

Figure 2. The Simulink block scheme of the rate equations.

The components Rph and Cph of the circuit help to model the time variation of the photon density under the effects of spontaneous and stimulated emission, which are accounted for by Br2 and Bs2, respectively. Finally, the source Bpf produces the optical output power of the laser in the form of a voltage. The circuit equations are given as follows:

$$I = I_{T1} + I_{D1} + I_{C1} + B_{r1} + B_{s1} \text{ where } I_{T1} = I_{D1} + I_{C1} \tag{13}$$

$$2\tau_p \frac{dm}{dt} + m = B_{r2} + B_{s2} \quad \text{and} \quad B_{pf} = (m + \delta)^2 \tag{14}$$

$$I_{D1} = \frac{qN_w V_{act} N_e}{2\eta_i \tau_n} \left[\exp\left(\frac{qV}{nkT} \right) - 1 \right] \tag{15}$$

$$I_{D2} = \frac{qN_w V_{act} N_e}{2\eta_i \tau_n} \left[\exp\left(\frac{qV}{nkT} \right) - 1 + \frac{2q\tau_p}{nkT} \exp\left(\frac{qV}{nkT} \right) \frac{dV}{dt} \right] \tag{16}$$

$$I_{c1} = I_{c2} = \frac{qN_w V_{act} N_e}{2\eta_i \tau_n} \tag{17}$$

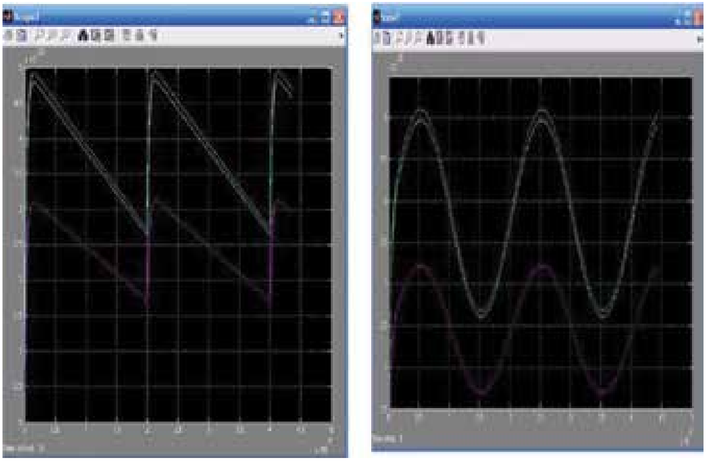

Figure 3. Output for saw tooth input signal of 10 mA amplitude and frequency of 5 MHz, and the output for the input signal sinusoidally having the same values for the amplitude and frequency.

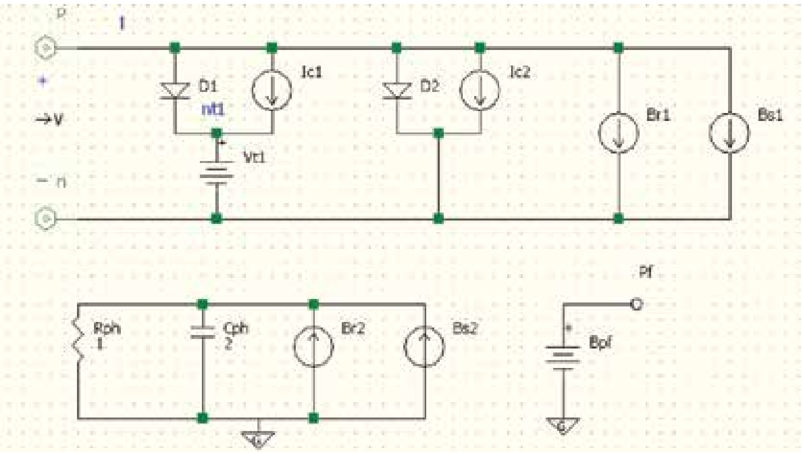

Figure 4. The electric circuit corresponding to the rate equation model.

$$B_{r1} = \frac{qN_w V_{act}}{\eta_i} R_{\omega 2}(\Theta I_{T1}) \tag{18}$$

$$B_{s1} = \frac{\lambda \tau_p N_w \Gamma_c v_{gr}}{\eta i \eta_c hc} \frac{\alpha(\Theta I_{T1})}{\phi\left(\vartheta(m+\delta)^2\right)} \vartheta(m+\delta)^2 \tag{19}$$

$$B_{r2} = \frac{N_w \eta_c V_{act} hc}{\lambda \vartheta(m+\delta)} R_{\omega 2}(\Theta I_{T1}) \tag{20}$$

$$B_{s2} = \tau_p N_w \Gamma_c v_{gr} \frac{\alpha(\Theta I_{T1})}{\phi\left(\vartheta(m+\delta)^2\right)} (m+\delta) - \delta \tag{21}$$

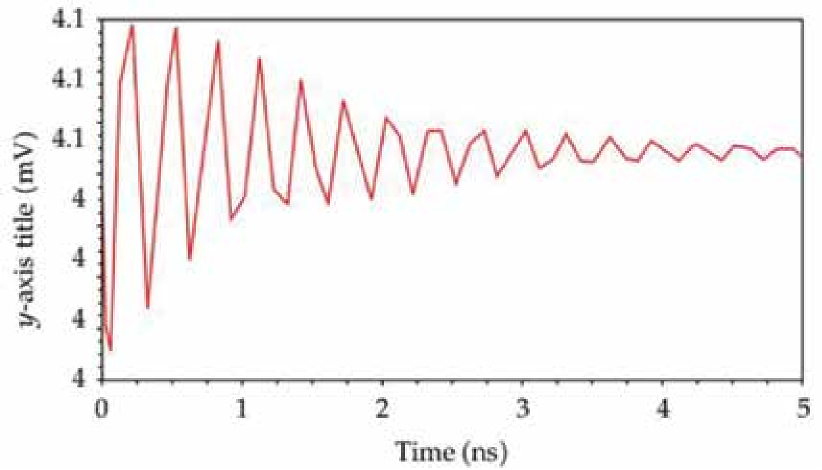

Figure 5. Transient output power response between 0 and 5 ns.

We implemented the SPICE netlist in AIM-SPICE, but calculating the parameters in the netlist is time-consuming. **Figure 5** shows results from PSPICE simulation with simple DC sweep and transient output power in response. (Obs: output power is given in Volt, because SPICE cannot have output variables in Watt).

Modifying one parameter will result in new calculations and new SPICE netlist. Simulations are not limited to SPICE, any all-purpose circuit simulators can be used to get similar results. Future development software that integrates circuit simulation and other modeling methods for quantum well lasers can be built to have a tool that models these devices from all points of view.

As a future development, we mention the method of the MATH package Simulink to simulate the behavior of the quantum well laser diodes with distributed feedback using the rate equations [16].

A more deeper additional can be the finite-difference time-domain (FDTD) method and then all are bundled in one software package for more simulation options [34].

3. Nonlinear dynamics of the quantum well laser

3.1. Modulation of the quantum well laser

We study the amplitude modulation of the injection current [22, 23]:

$$I = I_b[1 + m \sin(2\pi f t)] \tag{22}$$

where I_b is the polarization current and m modulation index:

$$m = \frac{I_m}{I_b} \tag{23}$$

where I_m is the amplitude of the modulating signal $(i_m = I_m \sin(\omega t))$, f being the modulation frequency.

3.2. The model of small signal and the frequency response

In this section, we analyze the low signal model and the frequency response of the laser for different polarization currents. The small signal model can be obtained from the equations of the rates, with two equations of populations [10], replacing I, N_b, N_w, and S with $N_{b0} + \Delta N_b e^{j\omega t}$, $I_b + \Delta I e^{j\omega t}$, $N_{w0} + \Delta N_w e^{j\omega t}$, respectively, $S_0 + \Delta S e^{j\omega t}$, where I_b is the polarization current. The quantities N_{b0}, N_{w0}, S_0 are the solution of the considered rate equations, when the laser is pumped with the polarization current I_b, ΔI is the amplitude of a small perturbation overlaid on I_b and $\Delta N_b, \Delta N_w, \Delta S$ are the amplitudes of population densities and photon density corresponding to a small excitation. The frequency response of the laser is represented graphically in **Figure 6** using system (24) where N_{w0} and S_0 are calculated by means of the large signal model, placing $I(t) = I_b$ for the large t. The simulation parameters can be found in [10]

$$\begin{pmatrix} -\frac{i\Delta I}{qV_w} \\ 0 \\ 0 \end{pmatrix} =$$

$$= \begin{pmatrix} \overline{\omega} - \frac{i}{\tau_{cap}} - \frac{i}{\tau_n} & \frac{i}{\tau_{esc}} & 0 \\ \frac{i}{\tau_{cap}} & \omega - \frac{i}{\tau_{esc}} - \frac{i}{\tau_n} - i g_0 \frac{S_0}{1+\varepsilon S_0} & -i\frac{g_0}{(1+\varepsilon S_0)^2}(N_{w0} - N_0) \\ 0 & i\Gamma g_0 \frac{S_0}{1+\varepsilon S_0} + i\Gamma \frac{\beta_{sp}}{\tau_n} & \overline{\omega} + i\Gamma\frac{g_0}{(1+\varepsilon S_0)^2}(N_{w0} - N_0) - \frac{i}{\tau_p} \end{pmatrix} \cdot \begin{pmatrix} N_b \\ N_w \\ S \end{pmatrix} \tag{24}$$

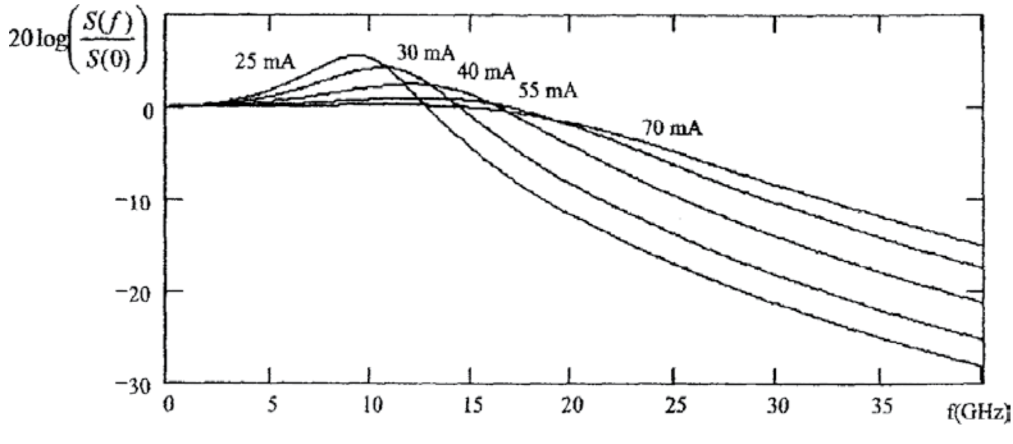

Figure 6. Frequency response of QW laser for $I_b = 25; 30; 40; 55; 70$ mA.

In the preceding paragraph, a small signal pattern was derived to analyze the frequency response of a QW laser for different polarization currents I_b. By increasing this current in a certain range, the laser band, the maximum modulation frequency increases.

As shown in the subsequent text, the QW laser band can be further extended if the gain of the active medium g_0 (e.g., carrier temperature in the active region of the laser) is modulated additionally to I. For this purpose, a new low signal model is derived. This time, we use the equations of the large signal pattern with one population equation [10, 20]. Optical gain is no longer a constant, having the form $g(t) = g_0(1 + \Delta P \sin\omega t)$, where ΔP represents a small fraction of g_0. The system of linear equations of the small signal pattern written in a matrix form easily implementable in MathCad has the form:

$$\begin{pmatrix} \dfrac{-i\Delta I}{qV_{act}} + i(1-\varepsilon S)Sg_0(N-N_0)\Delta P \\ -i(1-\varepsilon S)Sg_0\Gamma(N-N_0)\Delta P \end{pmatrix} = \\ = \begin{pmatrix} \overline{\omega} - ig_0S(1-\varepsilon S) - \dfrac{i}{\tau_n} & -i(1-2\varepsilon S)g_0(N-N_0) \\ i\Gamma g_0S(1-\varepsilon S) + i\Gamma\beta\dfrac{1}{\tau_n} & \overline{\omega} + i(1-2\varepsilon S)g_0\Gamma(N-N_0) - \dfrac{i}{\tau_p} \end{pmatrix} \cdot \begin{pmatrix} N \\ S \end{pmatrix} \quad . \tag{25}$$

The results obtained by simulations for the photon density correspond to the three modulation cases and are given in [10]: (1) modulation of injection current and simultaneously of g; (2) the simple modulation of I; and (3) simple modulation of g, being presented in **Figure 7** (in all cases, I_b = 50 mA).

An increase in the bandwidth of the laser is observed when both I and g_0 are simultaneously modulated.

3.3. Routes to chaos and bifurcation diagrams

In **Figure 8**, the variation of the photon density S for different modulation indices as in [28] is compared.

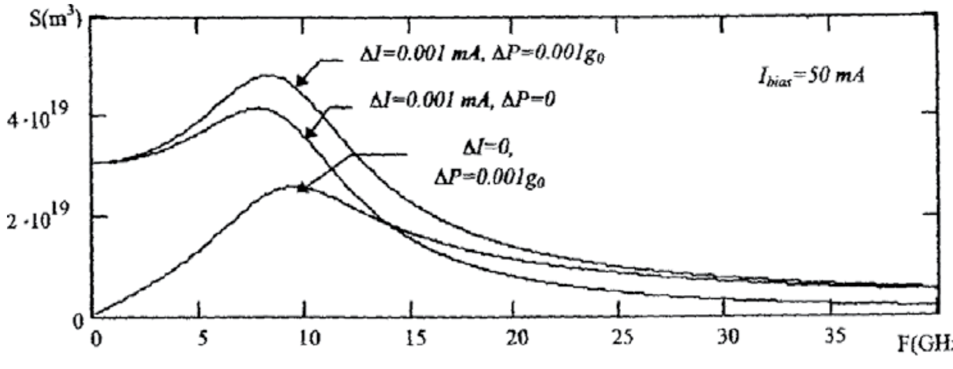

Figure 7. The photon density for three modulation cases: (1) modulation of injection current and simultaneously of g; (2) the simple modulation of I; and (3) simple modulation of g.

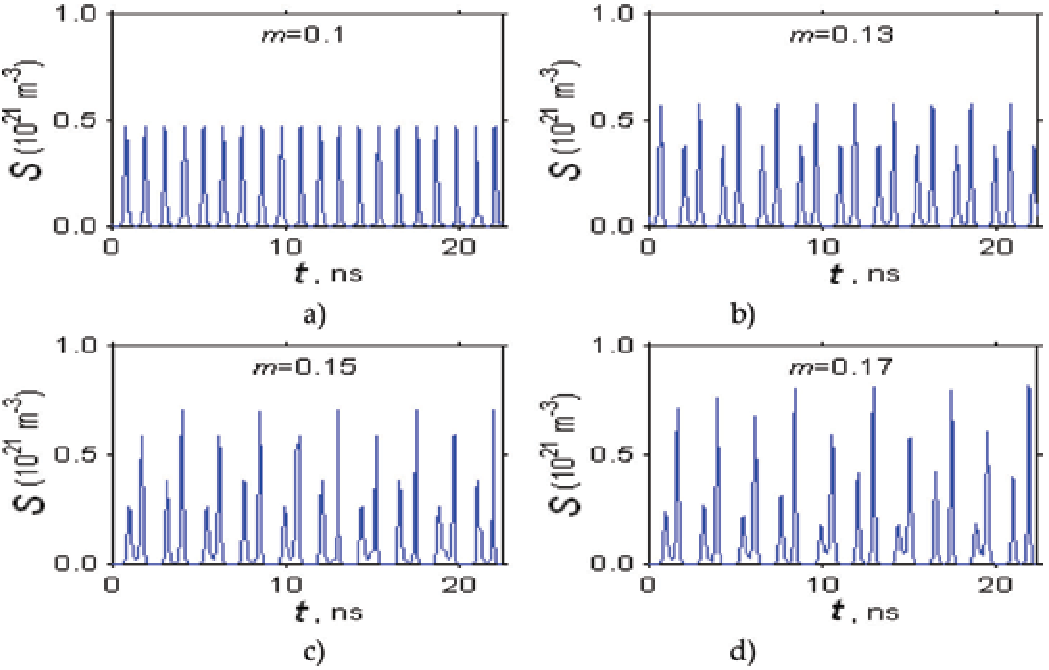

Figure 8. Time dependence of photon density for different modulation indices. The 1 T periodic signal in (a) becomes a double period (2 T) in (b), with the 4 T period in (c) and chaotically in (d).

Such a route to chaos with the increase of m by doubling of the period can also be presented qualitatively in the phase space as in [10, 28]. Knowing the hierarchy of instabilities of laser devices is useful in designing and calculating stable operating regimes in applications. Next, we analyze the bifurcation diagram of the peak photon density according to the modulation index (**Figure 9**) in the direct sense (with the increase of m) and vice versa (with the decrease of m) for a modulation cycle as an indicator of the evolution of the system.

In the chaotic region, there are periodic dynamic windows and a hysteresis dynamics (marked with arrows in **Figure 9**). In **Figure 10**, another bifurcation diagram is presented for a modulation frequency $f = f_0/2$, the other parameters remaining unchanged.

This result shows the complexity of system dynamics, without this complexity to be fully elucidated to date [12].

3.4. Rate equations with noise sources

The noise sources F_n and F_s are considered in the rate equations as in [27, 28]:

$$\frac{\mathrm{d}N}{\mathrm{d}t} = \frac{I}{qV_{act}} - g_0(N - N_0)S - \frac{N}{\tau_n} + F_n(t) \tag{26}$$

$$\frac{\mathrm{d}S}{\mathrm{d}t} = g_0(N - N_0)S - \frac{S}{\tau_p} + \gamma\frac{N}{\tau_n} + F_s(t) \tag{27}$$

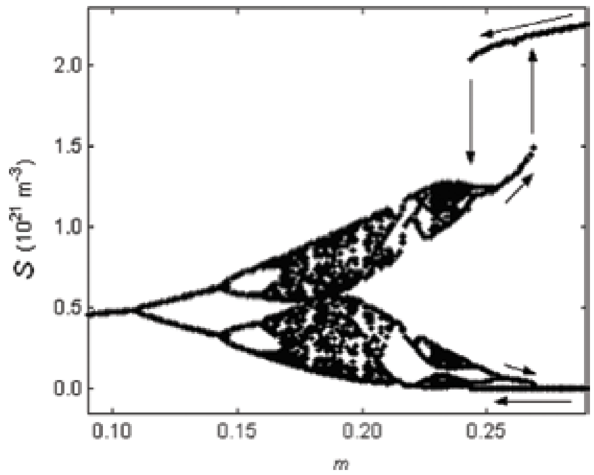

Figure 9. Bifurcation diagram of photon density depending on the modulation index.

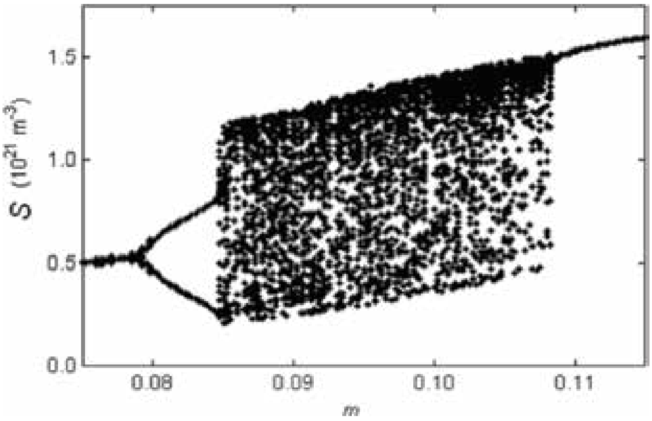

Figure 10. Bifurcation diagram for $f = f_0/2$.

In the Markoff approximation, noise sources are Gaussian variables of zero average, δ correlated, as

$$\langle F_\mathrm{n}(t)\rangle = 0, \quad \langle F_\mathrm{n}(t)F_\mathrm{n}(t')\rangle = V_\mathrm{n}^2\delta(t-t') \tag{28}$$

$$\langle F_\mathrm{s}(t)\rangle = 0, \quad \langle F_\mathrm{s}(t)F_\mathrm{s}(t')\rangle = V_\mathrm{s}^2\delta(t-t') \tag{29}$$

$$\langle F_\mathrm{n}(t)F_\mathrm{s}(t')\rangle = rV_\mathrm{n}V_\mathrm{s}\delta(t-t') \tag{30}$$

In the above expressions, V_n^2 and V_s^2, there are variances of the random variables F_n and F_s, respectively, and r a correlation coefficient. See reference [28] for details. In the numerical modeling of Eqs. (26) and (27), it considers, for the intervals Δt, the autocorrelation function (7.81) of the form:

$$\langle F_{\mathrm{n}}(t)F_{\mathrm{n}}(t')\rangle = \begin{cases} V_{\mathrm{n}}^2/\Delta t, & pentru \quad |t-t'| < \Delta t \\ 0, & pentru \quad |t-t'| > \Delta t. \end{cases} \tag{31}$$

This condition leads to the representation of

$$F_n = \left(V_n/\sqrt{\Delta t}\right)x_n \tag{32}$$

where x_n is a Gaussian random variable of zero average and unit variance.

By using Gaussian random numbers supplied by MATLAB functions, integration is achieved in much smaller steps Δt relative to the modulation period. Numerical calculations show that no matter how small the noise is, it disturbs the attractors and can even produce transitions between coexisting attractors.

For a modulation index $m = 0,265$, two stable attractors coexist (**Figure 11a** and **b**), but the presence of noise induces transitions from one attractor to another as is shown in **Figure 11c**. See references [27, 28].

The complexity of phenomena taking place in a laser diode in the presence of modulation is correlated with the nonlinearity of the stimulated-emission rate $g_0(N-N_0)S$, which will be analyzed extensively in the following paragraph.

3.5. Nonlinear dynamics of the MQW: A case study

This section presents a case study in which the nonlinear dynamics of the quantum hole laser is systematically analyzed on the basis of two population equations proposed by Nagarajan et al. [26]. In this model, a quantum well structure is modeled as a single quantum well structure, "concentrating" both the quantum wells and the barriers together.

Rate equations were solved numerically. The simulations were performed in the Matlab programming language using a fourth-order Runge–Kutta scheme [10].

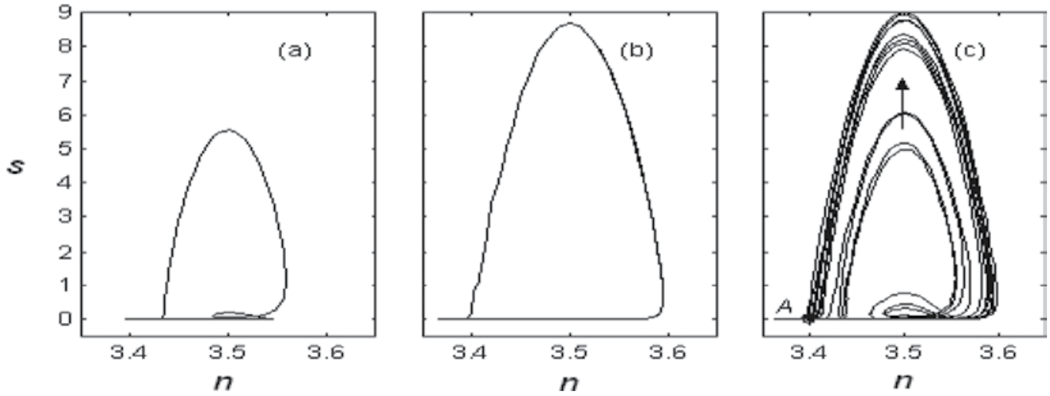

Figure 11. Influence of Gaussian noise on the evolution of the system in phases.

Detailed numerical investigations have shown that for lower frequencies with respect to the relaxation frequency, system dynamics is periodic with the radiofrequency modulator signal period.

For a small enough modulation index $\left(m = \frac{I_{RF}}{I_{DC}} << 1\right)$, the periodic sinusoidal mode is obtained. The output power of the laser is sinusoidal, with the injection current (**Figure 12a**).

In the case of increasing of the modulation index and by approximating the frequency modulation with the frequency of the relaxation oscillations, a pulse operation mode (**Figure 12b**) is obtained, with a duration of the picoseconds (ultrashort pulses), the laser being used as a pulse source for optical communications.

For higher frequencies in relation to the resonance frequency of the system and modulation indices over a critical value, the phenomenon of doubling the frequency occurs.

The corresponding bifurcation diagrams are shown in [12]. At a value of parameter m for which the dynamics is 2 T (nT), the representation consists of two points (n points). Higher modulation frequencies cause multiple bifurcation points, including chaotic dynamics for certain parameter values (f = 8 GHz, in **Figure 13**).

Also in **Figure 13**, the dependence of the critical modulation index (frequency bifurcation) is observed (for f = 12 GHz, m_{critic} is higher than for f = 7 GHz). **Figure 14** shows the laser nonlinear dynamics 4 T (**Figure 14a**) and the corresponding two-dimensional representation in the phase space (**Figure 14b**), for I_{DC} = 20 mA, f = 8 GHz, and m = 3.5. For an increased modulation index, m = 5.5, the dynamics becomes chaotic (**Figure 14c** and **d**).

The behavior is similar for other over-threshold injection current values, but there is an increasing dependence of the modulation index on doubling the period with the polarization current.

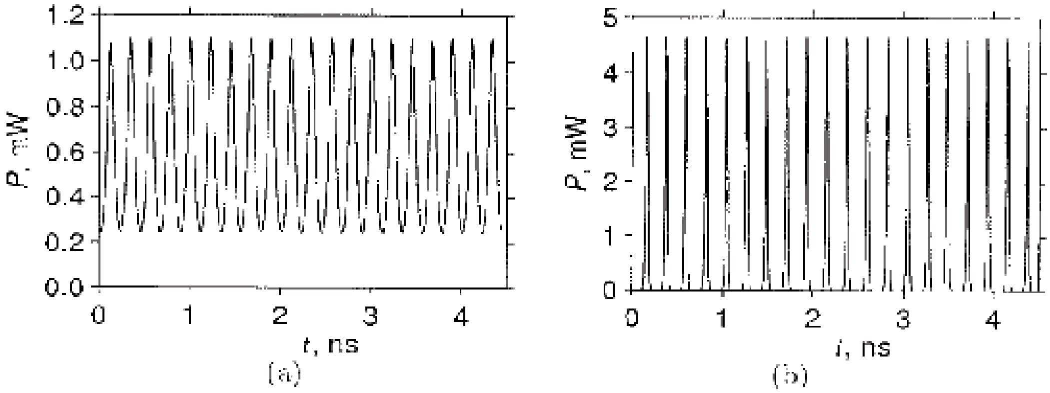

Figure 12. (a) Output power of the laser, sinusoidal for low signal modulation (m = 0,1); (b) the same pulse dependence, for m = 2 (I = 20 mA, f = 4.5 GHz).

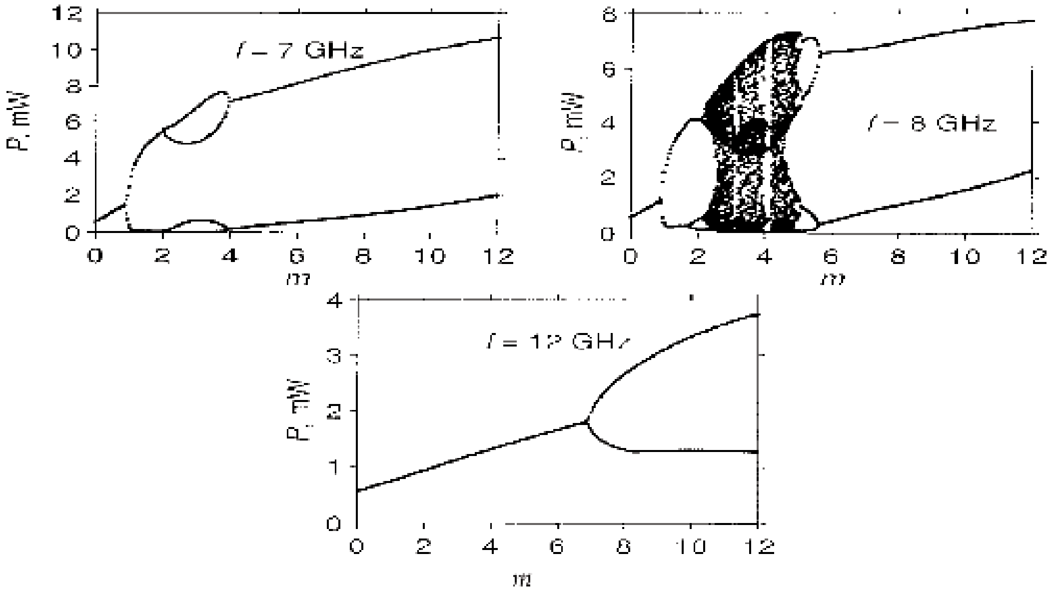

Figure 13. Bifurcation diagrams of the laser for different modulation frequencies.

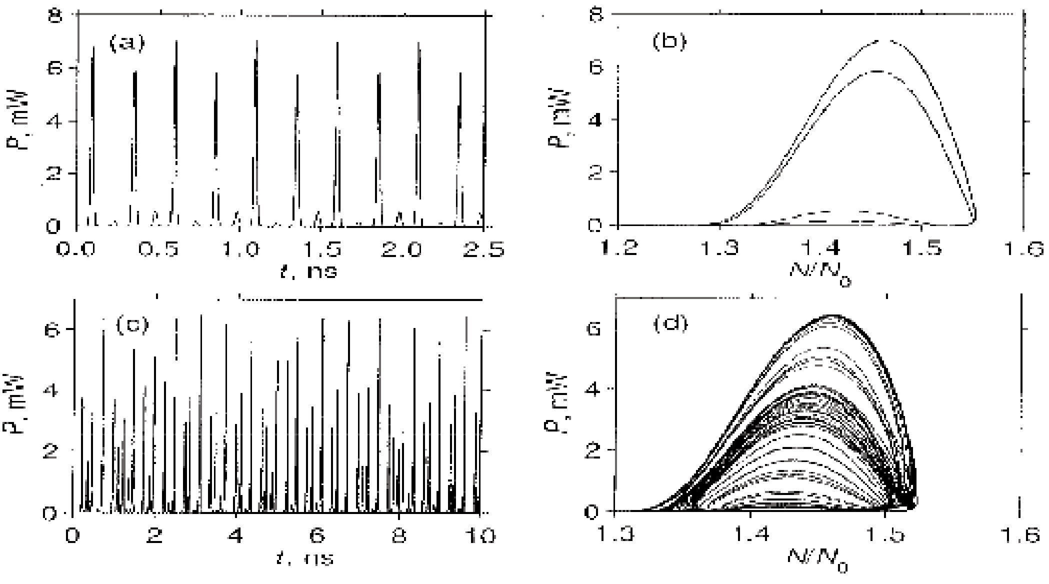

Figure 14. Nonlinear dynamics, temporal and in the phase space: (a, b) 4 T for m = 3.5 and (c, d) chaotic for m = 5.5.

4. Particularities of modeling and simulation of quantum well solar cells

This part of the chapter is dedicated to research results concerning the simulation of optical parameters (refraction index, reflectance, and the absorption coefficient) of the quantum well

(QW) photovoltaic cells, which represents the third generation of solar cells, proposed in 1990 by Keith Barnham [29, 30], aiming to extend the spectral response and to increase the photocurrent of this kind of optoelectronics devices.

The quantum well solar cell is a p-i-n structure having quantum wells built in the intrinsic region. The doped parts on each side will produce an electric field perpendicular to the layers of quantum wells as is shown in [31]. The multiple quantum well solar cells (MQW) modeling is conducted at two levels dimensionally: a *quantum level* in which one computes the energy spectrum of the electron and the absorption coefficient of the MQW; a *macroscopic level* in which one studies the transport of charge carriers in a similar manner to the conventional p-i-n diode as in [30]. The reflection of light is brought, considering MQW cell a pseudo-homogeneous medium. This combination of quantum and classical elements used in the modeling of MQW solar cell justifies the name of *hybrid* given to the model of MQW solar cell. An example of the application of the hybrid model (HM) is given in [31]. It is the case of solar cell based on a ternary alloy semiconductor $A_xB_{1-X}C$ ($Al_xGa_{1-x}As/GaAs$) which has the lowest BC band gap = 0 and achieves the greatest value (x = 1) for the AC semiconductor band gap.

The hybrid model (HM) allows determining the configuration that leads to maximum conversion efficiency. This configuration can be designed, by using the transfer matrix method and the properties of the real materials. In other words, starting from a hypothetic system structure, the HM model allows optimization of the solar cell configuration in order to obtain maximum output electrical power, for a certain state of illumination as in [32].

4.1. Modeling and simulation of the cell reflectance

An important problem is to evaluate the effect of the quantum well number on the index of refraction and on the reflection losses, so the optimal number of the quantum well for the structure can be calculated [9].

In **Figure 15**, the results of the optical simulation of reflectance R dependence on the radiation wavelength for different thicknesses d of the anti-reflecting coating (ARC) are presented, in the case of anti-reflecting coating of SiO (n_1 = 1.4). Results obtained based on presented model are consistent with experimental data.

The simulation of refraction index and reflectance of the solar cells with quantum wells have been made with the Octave software, version 3.02. The cell reflectance can be calculated using the refraction indices of GaAs semiconductor and of the $Al_{0.3}Ga_{0.7}As$ alloy as in [30]:

$$n_{GaAs} = \begin{cases} \dfrac{3.24123 - \dfrac{4.8304085}{\lambda} + \dfrac{2.82482}{\lambda^2} - \dfrac{0.769037}{\lambda^3} + \dfrac{0.08198}{\lambda^4}}{1 - \dfrac{1.5308}{\lambda} + \dfrac{0.9123972}{\lambda^2} - \dfrac{0.2508648}{\lambda^3} + \dfrac{0.026769}{\lambda^4}} \, if 0.325 < \lambda \le 4 \\ \dfrac{2.8434068 - \dfrac{1.8916996}{\lambda} + \dfrac{0.4189801}{\lambda^2} - \dfrac{0.0308637}{\lambda^3}}{1 - \dfrac{0.682372}{\lambda} + \dfrac{0.154593}{\lambda^2} - \dfrac{0.01159}{\lambda^3}} \, if 0.2 \le \lambda \le 0.325 \end{cases} \qquad (33)$$

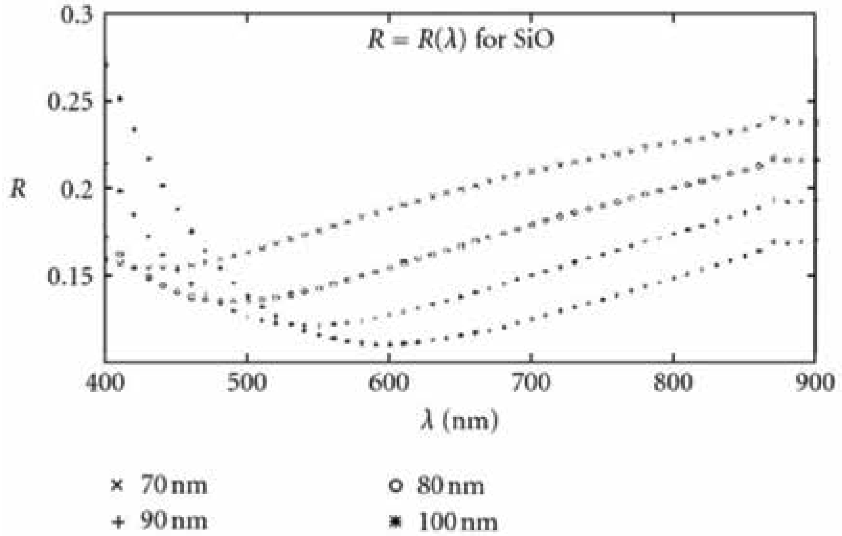

Figure 15. Simulation of the reflectance dependence of λ, for a solar cell QW structure with an SiO anti-reflecting coating.

In Eq. (33), λ is expressed in μm. The refraction index of ternary alloy $Al_xGa_{1-x}As$ is calculated as.

$$n_{Al_xGa_{1-x}As}(\lambda) = \left[1.05 - 0.53x + 0.09x^2\right] n_{GaAs}(\lambda_x) \tag{34}$$

with λ in μm

To minimize the reflection losses, the solar cells are frequently designed with anti-reflecting coating (ARC).

The MQW layer was considered to consist of 30 quantum wells of GaAs of 20-nm width separated by barriers $Al_{0.3}Ga_{0.7}As$ with a width of 10 nm.

4.2. Modeling and simulation of absorption coefficient

In applications related to calculating the conversion efficiency of solar cells, but also in other situations, the coefficient of absorption (the absorbance) is practically described by continuous functions. For GaAs, according to the experimental data shown in [30], the following function that approximates the acceptable rate of absorption was determined:

$$\alpha_{GaAs}(\lambda) = \begin{cases} e^{F_1(\lambda)}, 0.7 < \lambda \leq 0.88 \\ e^{F_2(\lambda)}, 0.24 < \lambda \leq 0.7 \\ e^{F_2(0.24)}, 0 < \lambda \leq 0.24 \\ 0, otherwise \end{cases} \tag{35}$$

$$F_1(\lambda) = -0.7863 + 5.3115\left[1 + erf\left(-\frac{\lambda - 0.84291}{0.038}\right)\right] \tag{36}$$

$$F_2(\lambda) = -447.432 + 4201.2\lambda^2 + 6835.128\lambda^2 \ln\lambda - 3781.193\lambda^3 + \frac{3.9049}{\lambda^2} \tag{37}$$

In Ref. [30], the absorption coefficient for GaAs calculated with this model is represented.

4.3. Simulation of the quantum efficiency of QW solar cells

The analyzed model uses the transport equation of $Al_xGa_{1\text{-}x}As$ quantum well solar cells, where x represents the aluminum concentration. The expression of the quantum efficiency *(QE)* is given by

$$QE \cong \frac{\alpha k(\alpha - S)}{\left(k^2 - \alpha^2\right)\left(S\sinh(kz) - k\cosh(kz)\right)} \cong \frac{\alpha - S}{\alpha^2(S-1)} \tag{38}$$

where α is the spectral absorption, ε_f is the effective electric field due to the minoritary carriers, and S a parameter.

From the analysis of the data obtained, it results that quantum efficiency increases with any increase in λ, reaching significant values of a maximum of 90%, in the case of large diffusion wavelength; quantum efficiency increases with any increase of z and ε_f, respectively.

In [30] for the cell parameters $N_w = 30$, $l_w = 20$ nm and $l_b = 10$ nm, the calculation results of the conversion efficiency are summarized.

In **Figure 16**, it is observed that the conversion efficiency is strongly correlated with the number of quantum well up to $Nw = 30$; above this value, the efficiency is saturated at larger

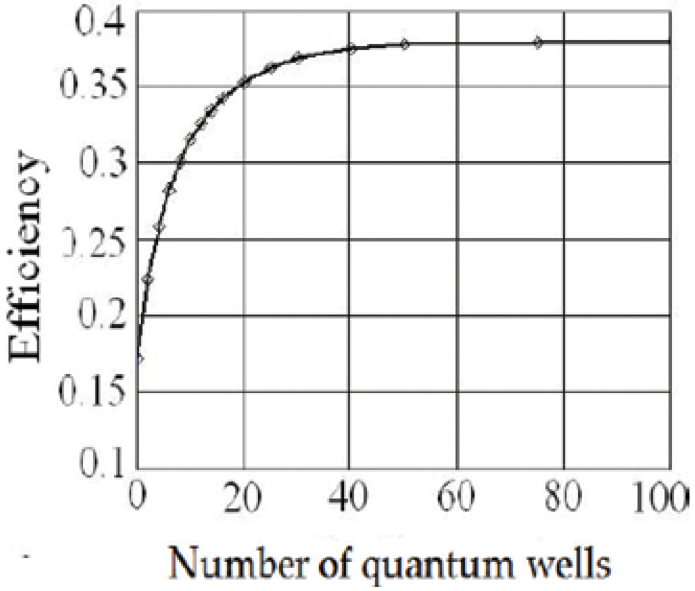

Figure 16. The dependence of the efficiency of MQW solar cell by the number of quantum wells.

values of *Nw*. The saturation is installed when the road length traveled by light is comparable with the absorption length. This result is a positive one by using the HM model. The calculation can be repeated varying different geometrical and material parameters in order to determine the optimal configuration, that is, one that maximizes efficiency.

Recently, good experimental results were reported in MQW solar cells. The fabricated solar cells based on $In_{0.3}Ga_{0.7}N$/GaN MQWs exhibit an open circuit voltage of about 2 V, a fill factor of about 60%, and an external efficiency of 40% at 420 nm and 10% at 50 nm. New solar devices could be conceived based on optical properties of nanostructured materials [29, 30].

5. Optical transmission system with laser chaotic carrier

5.1. The Pecora-Carroll synchronization method

The method presented in this chapter focuses on the transmission of information by masking it in a chaotic signal, the amplitude of the message being added to that of the carrier. Two chaotic systems can be synchronized if they have similar parameters as is shown in Ref.s [35, 36]. This phenomenon has a very good potential application in coding the transmission of information. The transmission is made by using an emergent wave from a laser as a chaotic transmitter. The signal is attached to a carrier wave which is of a chaotic nature and has much higher amplitude. This ensures a higher degree of difficulty in intercepting and decoding. For attaching the signal to the carrier chaotic masking, modulation can be used. The properties of transmission and reception of the data as well as the synchronization of the lasers can be studied by using a pair of master–slave lasers. Modeling of the lasers is made by the use of the rate equations as in [35].

A communication scheme compatible with the Pecora-Carroll synchronization method given in [36, 40] is presented in **Figure 17**. The link between the master system and the slave subsystems in the transmission area is unidirectional. The encryption is done by using the chaotic signal of the slave system at the transmitter as carrier for the message. At the receiver, the slave system synchronizes with its replica at the transmitter through the one linking drive signal. This allows the extraction of the information from the total transmitted signal.

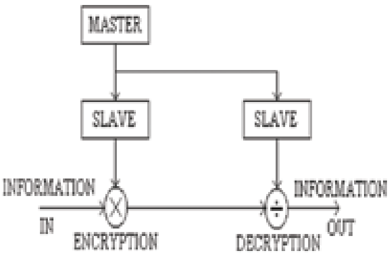

Figure 17. Block scheme of a communication system based on the synchronization of two chaotic subsystems.

5.2. Optical communications channel with chaotic laser carrier

It was shown that an amplitude modulator-demodulator with chaotic carrier can be implemented using a pair of self-pulsating laser diode (SPLDs), with closely matched parameters. If a sinusoidal injection current is superimposed over a polarization current for which self-pulsations occur, then the pulses become chaotic both in amplitude and in repetition interval. When the sinusoidal current is modulated with an information signal having amplitude and frequency much smaller than the disorder maker current, then the transmitted signal spectrum does not present a clear component having the frequency of the message, and the filtering operation is of no use in recovering the transmitted information. If a small part of the transmitted chaotic signal (SPLD-T) is coupled into the received signal (SPLD-R), the information can be recovered based on the property that the receiver output field synchronizes only with the chaotic carrier and not with the whole transmitted optical field. An SPLD is an active optical device able to produce a continuous train of pulses with repetition rate dependent on the injection current (**Figure 18**).

The self-pulsating laser diode (SPLD) is driven by an injection current $I^{T,R}(t)$:

$$I^{R,T} = I^{R,T}_{\text{bias}} + I^{R,T}_{\text{A}} \sin(2\pi f t) \tag{39}$$

where I_{bias} is the continuous component of the injection current, while I_{A} and f are the amplitude and frequency of a sinusoidal current superimposed over the continuous injection bias component, respectively. The laser parameters for numerical simulations can be found in [10]. It is noted that δ is the coupling factor of the transmitted field into the receiver SPLD.

If a sinusoidal current is superimposed over I_{bias}, then the self-pulsations became chaotic either in repetition interval or in amplitude (**Figure 19**). The two identical SPLD-R and SPLD-T have similar outputs but uncorrelated [35].

When a small part of the transmitted chaotic carrier is coupled into the receiver device, synchronization between the two lasers becomes possible (**Figures 20** and **21**), independently of the initial conditions of the two systems.

To investigate the possibility of transmission information, we introduce the information as an amplitude modulation of the sinusoidal injection current into the transmitter laser. For simplicity,

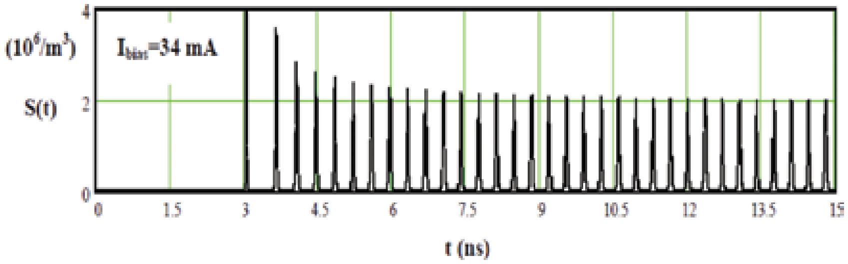

Figure 18. Temporal dynamics of SPLD for the injection current I_{bias} = 34 mA.

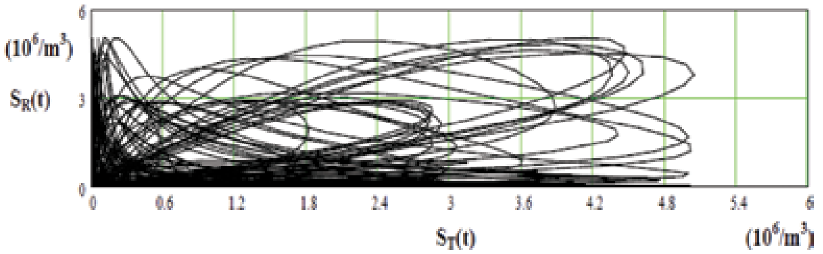

Figure 19. The output $S_R(t)$ of SPLD-R versus $S_T(t)$ SPLD-T. The two photon densities are not synchronized.

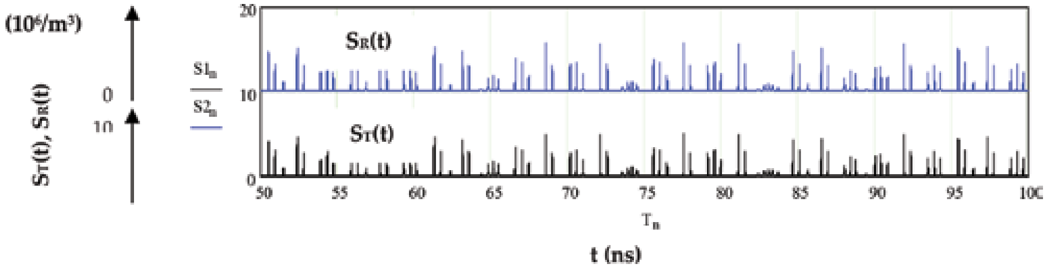

Figure 20. The graphical representation of the photon densities $S_R(t)$ and $S_T(t)$, synchronized, for $\delta = 0.04$.

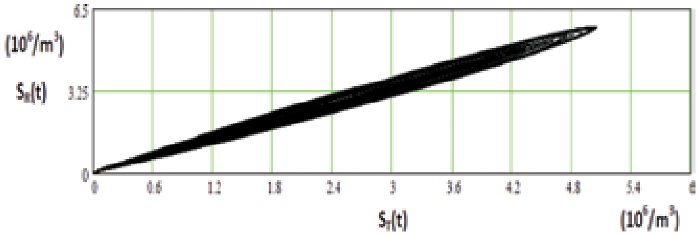

Figure 21. The output $S_R(t)$ of SPLD-R versus $S_T(t)$ SPLD-T. The two photon densities are closely synchronized.

we consider a sinusoidal message signal $I_m(t) = I_{m,A}\sin(2\pi f_m t)$, where $I_{m,A} << I_{bias}$ and $f_m << f$ for secrecy and small modulation distortion reasons. Numerical simulations show that the receiver output synchronizes with the carrier field, rather than to the transmitted signal; the decoded signal is obtained as $S_d(t) = S_T(t) - S_R(t)$ In **Figure 22**, a typical method of recovering information in such a kind of transmission is presented.

The useful message can be recovered by low filtering of the quantity $[S_T(t) - S_R(t)]/S_R(t)$. As SPLDs are widely available, cheap, and compact, their use in private communication systems, but not only, for transmissions with information encrypted is recommended.

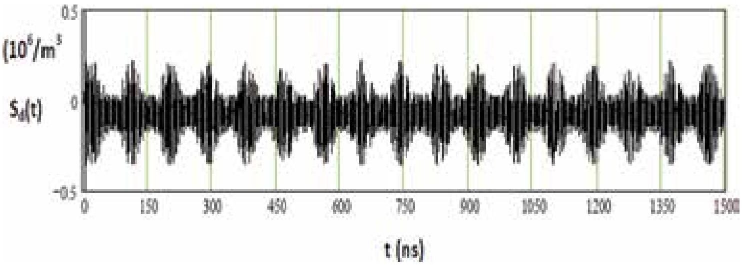

Figure 22. The decoded signal versus time. $S_d(t) = \frac{S_T(t)-S_R(t)}{S_R(t)}$ for $I_{\mathrm{m}}(t) = (7/50)\sin[2\pi(f/50)t]$ mA.

6. Conclusions

The mathematical models presented in this chapter highlight the possibility of unitary, describing the nonlinear dynamics in the optoelectronics structures with quantum well fact which is essential for their design and applications.

The obtained results by numerical simulations show how the dynamics is characterized by bifurcation points and chaos, being close to those obtained experimentally and reported in the literature.

The results based on the hybrid model of the MQW solar cells show that the number of quantum well of the structure can be determined by numerical simulations for improving the conversion efficiency, based on optical properties of nanostructured materials used in research and fabrication.

The broadband modulation and the low injection current at the oscillation threshold of the quantum well lasers compared to bulk laser ones recommends these optoelectronics structures for high-speed optical communications, providing unwanted nonlinear effects as the points of bifurcation and chaos are avoided, for the stable operation and the control of their dynamics.

Conflict of interest

The authors declare that there is no conflict of interest regarding the publication of this chapter.

Author details

Andreea Rodica Sterian

Address all correspondence to: andreea.sterian1@yahoo.com

Faculty of Applied Sciences, Physics Department, Academic Center of Optical Engineering
and Photonics, Polytechnic University of Bucharest, Bucharest, Romania

References

[1] Weiss U. Quantum Dissipative Systems. Toh Tuck Kink, Singapore: World Scientific Publishing Co. Pte.Ltd.; 2012

[2] Sterian PE. Analytical model of dissipative coupling coefficients in laser structures. Proceedings of the Romanian Academy A. 2002;**3**(3):123-126

[3] Peter SZ, Zory J. Quantum Well Lasers. Vol. 347. Boston: Academic Press; 1993

[4] Sterian P. Exact quantum master equations for Markoffian systems. Optical Engineering. 1996 Jun 1;**35**(6):1573-1575. DOI: 10.1117/1.601001

[5] Sterian PE. Fotonica. Printech; 2000

[6] Stefanescu E, Sterian AR, Sterian P. Study on the fermion systems coupled by electric dipol interaction with the free electromagnetic field. In: 21st European Mask and Lithography Conference 2005 Jun 7 (pp. 160–165). International Society for Optics and Photonics. DOI: 10.1117/12.63368

[7] Sterian AR. Coherent radiation generation and amplification in erbium doped systems. In: Advances in Optical Amplifiers. Croatia: InTech; 2011

[8] Iordache DA, Sterian P, Sterian AR, Pop F. Complex computer simulations, numerical artifacts, and numerical phenomena. International Journal of Computers Communications & Control. 2010 Dec 1;**5**(5):744-754. DOI: 10.15837/ijccc.2010.5.2234

[9] Barnham KW, Duggan G. A new approach to high-efficiency multi-band-gap solar cells. Journal of Applied Physics. 1990 Apr 1;**67**(7):3490-3493. DOI: 10.1063/1.345339

[10] Sterian AR. Amplificatoare optice. Editura Printech; 2006. DOI: 10.1109/3.748833

[11] Ghoniemy S, MacEachern L, Mahmoud S. Extended robust semiconductor laser modeling for analog optical link simulations. IEEE Journal of Selected Topics in Quantum Electronics. 2003 May;**9**(3):872-878. DOI: 10.1109/JSTQE.2003.818841

[12] Sterian AR. Numerical simulations on nonlinear dynamics in lasers as related high energy physics phenomena. Advances in High Energy Physics. 2013 Oct 27;**2013**. DOI: 10.1155/2013/516396

[13] Sterian AR. The structure of an automatic decision system for a large number of independent particle detectors. Advances in High Energy Physics. 2013 Mar 10;2013. DOI: 10.11 55/2013/839570

[14] Anghel DA, Sterian AR, Sterian PE. Modeling quantum well lasers. Mathematical Problems in Engineering. 2012 Mar 7;**2012**. DOI: 10.1155/2012/736529

[15] Tsou BP, Pulfrey DL. A versatile SPICE model for quantum-well lasers. IEEE Journal of Quantum Electronics. 1997 Feb;**33**(2):246-254. DOI: 10.1109/3.552265

[16] Dehghan M, Derakhshan P. A novel dynamic analysis and simulation for quantum-well distributed feedback laser,(qw-dfb). Progress in Electromagnetics Research B. 2008;**3**:105-114

[17] Popescu IM, Preda AM, Tudorache SS. Aplicatii ale laserilor. Bucuresti: Tehnica; 1979

[18] Gao DS, Kang SM, Bryan RP, Coleman JJ. Modeling of quantum-well lasers for computer-aided analysis of optoelectronic integrated circuits. IEEE Journal of Quantum Electronics. 1990 Jul;**26**(7):1206-1216. DOI: 10.1109/3.59660

[19] Javro SA, Kang SM. Transforming Tucker's linearization laser rate equations to a form that has a single solution regime. Journal of Lightwave Technology. 1995 Sep;**13**(9):1899-1904. DOI: 10.1109/50.464741

[20] Mena PV, Kang SM, DeTemple TA. Rate-equation-based laser models with a single solution regime. Journal of lightwave Technology. 1997 Apr;**15**(4):717-730. DOI: 10.1109/50.566695

[21] Sterian AR. Computer modeling of the coherent optical amplifier and laser systems. In: International Conference on Computational Science and Its Applications 2007 Aug 26. Springer, Berlin, Heidelberg. pp. 436-449

[22] Bulinski M, Pascu ML. Chaos in laser diode light emission. Romanian Journal of Optoelectronics. 2001 Apr;**9**(2):1-34

[23] Lee CH, Yoon TH, Shin SY. Period doubling and chaos in a directly modulated laser diode. Applied Physics Letters. 1985 Jan 1;**46**(1):95-97. DOI: 10.1063/1.95810

[24] Bennett S, Snowden CM, Iezekiel S. Nonlinear dynamics in directly modulated multiple-quantum-well laser diodes. IEEE Journal of Quantum Electronics. 1997 Nov;**33**(11):2076-2083. DOI: 10.1109/3.641323

[25] Ninulescu V, Nicolae VB, Sterian *A*. Quantum well lasers for medical industry. InBIRD. 2008. pp. 563-570

[26] Nagarajan R, Ishikawa M, Fukushima T, Geels RS, Bowers JE. High speed quantum-well lasers and carrier transport effects. IEEE Journal of Quantum Electronics. 1992 Oct;**28**(10): 1990-2008. DOI: 10.1109/3.159508

[27] Marcuse DI. Computer simulation of laser photon fluctuations: Theory of single-cavity laser. IEEE Journal of Quantum Electronics. 1984 Oct;**20**(10):1139-1148. DOI: 10.1109/JQE.1984.1072276

[28] Sterian AR, Ninulescu V, Sterian L. Modulated laser diode for medical applications. In: Proc. of SPIE Vol 2004 Oct 21 Vol. 5581. p. 275. DOI: 10.1117/12.582837

[29] Barnham KW, Barnes JM, Braun B, Connolly JP, Haarpaintner G, Nelson JA, Paxman M, Button C, Roberts JS, Foxon CT. A novel approach to higher efficiency-the quantum well solar cell. In: Proceedings of the 11th EC Photovoltaic Solar Energy Conference 1992 pp. 146-149

[30] Fara L, editor. Advanced Solar Cell Materials, Technology, Modeling, and Simulation. IGI Global; 2012 Jul 31

[31] Fara S, Sterian P, Fara L, Iancu M, Sterian A. New results in optical modelling of quantum well solar cells. International Journal of Photoenergy. 2012 May 16:2012. DOI: 10.1155/2012/810801

[32] Fara L, Moraru AG, Sterian P, Bobei AP, Diaconu A, Fara S. Building integrated photovoltaic (BIPV) systems in Romania. Monitoring, modelling and experimental validation. Journal of Optoelectronics and Advanced Materials. 2013 Jan 1;**15**(1–2):125-130

[33] Iordache DA, Sterian PE, Tunaru I. Charge coupled devices as particle detectors. Advances in High Energy Physics. 2013 Mar;**19**:2013. DOI: 10.1155/2012/810801

[34] Popescu DG, Sterian P. Photonic crystal fiber mode characterization with multipole method. UPB Scientific Bulletin, A Series. Bucharest: University "Politehnica" of Bucharest; 2013 Jan 1;**75**:205-215

[35] Sterian P, Ninulescu V, Sterian AR, Lazar B. Optical communication methods based on chaotic laser signals. University Politehnica of Bucharest scientific bulletin-series A-applied mathematics and. Physics. 2010 Jan 1;**72**(1):83-94

[36] Pecora LM, Carroll TL. Driving systems with chaotic signals. Physical Review A. 1991 Aug 1;**44**(4):2374. DOI: 10.1103/PhysRevA.44.2374

[37] Sterian PE. Transmisia optica a informatiei. Bucharest: Editura Tehnică; 1981

[38] FAZACAŞ A, Sterian P. Propagation of the Raman soliton in optical fibers. Romanian Reports in Physics. 2013;**65**(4):1420-1430

[39] Sanchez-Diaz A, Mirasso CR, Colet P, Garcia-Fernandez P. Encoded Gbit/s digital communications with synchronized chaotic semiconductor lasers. IEEE journal of quantum electronics. 1999 Mar;**35**(3):292-297

[40] Sterian PE. Communication based on chaotic signals. Proceedings of the Romanian Academy. 2002;**3**(1–2):45-48

Section 2

Sensors

Infrared Sensors for Autonomous Vehicles

Rajeev Thakur

Additional information is available at the end of the chapter

http://dx.doi.org/10.5772/intechopen.70577

Abstract

The spurt in interest and development of Autonomous vehicles is a continuing boost to the growth of electronic devices in the automotive industry. The sensing, processing, activation, feedback and control functions done by the human brain have to be replaced with electronics. The task is proving to be exhilarating and daunting at the same time. The environment sensors – RADAR (RAdio Detection And Ranging), Camera and LIDAR (Light Detection And Ranging) are enjoying a lot attention with the need for increasingly greater range and resolution being demanded by the "eyes" and faster computation by the "brain". Even though all three and more sensors (Ultrasonic / Stereo Camera / GPS / etc.) will be used together; this chapter will focus on challenges facing Camera and LIDAR. Anywhere from 2 – 8 cameras and 1 – 2 LIDAR are expected to be part of the sensor suite needed by Autonomous vehicles – which have to function equally well in day and night. Near infrared (800 – 1000nm) devices are currently emitters of choice in these sensors. Higher range, resolution and Field of view pose many challenges to overcome with new electronic device innovations before we realize the safety and other benefits of autonomous vehicles.

Keywords: autonomous vehicles, infrared, sensors, LIDAR, camera

1. Introduction

The Federal Automated Vehicles Policy [2] document released by NHTSA in September 2016 states that 35,092 people died on US roadways in 2015 and 94% of the crashes were attributed to human error. Highly automated vehicles (HAVs) have the potential to mitigate most of these crashes. They also have such advantages as not being emotional, not fatiguing like humans, learning from past mistakes of their own and other HAVs, being able to use complementary technologies like Vehicle-to-Vehicle (V2V) and Vehicle-to-Infrastructure (V2I) – which could further enhance system performance. Add in the potential to save energy

Level	**Name**	**Narrative definition**	**Dynamic Driving Task (DDT)**		**DDT fallback**	**Operational Design Domain (ODD)**
			Sustained lateral and longitudinal vehicle motion control	**Object and Event Detection and Response (OEDR)**		
Driver performs part or all of the Dynamic Driving Task (DDT)						
0	**No Driving Automation**	The performance by the *driver* of the entire *DDT*, even when enhanced by *active safety systems*.	*Driver*	*Driver*	*Driver*	n/a
1	**Driver Assistance**	The *sustained* and *ODD*-specific execution by a *driving automation system* of either the *lateral* or the *longitudinal vehicle motion control* subtask of the DDT (but not both simultaneously) with the expectation that the *driver* performs the remainder of the *DDT*.	*Driver* and *System*	*Driver*	*Driver*	Limited
2	**Partial Driving Automation**	The *sustained* and *ODD*-specific execution by a *driving automation system* of both the *lateral* and *longitudinal vehicle motion control* subtasks of the *DDT* with the expectation that the *driver* completes the *OEDR* subtask and *supervises* the *driving automation system*.	***System***	*Driver*	*Driver*	Limited
***Automated Driving System* (“*System*”) performs the entire *DDT* (while engaged)**						
3	**Conditional Driving Automation**	The *sustained* and *ODD*-specific performance by an *ADS* of the entire DDT with the expectation that the *DDT fallback-ready user* is *receptive* to *ADS*-issued *requests to intervene*, as well as to *DDT performance-relevant system failures* in other *vehicle* systems, and will respond appropriately.	*System*	*System*	*Fallback ready user (Driver is fallback)*	Limited
4	**High Driving Automation**	The *sustained* and *ODD*-specific performance by an *ADS* of the entire *DDT* and *DDT fallback* without any expectation that a *user* will respond to a *request to intervene*.	*System*	*System*	*System*	**Limited**
5	**Full Driving Automation**	The *sustained* and unconditional (i.e., not *ODD*-specific) performance by an *ADS* of the entire *DDT* and *DDT fallback* without any expectation that a *user* will respond to a *request to intervene*.	*System*	*System*	*System*	**Unlimited**

Table 1. SAE J3016 – summary of levels of driving automation [3].

and reduce pollution (better fuel economy, ride sharing and electrification) – creating a huge impetus to implement autonomous vehicle technology as soon as possible.

On the other hand we have the consumer industry from Silicon Valley eyeing autonomous vehicles as a huge platform to engage, interact, customize and monetize the user experience. Think online shopping, watching a movie, doing your email or office work, video chats, customized advertisements based on user profile and location, etc. – all while our transport takes us to our destination. The innovation and business potential presented by the HAVs is only limited by imagination and savvy to overcome the challenges.

Among the various challenges to overcome are those of sensing the environment around and even inside the vehicle. Two of these sensing technologies are LIDAR and camera. Each of them are evolving fast to meet the industry demands. Levels 3–5 of autonomous vehicles as defined by NHTSA and SAE (**Table 1**) will need a high resolution and long range scanning LIDAR [3]. They will also need cameras which operate in infrared (and visible) spectrum to be able to function at night and low light conditions.

We will start with discussing the infrared spectrum, its advantages and disadvantages and then move onto LIDAR and Camera in some level of detail.

2. Infrared spectrum

2.1. Infrared radiation

The sun radiates electromagnetic energy in a wide spectrum from the shortest X-rays to radio waves. **Figure 1** shows the portion visible to the human eye (~380–750 nm) and the infrared region [4]. The near infrared region (~750–1400 nm) is used in many sensing applications

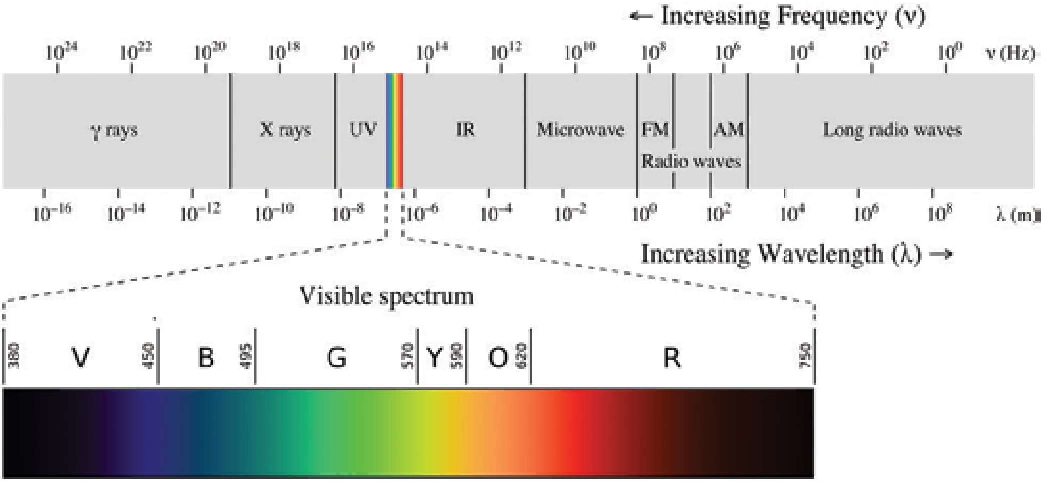

Figure 1. Electromagnetic spectrum with visible light highlighted [4].

including the night vision camera and LIDAR. The active night vision cameras (use light from artificial sources) are different from the passive thermal imaging cameras which operate at higher wavelengths (8–15 μm) and use natural heat as sources of radiation. **Figure 1** also shows the wide range of infrared radiation from 750 nm to 1 mm wavelength.

2.2. Sensitivity

Figure 2 shows the human eye and camera sensitivity to the visible – Near infrared (NIR) spectrum. The advantage and disadvantage for sensing applications primarily arises from the fact that infrared is mostly invisible in the far field. A fair amount of red color can be seen by most humans till 850 nm; beyond that lies a fair amount of subjectivity. The fact that the human eye is not very sensitive to NIR light allows cameras to be used unobtrusively (especially at night/poor lighting conditions). The disadvantage lies in the fact that silicon based image sensors have poor sensitivity in this wavelength (~35% QE at 850 and 10% at 940 nm). In addition these wavelengths can reach the retina of the eye – so the exposure has to be controlled to avoid damage.

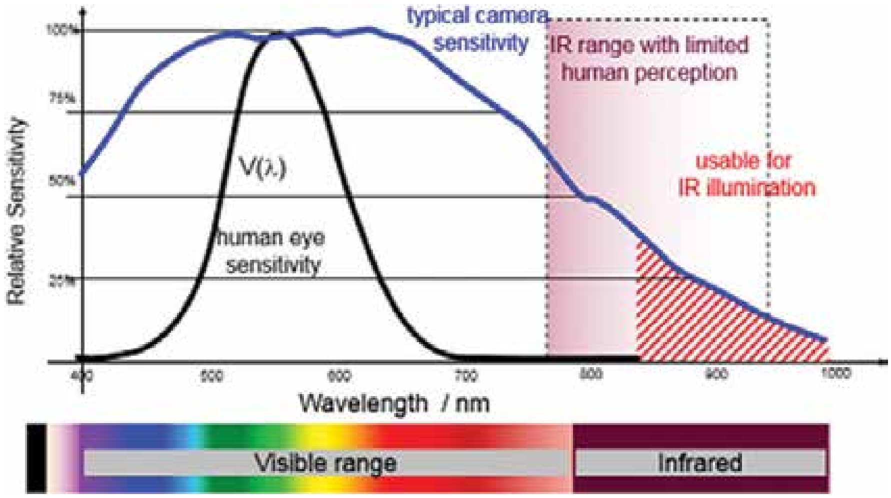

Figure 2. Sensitivity of photo detectors and cameras vs. human eye.

2.3. Spectral irradiance

The solar radiation outside the earth's atmosphere and that reaching the surface is shown in **Figure 3** [8].

Dips in the spectral irradiance at surface are primarily due to water in the atmosphere. In the infrared spectrum of interest they occur at 810, 935, 1130, 1380, 1880 nm and beyond. This means the ambient noise is lower at these specific wavelengths. However, wavelengths of many semiconductor devices shift with temperature (~0.3 nm/°C for Gallium arsenide and aluminum gallium

http://dx.doi.org/10.5772/intechopen.70577

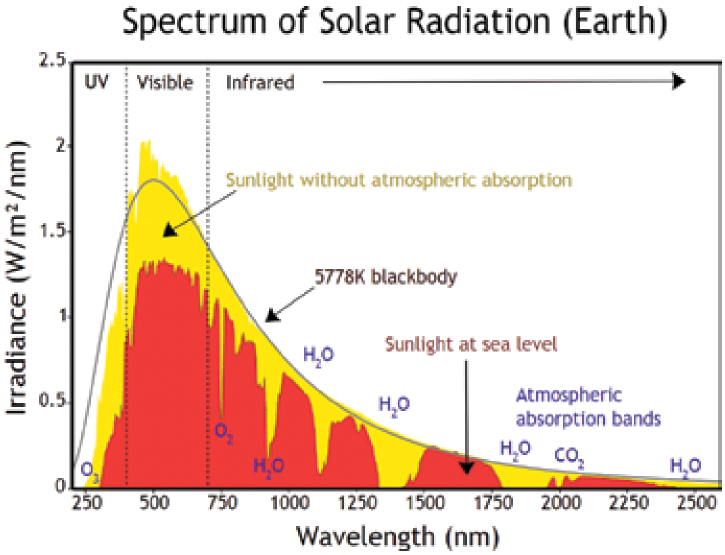

Figure 3. Solar spectral irradiance on earth [8].

arsenide materials used in infrared spectrum); for automotive applications this shift is ~44 nm from −40 to 105°C. Ideally we need a peak with flat ambient noise variation around it for good design.

Another observation from **Figure 3** is the lower ambient noise as we go to the longer wavelengths. However, past ~1000 nm the material base for detectors changes from silicon to germanium or indium gallium arsenide – which can be expensive.

3. Light Detection And Ranging (LIDAR)

3.1. Need for LIDAR in automotive

LIDAR, RAdio Detection And Ranging (RADAR) and Camera are the environment sensors central to the autonomous car operation. They are used to detect and classify the objects around the car by location and velocity. Each of the sensors has limitations and the information obtained from them is fused together with confidence prior to making a decision on the vehicles trajectory.

Table 2 provides a brief summary of the above sensing technologies.

3.2. Types

LIDAR sensors could be classified on any of its various key parameters:

- Operating principle: Time of Flight (ToF)/Frequency Modulated Continuous Wave (FMCW)

- Scanning technology: Mechanical/Micro-Mechanical-Mirror (MEMS)/Optical Phase Array (OPA)
- Scanning/Flash
- Solid State/Mechanical
- Wavelength: 905 /1550 nm
- Detection technology: Photodiode/Avalanche Photodiode/Single Photon Multiplier
- …and many other ways

Sensor	Typical range	Horizontal FOV	Vertical FOV	2020 price range	Comments
24 GHz RADAR	60 m [6]	56° [6]	~±20°	<$100	USA Bandwidth Max 250 MHz [7] Robust to snow/rain Poor angular resolution; sensitive to installation tolerances and materials
77 GHz RADAR	200 m [6]	18° [6]	~±5°	<$100	Similar to 24 GHz RADAR with more bandwidth (600 MHz [7]); sensitive to installation tolerances and materials
Front Mono Camera	50 m [6]	36° [6]	~±14°	<$100	Versatile sensor with high resolution; Poor depth perception; High processing needs; low range; sensitive to dirt/obstruction
LIDAR (Flash)	75 m	140°	~±5°	<$100	Better resolution than RADAR and more range than Camera. Eye safety limits; Poor in bad weather; sensitive to dirt/obstruction
LIDAR (Scanning)	200 m	360°	~±14°	<$500	Similar to Flash LIDAR with higher resolution and Cost; sensitive to dirt/obstruction

Table 2. RADAR – camera – LIDAR comparison.

3.3. Time of Flight LIDAR Operating Principle

The Time of Flight LIDAR operation can be explained using **Figure 4**.

A laser is used to illuminate or "FLASH" the field of view to be sensed. The laser pulse travels till it is reflected off a target and returned to a detector. The time taken for the pulse to travel back and forth provides the range. The location of the target is based off optics mapped over the field of view and detector array. Two or more pulses from the target provide the velocity. The angular resolution depends on the number of detector pixels which map the field of view. The more pixels we have – the better the resolution.

The same principle is used by 3D cameras or high resolution flash LIDAR. Higher power and more detector pixels are used.

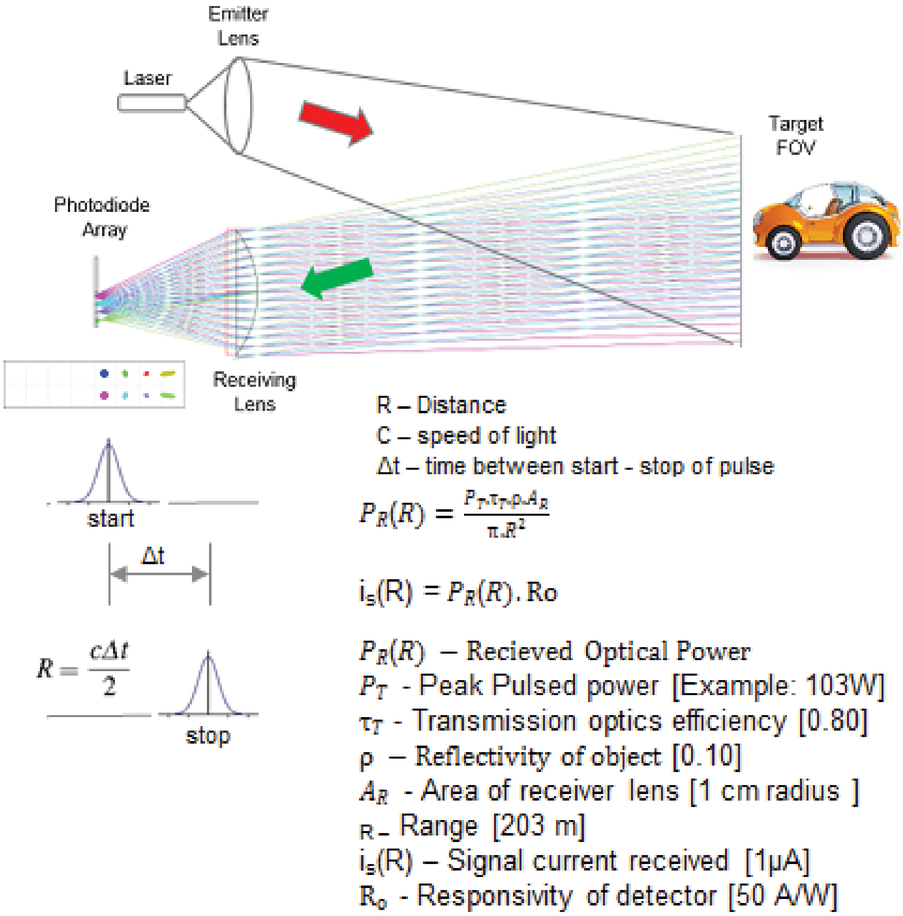

Figure 4. Time-of-Flight FLASH LIDAR.

3.4. Emitter and detector options

As shown in **Figure 4**, to increase the range by 2× – the needed power is 4×. As we increase the power – we start running into eye safety limits. Infrared light below 1400 nm can reach the retina of the eye. If the exposure limit is exceeded, permanent eye damage can occur.

There are many levers available to achieve the needed range – including better detectors, bigger lenses, and shorter pulse widths. Of course, the best option would be to use light above the 1400 nm wavelength. However, to use lasers and detectors in this wavelength region (>1400 nm) – we typically have to use more expensive materials (indium-gallium-arsenide—phosphide lasers and germanium-based detectors).

3.5. Eye safety

Sunlight on the earth's surface is composed of ~52% infrared (>700 nm), ~43% visible (400–700 nm) and ~3% Ultraviolet (<400 nm) [9]. The intensity of infrared is low enough that it does not cause eye damage under normal exposure. When light is visible and bright, the eye has a natural blink response and we do not stare at it – helping to avoid eye damage. Infrared light is not visible and so can cause eye damage if exposure limits are not regulated.

The safe levels of infrared levels are regulated by IEC-62471 for Light Emitting Diodes and IEC-60825 (2014) for lasers. In USA, the equivalent federal standards are in 21 CFR 1040 (Code of Federal Regulations).

The standards have hazard exposure limits for the cornea of the eye, thermal hazard limit for skin and eye retinal thermal hazard exposure. For exposures above 1000 s, the irradiance limit is 100 W/m^2 at room temperature and 400 W/m^2 at 0°C. The retina exposure limits tend to be more stringent. The calculations are complex and depend on wavelength, size of the emitter, exposure time and other factors.

3.6. Signal processing challenges

As sensors demand higher resolution and faster response – it increase the computational needs. At the raw signal level, using the forward camera as an example:

Number of pixels to be processed = frames per seconds × horizontal field of view/resolution × vertical field of view/resolution.

Example: 30 fps camera, 40° HFOV, 40° VFOV, 0.1° resolution

- 30 × 400 × 400 = 4.8 Mpx/s

A similar amount of data needs to be processed by the LIDAR, RADAR and other sensors. At some level, this information has to be fused to recognize and classify objects and their trajectory.

As more and more sensing data is collected, processed and acted upon in real time (time between collection and use is extremely short), creating ways of storing/processing and updating data are being developed. For example – the 3 dimensional roadway maps needed for autonomous driving are stored in the cloud (remote server) and real time data is processed to look only for changes and updates; thus reducing the amount of data crunching to be done in real time. Another trend is to collect and process the raw analog signal when possible – thus reducing the downstream processing needs.

Security of data in autonomous vehicles is another growing concern and business opportunity for innovation. Automotive Information Sharing and Analysis Center (Auto-ISAC) (www.automotiveisac.com) was formed in 2015 by automakers to share the best practices related to cyber threats in the connected car.

4. Camera

Camera's in automobiles continue to grow as their functional versatility is exploited with increasing innovation. They have become central to Advanced Driver Assistance Systems

(ADAS) like adaptive cruise control, adaptive high beam, automatic emergency braking, lane departure warning, blind spot detection, driver monitoring, traffic sign detection and others.

The latest Tesla Model 3 is believed to have up to eight exterior cameras. Other OEM's are also using interior driver monitoring and gesture recognition cameras. A presentation from IHS Markit [13] shows typically five exterior and one interior camera for Level 3; eight exterior cameras and 1 interior camera for Level 4 being planned by a number of Original Equipment Manufacturers.

4.1. Exterior infrared camera (night vision)

Cameras need light to illuminate the objects in its field of view. Currently most cameras used in ADAS functions work with visible light – which is fine for daytime operation. However, at night the prime source for visible light is usually the headlamps of the car. The visible light from the headlamps is strictly regulated by NHTSA with its Federal Motor Vehicles Safety Standard 108 (FMVSS 108). **Figure 5** below shows a bird's eye view of the permitted illumination region in the USA.

It can be observed that in essence, visible light can only be legally used for a limited range of ~60 m in front of the vehicle. Illumination outside the car lane and around the car is very limited (if any). These legal requirements are not expected to be changed anytime soon – since we will have cars driven by humans for at least another 20–30 years. This means to illuminate to longer and wider fields of view, the cameras have to work with infrared light (which is not regulated by FMVSS 108). As long as the infrared light is within eye safe limits, it can be used all around the car.

Figure 6 shows a graphic overview of the regions around the car that are covered by cameras. The forward camera needs to ideally sense as far as the RADAR and LIDAR to permit good sensor fusion.

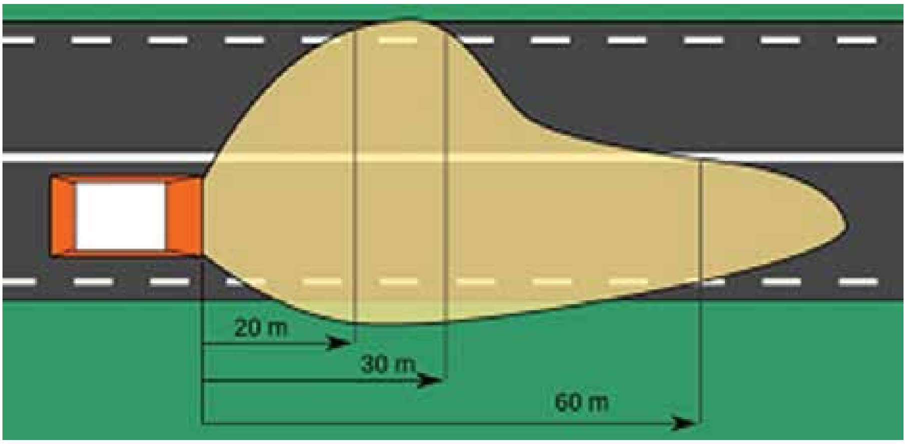

Figure 5. FMVSS 108 low beam visible light illumination.

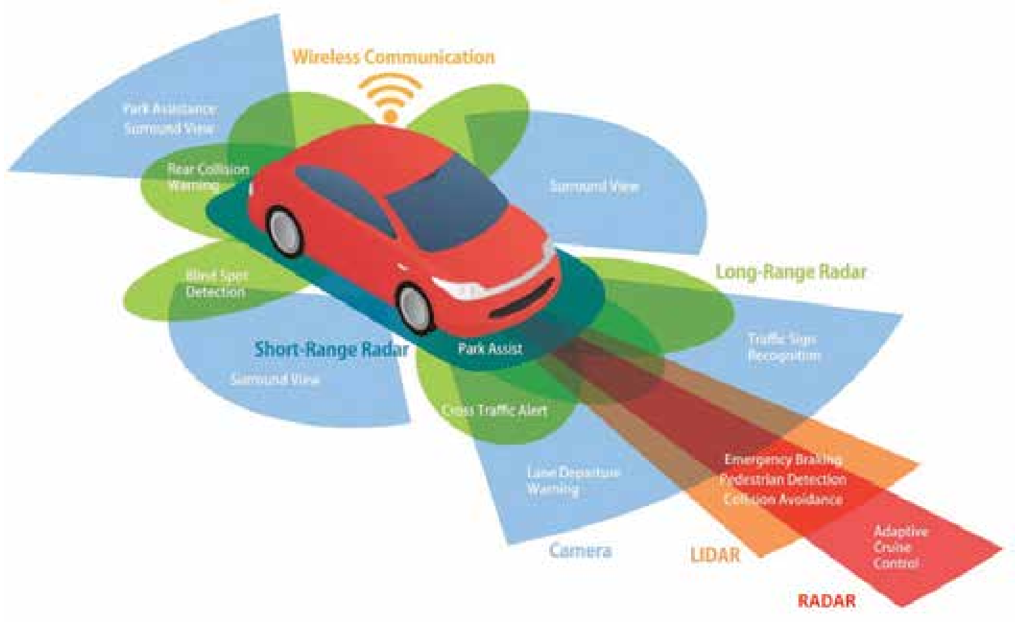

Figure 6. Environment sensors needed for autonomous cars.

The target range for RADAR and LIDAR is at least 200 m (Forward direction) and 50–100 m in all other directions.

4.2. Exterior camera illumination challenges

The spectral sensitivity of CMOS image sensors at 850 nm is ~35% compared to its peak at 550 nm (green). Further down at 940 nm, this reduces to ~10%. This means a larger number of infrared photons is needed to generate a clear image.

To illuminate targets at longer ranges and wider field of view more light is needed. In addition, different targets have different reflectivity – which can have a significant effect on the image quality. So while we put out more and more light to get a better signal – we need to ensure the intensity is still eye safe. We also start eating up more energy from the battery for illumination. Calculations show the amount of infrared flux needed could be anywhere from 6 W (100 m range, 12° FOV, 50% reflectivity, 850 nm, 0.15 $\mu W/cm^2$, Lens F#1) to 1250 W (200 m range, 40° FOV, 10% reflectivity, 850 nm, 0.15 $\mu W/cm^2$, Lens F#1) [10, 11].

A typical headlamp today may have 5 W of visible light used per lamp currently. Imagine the complexity of adding 100's of more Watts to the headlamp. The self-driving eco system has not yet come to grasp the scope of challenge that it has to deal with here. The alternative would be to rely more on the LIDAR and RADAR sensors at the longer ranges and use the camera only in the short ranges. This option may not provide needed reliability – since all of these technologies have weakness (RADAR does not same resolution as camera at long ranges and LIDAR is more prone to poor performance in bad weather).

Potential solution options which have not been fully vetted are to use pulsed infrared lasers to illuminate the CMOS based cameras; use of infrared matrix lighting architectures where rows of LED's are turned on in sequence with a rolling shutter camera more to come as we make progress.

4.3. Interior camera – market need

The need for an interior camera arises out of multiple market forces. The first is the introduction of self-driving cars which are autonomous only in certain driving conditions (highways/traffic Jams). The cars switch between the human driver and the computer as needed. To do this effectively, the human driver has to be monitored as part of the environment in and around the car. This is to ensure adequate warning is given to the driver to leave their current engagement and get ready to take over the task of driving.

The second market force is the increase of distracted driving. In 2014, 3179 (10% of Total) people were killed and an additional 431,000 (18% of total) were injured in collisions involving distracted drivers in the USA [10]. NHTSA has a blueprint to reduce accidents related to distracted driving – which encourages OEM's to put in place measures to ensure the driver keeps their eyes on the road when the vehicle is moving. A definition of distraction in terms of driver gaze and time elapsed away from looking straight is provided in other-related NHTSA documents [12]. At a high level, looking more than 2 s in a direction 30° sideways of up-down when the vehicle speed is more than 5 mph would be classified as distracted. The increase in distracted driving is attributed to cell phone/smartphone/texting and related activities.

Additional benefits and applications are continuing to generate from the driver monitoring infrared camera system. It lends itself well to also catch drowsy drivers (eyelids shut or drowsy pupils); face recognition – not strong enough to be a biometric device, but enough to at least enable customized settings for different drivers in family and many more to come.

The auto industry is responding to these two needs (autonomous cars, distracted driving) by installing an infrared camera to monitor the gaze of the driver. Infrared illumination is needed – since we do not want to distract the driver at night with visible light. The wavelength for illumination is in the 850–950 nm range. The eye safety and camera sensitivity challenges of illumination in this spectrum were briefly discussed earlier sections. A few other challenges are discussed in the next section.

4.4. Interior camera illumination challenges

When we use an infrared camera facing the driver, the LED's are shining the light right on our eyes and face. Light at 850 nm can be red enough to be seen easily by most people – especially at night. Measures to put in a dark filter and smudge the bright red LED spot with optics are partially successful. The problem arises from the fact that anything done to reduce the brightness will usually also reduce the illumination – which would result in poor image quality and failure to detect distraction in gaze by the software processing the image.

One solution is to go to higher wavelengths (940 nm) – the challenge here is lower camera sensitivity. This has been overcome by pulsing higher peak currents at lower duty cycle using a global shutter image sensor. The typical cameras used are 30 fps and these are fast enough – since gaze while driving does not change that often and fast.

On the eye safety side, measures are needed to ensure that when the eyes are too close to the Infrared LED (IRED) – then they either need to be shutoff or reduced in intensity. Typically the distance to the eye is estimated with the camera itself, as an added measure we can have proximity sensors.

Since these cameras work in infrared with a filter block for visible wavelengths, the biggest challenge for illumination tends to be during daytime under full sunlight. The IREDs have to typically overcome ambient noise from the sun. Polaroid sunglasses can also sometimes prevent function if the coating prevents the wavelength to pass through.

The last challenge worth mentioning is that of consumer acceptance and loss of privacy. From a legal perspective, if the camera is recording the driver's face – the information can be pulled up in court if needed by a lawyer. NHTSA regulations mandate that any information needed for vehicle safety has to be stored for a short direction – essentially a black box (As used in aircrafts) to help reconstruct an accident. Will consumers trade a loss of privacy for safety and convenience (of automated driving) is yet to be seen. OEM's may initially provide consumers with the option to turn off the camera (and related loss of function) to enable the transition.

4.5. Additional applications for interior camera

OEMs are evaluating the concept of using interior cameras to monitor all occupants in the car – to enable optimum deployment of airbags and other passive safety devices. At a basic level, if there is no occupant in the passenger seat (or just a cargo box) – do not deploy the airbag.

Another application is the use of gesture recognition. The idea is use gesture's seamlessly and conveniently to open windows/sunroofs/turn on radio/change albums/etc. The successful combination of voice, touch and gesture to operate devices depend a lot on the age group (and resultant car design) and how well the technologies are implemented.

Face recognition and iris recognition are already making their way into smartphones. They are expected to penetrate the auto market. Even through the technologies are available and mature, the business case/consumer demand/willingness to pay for these functions is yet to be explored.

4.6. Signal processing

As cameras become ubiquitous around the car, the questions become how many cameras are enough and what should be the range and resolution of the cameras. The same question can be asked of LIDAR and RADAR also. However, signal processing tends to be more demanding the high resolution (comparatively) of cameras.

Assuming a VGA format for the image sensor, we get 480 (H) × 640 (W) pixels per frame; with typically 30 fps coming in for processing. The resolution we get from this VGA image sensor depends on the optical field of view it covers and the maximum range at which the smallest object has to be recognized and resolved for action. At 100 m and a 40° HFOV the width covered by the 640 pixels is ~7279 cm. This means each pixel covers 11.4 cm or ~4.5 in. Is this level of resolution good enough for self-driving cars? The next section digs a little deeper into this topic.

4.7. Exterior camera resolution requirement

What is the smallest object that can change the trajectory of the car? One could argue this could be as small as a nail or sharp object on the road. Maybe with the newer tires which can roll over nails, we can overlook this object (They would then become mandatory for self-driving cars). The next object I can think of would be a solid brick placed on the road which even though small, could change the trajectory of the car. Other such objects like tires, tin cans, potholes, etc. could be imagined that would have a similar impact.

The autonomous car machine vision has to detect such an object at a far enough distance to take appropriate measures (steer, brake/slow down or prepare for collision). With a speed of 100 mph and a dry road with friction of 0.7, a braking/sensing range of 190 m is calculated [13]. A modular USA brick with dimensions of 194 × 92 × 57 mm would subtend an angle of ~2 arc min ($\tan^{-1}$ 65/100,000). This level of resolution would be outside the capability of a standard VGA camera.

After detection, the object has to be classified before an action can be taken on how to deal with it. The kinds of objects the car could come across on its path depends very much geo fenced location. Objects on the US road freeways and urban streets could be very different from those in India or china. This is the point where the admiration for the human senses and brain capacity start daunting current computer chips.

5. Sensor fusion

5.1. Need for sensor fusion

For self-driving cars to be accepted by society, they would have to demonstrate significantly lower probability of collision – when compared to human drivers. A 2016 study by Virginia Tech Transportation Institute [14] found that self-driving cars would be a comparable or a little better than humans for severe crashes, but significantly better at avoiding low severity level crashes (level 3). The level 3 crash rate was calculated at 14.4 crashes per million miles driven for humans and 5.6 crashes for self-driving cars.

To keep things in perspective, we could estimate an average person in USA to drive 900,000 miles in their lifetime (12,000 miles/year × 75 years). Also note that the above report uses only Google

Object_list	RADAR	Camera	LIDAR	Sensor Fusion
Car@150m		Don't See it (Noise)		
Not_Classified@100 m & low light				Evaluate TTC & brake if unresolved ?
@50m				Person on bicycle
Not classified	Don't see it (Noise)			Brake or ignore ?
Potholes & stuff		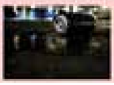		What can be safely ignored ?

Figure 7. The challenge of sensor fusion – illustrated.

self-driving car data. These cars are known to have a full suite of sensors (Multiple LIDAR, RADAR, Cameras, Ultrasonic, GPS and other sensors).

The point is that just like the human driver, the car has to integrate the information from multiple sensors and make the best decision possible in the circumstance. On top of that, it has to be way better to get people to start adopting the technology. Knowing that each of the sensor technologies has some limitation, the need to fuse multiple inputs reliably is a daunting task. Incorrect or poor implementation of the sensor fusion could quickly take the car back to the dealer show room.

5.2. Challenges to sensor fusion

Figure 7 below illustrates the challenge of sensor fusion.

The objective sensor fusion is to determine the environment around the vehicle trajectory with enough resolution, confidence and latency to navigate the vehicle safely.

Figure 7 row 1 shows the ideal case when two sensors agree on an object and the object is detected early enough to navigate the car.

Figure 7 row 2 shows a case where each of the sensors classifies the object differently. In this case, the best option maybe to just agree that it is big enough object to avoid if possible.

Figure 7 row 3 similar situation where a person on a bicycle maybe identified as a person or a bicycle. Again, we could agree that it is an unidentified large moving object that needs to be avoided.

The last two rows shows smaller objects that pose difficult questions. Is it better to run over a small dog than to risk braking and getting rear-ended? Can the pothole be detected and classified early enough to navigate? Is the pothole or object small enough to run over?

These questions will take a longer time to resolve with improving technology in sensing, computing, public acceptance and legislation. The 80/20 Pareto principle would imply that the last 20% of the problems for self-driving cars will take 80% of the time it takes to bring it to mass market.

6. Conclusions

The exponential growth of electronics in the auto industry can be estimated by the number of sensors and electronic control units (ECUs) being added to each newer cars. From a 2003 VW golf (~35 ECUs, 30 sensors); a 2013 Ford Fusion (~70 ECUs, 75 Sensors) to a projection for automated car in 2030 (~120 ECUs, >100 Sensors) [1]. One could be forgiven for imagining the future car to be a supercomputer with wheels.

We are in the initial growth spurt for autonomous cars. A lot of technology still remains to be innovated and matured before regulation and standards kick-in. LIDAR technology is still evolving – range, resolution, eye safety, form factor and cost of the technology is improving rapidly. Camera hardware for medium range and VGA resolution has matured – but needs improvement in range (200 m target), resolution (>8 Megapixel) and performance under poor lighting or with infrared. Sensor fusion architectures can only be optimized after sensors needed are standardized or at least well understood. Real time operation with use of Artificial Intelligence – Neural networks is still in early stage. Society has still to debate and accept the safety performance with known behavior of these robots on wheels. What a great time for electronics and the Auto industry!

Author details

Rajeev Thakur

Address all correspondence to: rajeev.thakur@osram-os.com

OSRAM Opto Semiconductors, Inc., Novi, United States of America

References

[1] Carlson J. Evolution of ADAS architectures, sensor fusion, and the future of the autonomous car. In: ADAS Sensors Conference (2017); 17-18 May 2017; Detroit, Michigan

[2] Federal Automated Vehicles Policy; Sept 2016; U.S Department of Transportation; www.nhtsa.gov; Docket No. NHTSA-2016-0090; page 5

[3] Surface vehicle recommended practice; Taxonomy and Definitions of terms related to driving automation systems for on-road motor vehicles; SAE J3016_201609; Table 1, page 17

[4] Philip Ronan, Gringer. Revised diagram with re-aligned spectrum; File – EM spectrum.svg and Linear visible spectrum.svg; 19 February 2013;**13**:51:42. Available from: https://en.wikipedia.org/wiki/Electromagnetic_radiation [Accessed: 2017-07-17]

[5] Rfcafe. Solar Spectral Irradiance & PV Cell Operational Regions (ASTM G173-03) [Internet]. 2017. Available from: http://www.rfcafe.com/references/electrical/ASTM-G173-03-Reference-Spectra.htm [Accessed: 2017-07-18]

[6] Vehicle-to-Vehicle Communications: readiness of V2V technology for application – DOT HS 812014; Table V-7; page 105

[7] Millimetre Wave Receiver concepts for 77 GHz automotive radar in silicon Germanium Technology – D.Kissenger (Springer Brief's 2012); Table 2.1 and 2.2; Page 18

[8] Wikipedia. Sunlight [Internet]. 2001; By Nick84 - http://commons.wikimedia.org/wiki/File:Solar_spectrum_ita.svg, CC BY-SA 3.0, [Accessed: 2017-09-05]

[9] Thakur R. ADAS to autonomous – Evolution of LIDAR and infrared camera. In: ADAS Sensors Conference (2017); 17-18 May 2017; Detroit, Michigan

[10] Weber R. Infrared LED Illumination for Sensor Applications [OSRAM Opto Semiconductors Inc - Webinar]; 3 Dec 2015; Detroit, Michigan

[11] National Center for Statistics and Analysis. Distracted Driving 2014 (Traffic Safety Facts Research Note. Report No. DOT HS 812 260). Washington, DC: National Highway Traffic Safety Administration; 2016, April

[12] Department of Transportation, National Highway Traffic Safety Administration Docket No. NHTSA-2010-0053. Visual-Manual NHTSA Driver Distraction Guidelines for In-Vehicle Electronic Devices

[13] Thakur R. Infrared sensors for ADAS and beyond – LIDAR/infrared camera. In: TU-Automotive Conference (2015); 4 October 2015; Novi, Michigan

[14] Blanco M, et al; Automated Vehicle Crash Rate Comparison Using Naturalistic Data (2016); Jan 2016; Virginia Tech Transportation Institute; figure 1; page iv

Experimental and Numerical Study of an Optoelectronics Flexible Logic Gate Using a Chaotic Doped Fiber Laser

Juan Hugo García-López, Rider Jaimes-Reátegui,
Samuel Mardoqueo Afanador-Delgado,
Ricardo Sevilla-Escoboza, Guillermo Huerta-Cuéllar,
Didier López-Mancilla, Roger Chiu-Zarate,
Carlos Eduardo Castañeda-Hernández and
Alexander Nikolaevich Pisarchik

Additional information is available at the end of the chapter

http://dx.doi.org/10.5772/intechopen.75466

Abstract

In this chapter, we present the experimental and numerical study of an optoelectronics flexible logic gate using a chaotic erbium-doped fiber laser. The implementation consists of three elements: a chaotic erbium-doped fiber laser, a threshold controller, and the logic gate output. The output signal of the fiber laser is sent to the logic gate input as the threshold controller. Then, the threshold controller output signal is sent to the input of the logic gate and fed back to the fiber laser to control its dynamics. The logic gate output consists of a difference amplifier, which compares the signals sent by the threshold controller and the fiber laser, resulting in the logic output, which depends on an accessible parameter of the threshold controller. The dynamic logic gate using the fiber laser exhibits high ability in changing the logic gate type by modifying the threshold control parameter.

Keywords: optical logic devices, optoelectronics, fiber laser, chaos

1. Introduction

An important advantage of erbium-doped fiber lasers (EDFLs) over other optical devices is a long interaction length of the pumping light with active ions that leads to a high gain and a

IntechOpen

single transversal-mode operation for a suitable choice of fiber parameters. The EDFL with coherent radiation at the wavelength of 1560 nm is an excellent device for applications in medicine, remote sensing, reflectometry, and all-optical fiber communications networks [1, 2]. Rare-doped fiber lasers subjected to external modulation from semiconductor pump lasers are known to exhibit chaotic dynamics [3–12]. Besides, a very important advantage of the EDFL working in a chaotic regimen is its application to the development of basic logic gates [13], since it can process different logical gates and implements diverse arithmetic operations. The simplicity in switching chaotic EDFL between different logical operations makes this device more suitable for general proposes than traditional computer architecture with fixed wire hardware.

Using a chaotic system as a computing device was proposed by Sinha and Ditto [14], who applied for this purpose a chaotic Chua's circuit with a simple threshold mechanism. After this pioneering work, chaotic computational elements received considerable attention from many researchers who developed new designs allowing higher capacity for universal general computing purposes enable to reproduce basic logic operations, such as AND, OR, NOT, XOR, NAND, and NOR [15–26]. Likewise, a single chaotic element has the ability in reconfiguring into different logic gates through a threshold-based control [15, 16]. This device is also known as reconfigurable chaotic logic gate (RCLGs) and, due to its inherent nonlinear components, has advantages over standard programmable gate array elements [19] where reconfiguration is obtained by interchanging between multiple single-purpose gates. Also, discrete circuits working as RCLGs were proposed to reconfigure all logic gates [17, 18]. Additionally, reconfigurable chaotic logic gates arrays (RCGA), which morph between higher-order functions, such as those found in a typical arithmetic logic unit (ALU), were invented [20]. Recently, some of the authors of this work proposed an optoelectronics flexible logic gate based on a fiber laser [27, 28].

Here, we describe in detail the implementation of the optoelectronics flexible logic gate based on EDFL, which exploits the richness and complexity inherent to chaotic dynamics. Using a threshold controller, NOR and NAND logic operations are realized in the chaotic EDFL.

This chapter is an extension of the article *"Optoelectronic flexible logic gate based on a fiber laser. Eur. Phys. J. Special Topics. 2014"* [27]. It is organized as follows. The theoretical model of the diode-pumped EDFL is described in Section 2. The experimental setup of the optical logic gate based on the EDFL is given in Section 3. Likewise, the discussion of theoretical and experimental results on the application of the NAND and NOR logic gates based on the EDFL as a function of the threshold controller is presented in Section 4. Finally, main conclusions are given in Section 5.

2. Theoretical arrangement

The EDFL is known to be extremely sensitive to external disturbances, which can destabilize its normal operation. This makes this device very promising for many applications where small-amplitude external modulation is required to control the laser dynamics. The mathematical model and experimental arrangement of the EDFL used in this work have been developed by Pisarchik et al. [6–12].

2.1. EDFL theoretical model

Based on the power balance approach, we model diode-pumped EDFL dynamics by considering both the excited-state absorption (ESA) in erbium at the 1560-nm wavelength and the averaged population inversion along the pumped active fiber laser. The model addresses two evident factors, the ESA at the laser wavelength and the depleting of the pump wave at propagation along the active fiber, leading to undumped oscillations experimentally observed in the EDFL without external modulation [6, 12]. The energy-level diagram of the theoretical model used in this work is shown in **Figure 1**.

Using a conventional system for EDFL balance Equations [6, 7], which describe the variations of the intra-cavity laser power P (in units of s^{-1}), that is, the sum of the contrapropagating waves' powers inside the cavity and the averaged population N (dimensionless variable) in the upper laser level "2," we can write EDFL equations as follows:

$$\frac{dP}{dt} = \frac{2L}{T_r} P[r_\omega \alpha_0 (N[\xi - \eta] - 1) - \alpha_{th}] + P_{sp} \tag{1}$$

$$\frac{dN}{dt} = -\frac{\sigma_{12} r_\omega P}{\pi r_0^2} (\xi N - 1) - \frac{N}{\tau} + P_{pump} \tag{2}$$

where N can take values between $0 \le N \le 1$ and is defined as $N = \frac{1}{n_0} L \int_0^L N_2(z)\, dz$, with N_2 as the upper laser-level population density "2," n_0 is the refractive index of an erbium-doped fiber, and L is the length of the active fiber medium; σ_{12} is the cross section of the absorption transition from the state "1" to the upper state "2," σ_{12} is the stimulated cross section of the transition in return from the upper state "2" to the ground state "1," in

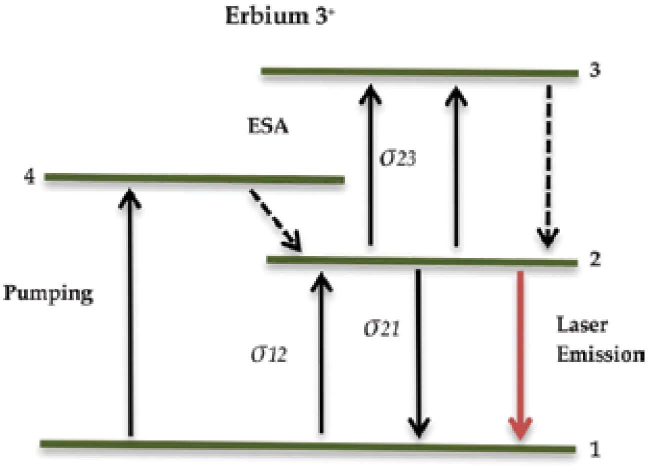

Figure 1. Erbium-doped fiber laser energy diagram.

magnitude practically are the same, that is, $\sigma_{21} = \sigma_{12}$, that gives $\xi = \frac{\sigma_{12}+\sigma_{21}}{\sigma_{12}} = 2$; $\eta = \frac{\sigma_{23}}{\sigma_{12}}$ is the coefficient ratio between excited-state absorption (σ_{23}) and the ground-state absorption cross sections (σ_{12}); $\tau_r = \frac{2n_0(L+l_0)}{c}$ is the photon round-trip time in the cavity (l_0 is the length intra-cavity tails of FBG couplers); $\alpha_0 = N_0\sigma_{12}$ is the small-signal absorption of the erbium fiber at the laser wavelength ($N_0 = N_1 + N_2$ is the total erbium ions' populations density in the active fiber medium); $\alpha_{th} = \gamma_0 + \frac{ln(1/R_B)}{2L}$ is the cavity losses at threshold (γ_0 being the passive fiber losses, R_B is the total reflection coefficient of the fiber Bragg grating (FBG) couplers); τ is the lifetime of erbium ions in the excited state "2"; r_ω is the factor addressing a match between the laser fundamental mode and erbium doped core volumes inside the active fiber, given as

$$r_\omega = 1 - \exp\left[-2\left({}^{r_0}/_{\omega_0}\right)^2\right], \tag{3}$$

where r_0 is the fiber core radius and w_0 is the radius fundamental fiber mode. The spontaneous emission P_{sp} into the fundamental laser mode is taken as

$$P_{sp} = \frac{y10^{-3}}{\tau T_\tau}\left(\frac{\lambda_g}{\omega_0}\right)^2 \frac{r_0^2\alpha_0 L}{4\pi^2\sigma_{12}}. \tag{4}$$

Here, we assume that the erbium luminescence spectral bandwidth (λ_g being the laser wavelength) is 10^{-3}. P_{pump} is the laser pump power given as

$$P_{pump} = P_P \frac{1 - \exp\left[-\beta\alpha_0 L(1-N)\right]}{n_0\pi r_0^2 L}, \tag{5}$$

where P_p is the pump power at the fiber entrance and $\beta = \frac{\alpha_p}{\alpha_0}$ is the dimensionless coefficient that accounts for the ratio of absorption coefficients of the erbium fiber at pump wavelength λ_p to that at laser wavelength λ_g. Eqs. (1) and (2) describe the laser dynamics without external modulation. We add the modulation to the pump parameter as:

$$P_{pump} = P_p^0[1 + A_m \sin(2\pi F_m t)], \tag{6}$$

where P_p^0 is the laser pump power without modulation, A_m and F_m are the modulation amplitude and frequency, respectively.

We perform numerical simulations for the laser parameters corresponding to the following experimental conditions from references [6, 7]: L = 90 cm, n_0 = 1.45 and l_0 = 20 cm, giving T_r = 8.7 ns, $r_0 = 1.5 \times 10^{-4}$ cm, and $w_0 = 3.5 \times 10^{-4}$ cm. The value of w_0 is measured experimentally and using Eq. (3) resulting in r_w = 0.308. The coefficients characterizing the resonant-absorption properties of the erbium fiber at the laser and pump wavelengths are $\alpha_0 = 0.4$ cm^{-1} and $\beta = 0.5$ (corresponding to direct measurements for doped fiber with erbium concentration of 2300 ppm); $\sigma_{12} = \sigma_{21} = 3 \times 10^{-21}$ cm^2 and $\sigma_{23} = 0.6 \times 10^{-21}$ cm^2 giving $\xi = 2$ and $\eta = 0.2$; $\tau = 10^{-2}$ s [6, 7]; $\gamma_0 = 0.038$ and $R_B = 0.8$ with a cavity losses at threshold of

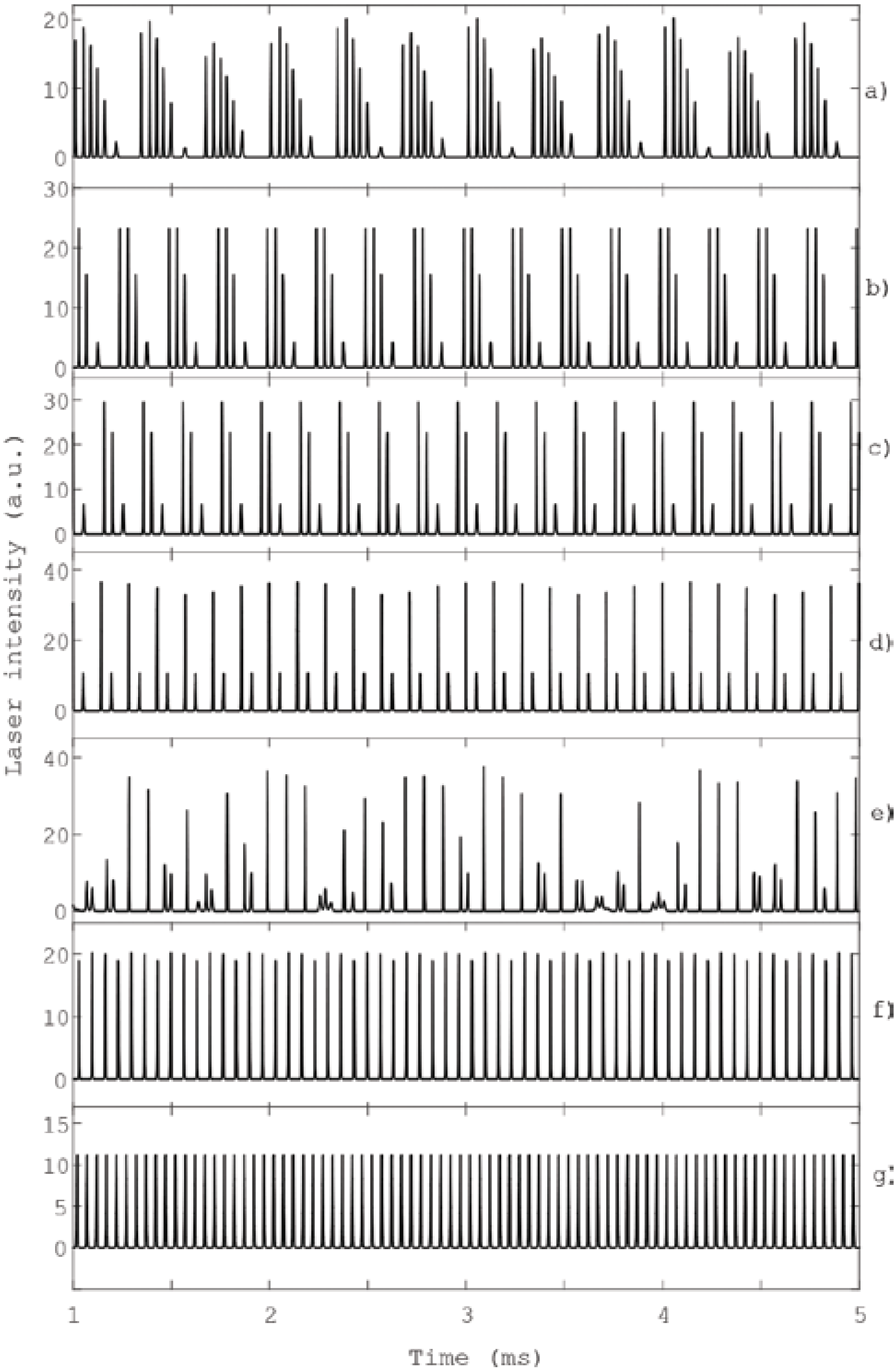

Figure 2. Time series of laser intensity P, with $A_m = 1$, and (a) $F_m = 3$ kHz, (b) $F_m = 4$ kHz, (c) $F_m = 3$ kHz, (d) $F_m = 7$ kHz, (e) $F_m = 10$ kHz, (f) $F_m = 15$ kHz, and (g) $F_m = 20$ kHz.

α_{th} = 3.92 × 10^{-2}. The laser wavelength is λ_g = 1.56 × 10^{-4} cm (photon energy hv_g = 1.274 × 10^{-19} J) corresponding to the maximum reflection coefficients of both FBG's.

The laser threshold is defined as $\varepsilon = P_p/P_{th}$, where

$$P_{th} = \frac{N_{th}}{\tau}\frac{n_0\pi r\omega_p^2 L}{1-\exp\left[-\beta\alpha_0 L\left(1-y_{th}\right)\right]} \tag{7}$$

is the threshold pump power, $N_{th} = \frac{1}{\xi}\left(1+\frac{\alpha_{th}}{r_\omega\alpha_0}\right)$ is threshold population of the level "2" and the radius of the pump beam $w_p = w_0$. In the numerical simulations, we choose the pump power $P_p = 7.4 \times 10^{19}\ \mathrm{s}^{-1}$ that yields the laser relaxation oscillation frequency $f_0 \approx 30$ kHz.

In order to understand the dynamics of the EDFL, the bifurcation diagram of the local maxima of the laser power versus the pump modulation frequency F_m is calculated. To perform numerical simulations, we normalize Eqs. (1) and (2) (as described in the appendix of reference [29]) and obtain the following equations:

$$\frac{dx}{dt} = axy - bx + c(y + r_\omega), \tag{8}$$

$$\frac{dy}{dt} = -dxy - (y + r_\omega) + e\left\{1 - exp\left[-\beta\alpha_0 L\left(1 - \frac{N_2 + r_\omega}{\xi_2 r_\omega}\right)\right]\right\}, \tag{9}$$

Figure 2 presents the time series of the laser intensity at the following driven frequencies: (a) F_m = 3 kHz, the laser behavior is chaotic, (b) F_m = 4 kHz, the EDFL response is a period 4, (c) F_m = 3 kHz, the EDFL response is a period 3, (d) F_m = 7 kHz, the EDFL response is a period 2, (e) F_m = 10 KHz, chaos, (f) F_m = 15 kHz and (g) F_m = 20 kHz, a period 1 with decreasing amplitude as the modulation frequency is increased.

The constant parameters of Eqs. (8) and (9) are shown in **Table 1** [30].

Figure 3 shows the numerical bifurcation diagram of the laser peak intensity versus the modulation frequency (0–20 kHz) for the 100% modulation depth (A_m = 1). The laser dynamical behavior (periodic or chaotic) is determined by the modulation frequency.

In this work, we are interested in a chaotic regime. **Figure 4** shows the times series corresponding to chaos for F_m = 10 kHz.

Constant parameter	Values (a.u.)
a	6.6207×10^7
b	7.4151×10^6
c	0.0163
d	4.0763×10^3
e	506

Table 1. Normalized constant parameters of Eqs. (8) and (9).

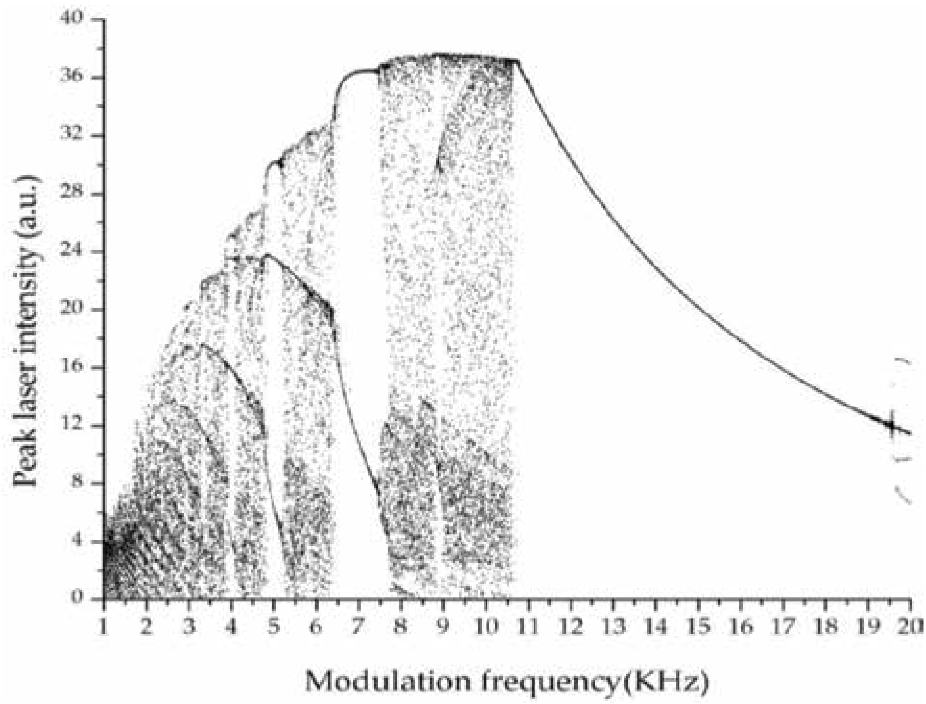

Figure 3. Numerical bifurcation diagram of laser peak intensity versus modulation frequency (F_m) for A_m = 1.

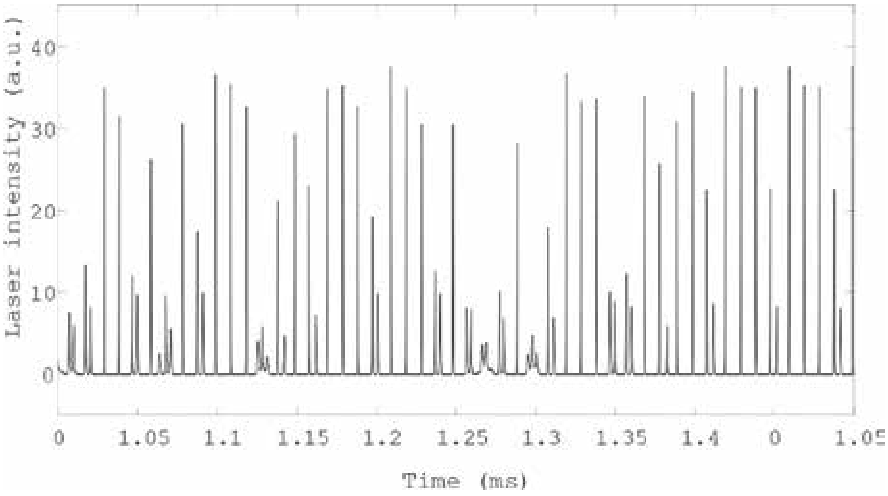

Figure 4. Time series of laser intensity P for F_m = 10 kHz and A_m = 1.

3. Implementation of the optoelectronics flexible logic gate using the EDFL

Figure 5 shows the scheme of the proposed optoelectronics flexible logic gate using the EDFL. The reconfigurable logical gate contains two principal elements: a chaotic EDFL and a threshold controller. The dynamics behavior of the EDFL is described by the balance Eqs. (1) and (2). The threshold controller compares laser power P with value V_T generated by the controller that releases output $V_T = E$ if $P > E$ and $V_T = P$ otherwise, with E as threshold value. This output signal V_T is added to the diode pump current P_{pump} with a coupling coefficient K. The logic gate output subtracts V_T from P yielding $V_0 = P - V_T$. Next, we consider the laser and the controller models separately.

3.1. Threshold controller

In our numerical simulations, we use the laser power P calculated by Eqs. (1), (2), and (6) as the input signal for the threshold controller. The output signal V_T from the controller is used to control the diode pump current as:

$$P_{pump} = P_p[1 + A_m \sin(2\pi F_m t) + KV_T] \tag{10}$$

The threshold controller has two logic inputs 0 and 1, which generate the corresponding values I_1 and I_2, where $I_{1,2} = 0$ for input 0 and $I_{1,2} = V_{in}$ otherwise, where V_{in} is a certain value to define the threshold for E. A type of the logic gate is determined by a parameter V_c. The procedure to obtain this parameter is explained in detail in section Results and Discussions.

The controller generates an initial value E defined by the inputs I_1 and I_2 being either 0 or V_{in} and takes the value:

$$E = V_c + I_1 + I_2 \tag{11}$$

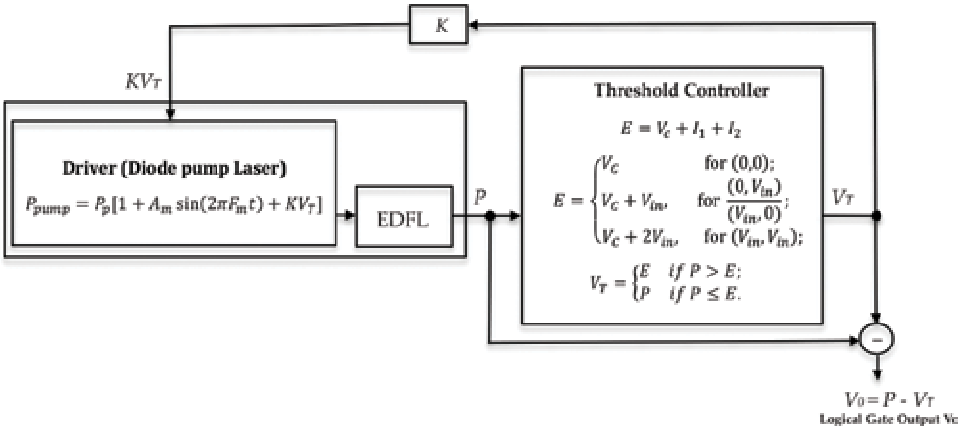

Figure 5. Arrangement of the optoelectronics logic gate. E is the threshold controller, V_c determines the logic response, $I_{1,2}$ is the logic input which takes the value of either V_{in} or 0, V_T is the output controller signal, P is the laser output intensity, P_{pump} is the diode laser pump intensity, P_p is the continuous component of the pumping, A_m and F_m are the modulation depth and frequency, and K is the gain factor.

so that there are three possible options:

$$E = \begin{cases} V_C & \text{for } (0,0), \\ V_C + V_{in}, & \text{for } \dfrac{(0, V_{in})}{(V_{in}, 0)}, \\ V_C + 2V_{in}, & \text{for } (V_{in}, V_{in}). \end{cases} \tag{12}$$

The controller output is determined as:

$$V_T = \begin{cases} E & \text{if } P > E, \\ P & \text{if } P \leq E. \end{cases} \tag{13}$$

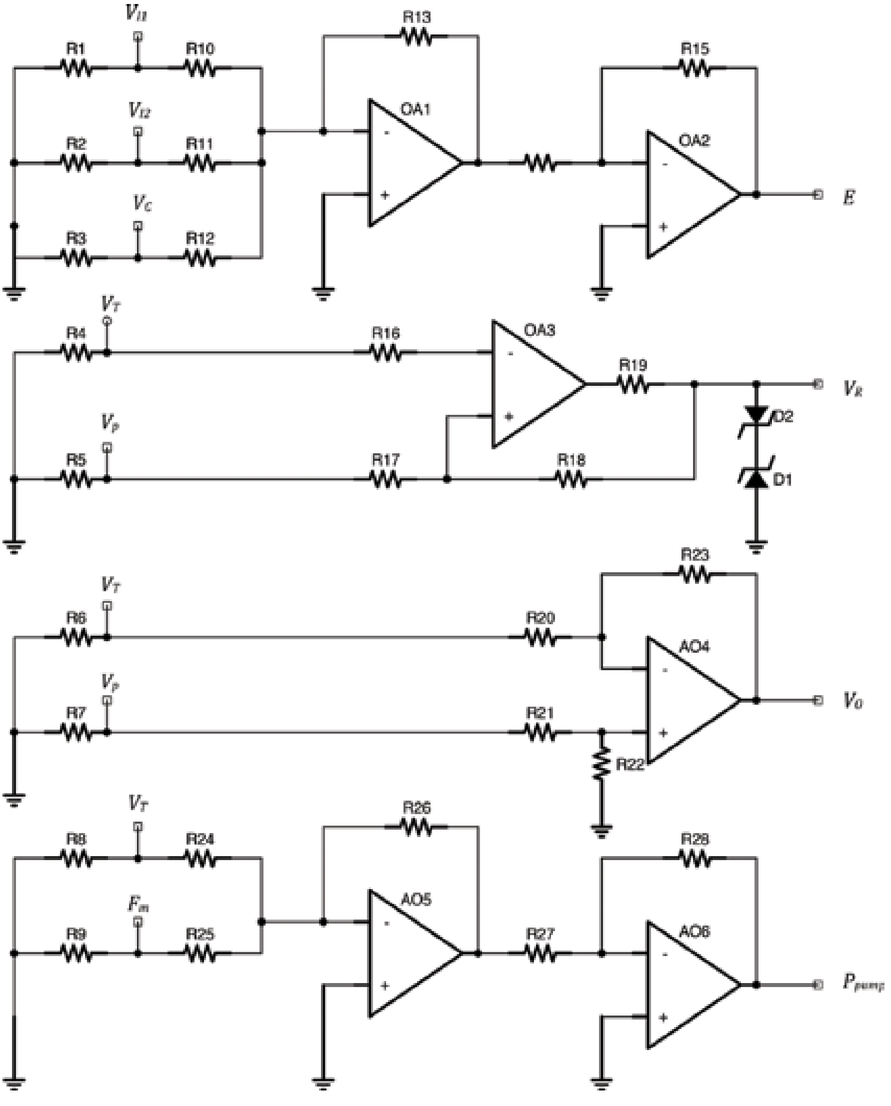

Figure 6. Electronic circuits of the threshold controller.

where V_T becomes the threshold signal.

Figure 6 shows the electronic circuits in the controller to generate E, V_R, $V_{0,}$ and P_{pump} signals. The electronic components used in the controller are presented in **Table 2**.

3.2. EDFL experimental arrangement

The experimental arrangement presented in **Figure 7** consists of EDFL pumped by a laser diode (LD) from Thorlabs PL980 operating at 1560 and 977 nm, respectively. The Fabry-Perot fiber laser cavity with total length of 4.81 m is formed by an active, long EDFL of 88-cm length, and a 2.7-μm core diameter, incorporating two fiber Bragg gratings (FBG1 and FBG2) with 0.288 and 0.544-nm full widths on half-magnitude bandwidth, having, respectively, ∽100% and ∽96%

Electronic component	Value
R1–R9	100 Ω
R10–R15, R17, R19–R28	10 kΩ
R16	100 KΩ
R18	2.2 MΩ
C1, C2	100 μF
D1, D2	Zener diode
OA1 – OA6	LM741CN
I/O	Phoenix connector

Table 2. Parameters for electronic components of circuits shown in **Figure 6**.

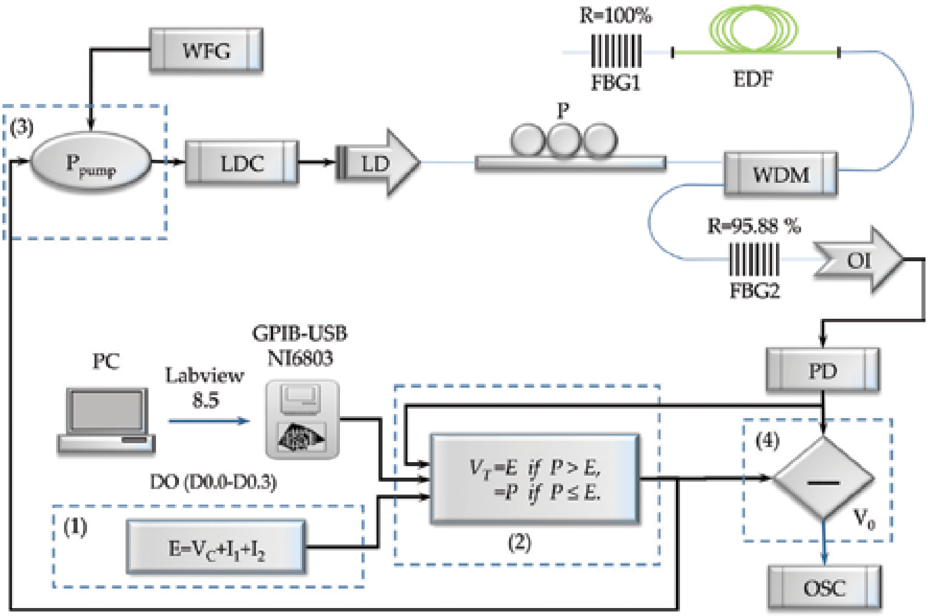

Figure 7. Experimental scheme of the optoelectronics logical gate based on EDFL.

reflectivity at the laser operating wavelength. A fiber laser formed by an erbium doped fiber (EDF) and two Bragg gratings (FBG1 and FBG2), is externally driven by the harmonic pump signal $P_{pump} = P_p[1 + A_m \sin(2\pi F_m t) + KV_T]$ (through a sum circuit CI 741) applied to a diode pump laser (LD) current via a laser diode controller (LDC) from a wave function generator (WFG). A single-mode fiber is used to connect the optical components.

The current and temperature of the LD are controlled by a laser diode controller (LDC) (Thorlabs ITC510). The 145.5-mA pump current is selected to guarantee that the laser relaxation oscillation frequency is around $F_r = 30$ kHz to provide a 20-mW power; which is above a 110-mA EDFL threshold current. A harmonic modulation signal $A_m \sin(2\pi F_m t)$ from wave function generator (WFG) (Tektronix AFG3102) is supplied to the diode pump current. The fiber laser output after passing through a polarization controller (P), wavelength division multiplexer (WDM), and an optical isolator (OI) is recorded with a photodiode (PD), and the electronic signal is compared with the signal generated by the threshold controller. The threshold controller with $E = V_c + I_1 + I_2$ is a summing circuit (CI 741) with dynamical control signal Vc and inputs logic signals $I_{1,2}$ controlled by a USB NI 6803, V_T is a comparator circuit between laser intensity P and threshold controller E. The logic gate output V_0 is sent back to the driver (P_{pump}) of the EDFL to change its dynamics. The signals P from the EDFL, $I_{1,2}$, V_T, and V_0 from the threshold controller are analyzed with a multichannel oscilloscope.

4. Results and discussions

4.1. Numerical results

In order to use the arrangement of the optoelectronics logic gate shown in **Figure 5**, it is necessary to determine V_c and V_{in} signals and find the required logic gates NAND or NOR.

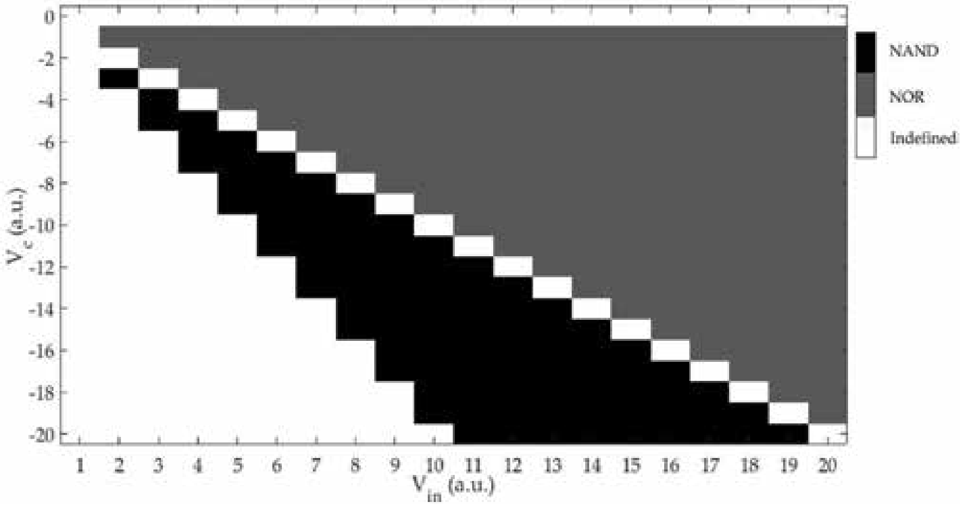

Figure 8. Diagram of values for V_c and V_{in} to determine the logic gate type, either NAND or NOR.

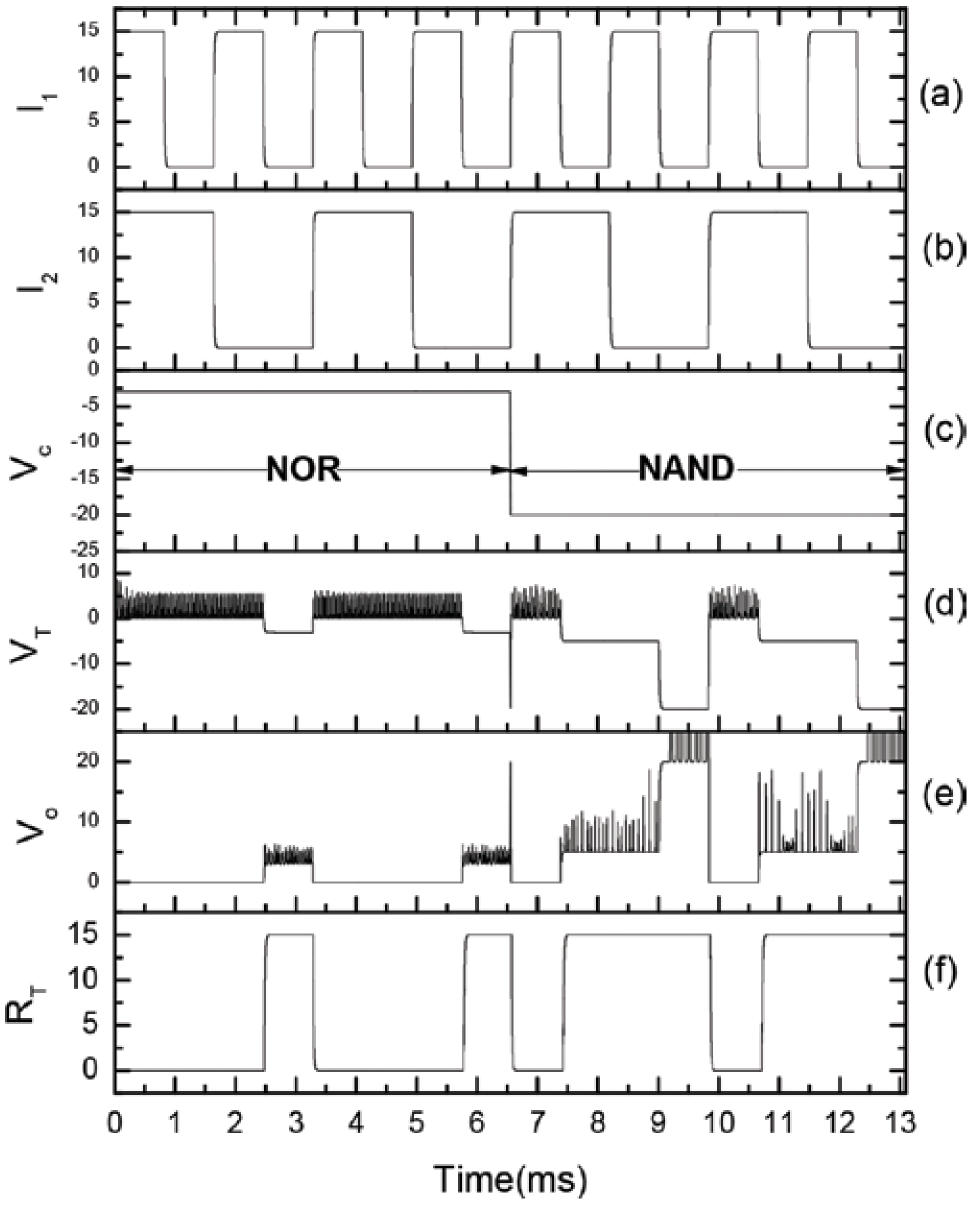

Figure 9. Numerical simulation results. (a)–(b) inputs $I_{1,2}$, (c) dynamical control signal V_c, (d) threshold controller signal V_T, (e) logic gate output V_0, and (f) recover logic output from signal V_0.

The value of V_c was gradually changed (-20 V < V_c < 2 V) and for each value of V_c the value of V_{in} was changed (2 V < V_{in} < 20 V). **Figure 8** shows the values of V_c versus V_{in} which we use to determine the logical gates NAND and NOR. If we set the parameter V_{in} = 10 V and V_c varies from −1 to −9 V, we get the NOR gate; but if V_c changes from −11 to −20 V, the NAND gate is used.

The numerical results of NOR and NAND operations of the reconfigurable dynamic logic gate Eqs. (1), (2), and (10)–(13) are shown in **Figure 9** for $A_m = 1$ V and $F_m = 10$ kHz.

For the time interval from $t = 0$ to 6.5 ms, we have a NOR logic gate, where the signal from $V_c = -3$ V to $V_{in} = 15$ V produces three different combinations of the threshold controller V_T as

1. For input $I_{1,2} = (V_{in}, V_{in})$, $E = 27$ resulting in $P \leq E$ and the threshold level $V_T = P$, that yields $V_0 = 0$.
2. For input $I_{1,2} = (0, V_{in})/(V_{in}, 0)$, $E = 12$ resulting in $P \leq E$ and the threshold level $V_T = P$, that yields $V_0 = 0$.
3. For input $I_{1,2} = (0, 0)$, $E = V_c = -3$ resulting in $P > E$ and the threshold level $V_T = E$, that yields $V_0 = P - E$.

For the time interval from $t = 6.5$ to $t = 13$ ms, **Figure 9** shows a NAND logic gate, where the signal from $V_c = -20$ V to $V_{in} = 15$ V produces three different combinations of the threshold controller V_T as

1. For input $I_{1,2} = (V_{in}, V_{in})$, $E = V_c + I_1 + I_2 = V_c + 2V_{in} = 10$ resulting in $P \leq E$ and the threshold level $V_T = P$, that yields $V_0 = 0$.
2. For input $I_{1,2} = (0, V_{in})/(V_{in}, 0)$, $E = V_c + I_1 + I_2 = V_c + V_{in} = -5$ resulting in $P > E$ and the threshold level $V_T = E$, that yields $V_0 = P - E$.
3. For input $I_{1,2} = (0, 0)$, $E = V_c = -20$ resulting in $P > E$ and the threshold level $V_T = E$, that yields $V_0 = P - E$.

4.2. Experimental results

Similar to the results of the numerical simulations, a change was made in the parameters for V_c versus V_{in} to determine required NAND or NOR logic gates. **Figure 10** shows the values of V_c

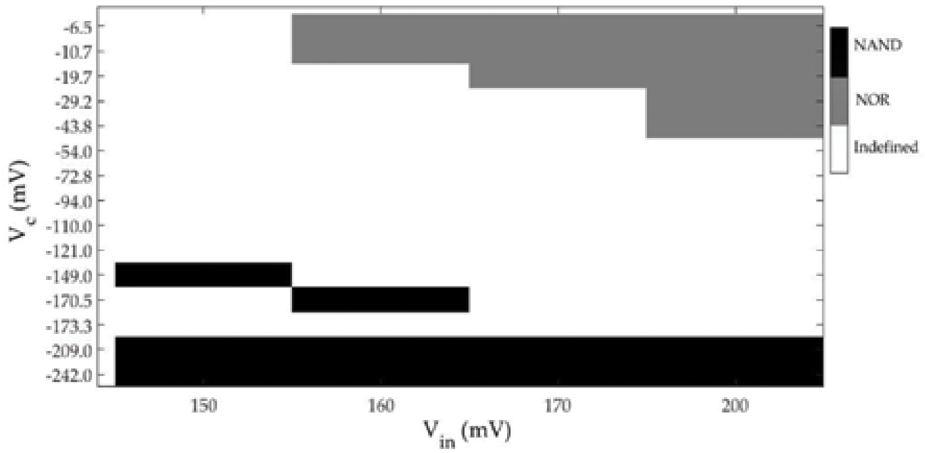

Figure 10. Diagram of values for V_c and V_{in} to determine the logic gate type, either NAND or NOR.

versus V_{in} which we use to determine the NAND and NOR logic gates. If we set the parameter $V_{in} = 160$ mV and changes $V_c = -10.7$ mV, we get the NOR gate, but if we change $V_c = -170.3$ mV, the NAND gate is used.

Figure 11 and **Table 3** show the experimental results of the dynamic NOR and NAND logic operations for $A_m = 700$ mV, $F_m = 15$ kHz, and $V_{\text{in}} = 200$ mV. The NOR gate corresponds to the time series from $t = 0$ ms to $t = 8$ ms for V_c = ©40 mV, and for the NAND gate for the time series

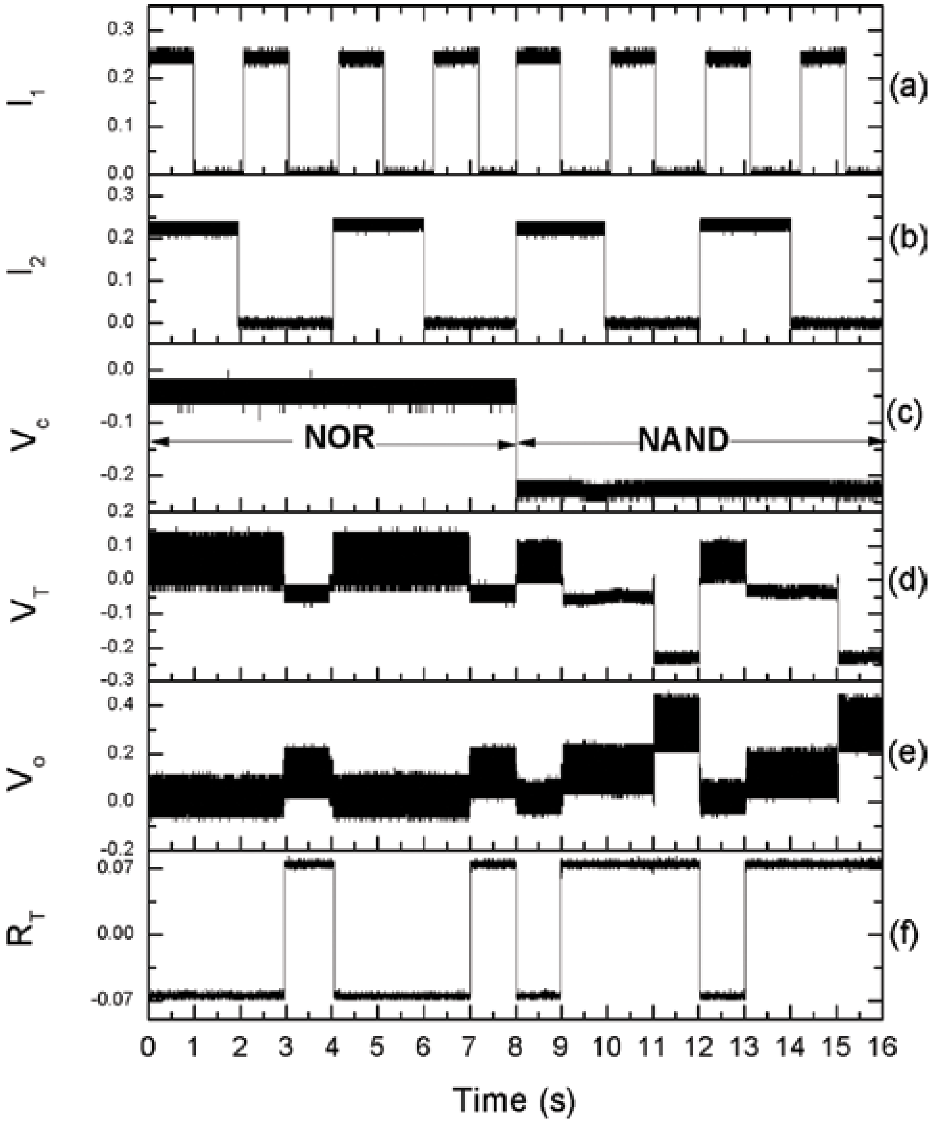

Figure 11. Experimental results. (a)–(b) inputs $I_{1,2}$, (c) dynamical control signal Vc, (d) threshold controller signal V_T, (e) logic gate output V_0, and (f) recover logic output from signal V_0.

	(I_1, I_2)	Time	Threshold controller E	V_T	V_O
	(mV)	(ms)	(mV)	(mV)	(mV)
NOR	$(0, 0)$	3–4	$E = V_c \sim -40$	$E \le P$	$V_O = P - V_T = P - E$
		7–8		$V_T = E$	
	$(V_{in}, 0)$ or $(V_{in}, 0)$	1–3	$E = V_c + V_{in} \sim 160$	$E > P$	$V_O = P - V_T = P - P = 0$
		5–7		$V_T = P$	
	(V_{in}, V_{in})	0–1	$E = V_c + 2 * V_{in} \sim 360$	$E > P$	$V_O = P - V_T = P - P = 0$
		4–5		$V_T = P$	
NAND	$(0, 0)$	11–12	$E = V_c{}^{\sim} -220$	$E \le P$	$V_O = P - V_T = P - E$
		15–16		$V_T = E$	
	$(V_{in}, 0)$ or $(V_{in}, 0)$	9–11	$E = V_c + V_{in} \sim -20$	$E \le P$	$V_O = P - V_T = P - E$
		13–15		$V_T = E$	
	(V_{in}, V_{in})	8–9	$E = V_c + 2 * V_{in} \sim 180$	$E > P$	$V_O = P - V_T = P - P = 0$
		12–13		$V_T = P$	

Table 3. Experimental data for implementation of NOR and NAND optoelectronics logical gates.

from $t = 8$ to $t = 16$ ms for $V_c = -220$ mV. By comparing **Figure 9** with **Figure 11**, we can see a good agreement between the numerical and experimental results.

5. Conclusions

In this chapter, we have described the implementation of an optoelectronics logic gate based on a diode-pumped EDFL. We have demonstrated good functionality of our system for NOR and NAND logic operations, taking advantage of optical chaos and a threshold controller. The system was controlled by a split signal from the threshold controller, allowing the diode pump laser to mismatch between the output threshold controller signal and the output EDFL signal. The numerical results obtained from the EDFL equations have displayed good agreement with the experimental results. We have demonstrated that the chaotic dynamic behavior of the diode-pumped EDFL and the electronic threshold controller can be successfully used to obtain NAND or NOR logic gates to be constructive bricks of different logic systems. The main contribution of the developed optoelectronics logic gate is addressed in optical computing. The proposed device is more adaptable and faster than a conventional wired hardware, since it can be implemented as an arithmetic processing unit or an optical memory RAM.

Acknowledgements

We gratefully acknowledge support and funding from the University of Guadalajara (UdeG), (R-0138/2016) under the project: Equipment of the research laboratories of the academic groups of the CULAGOS with orientation in optoelectronics, Agreement RG/019/2016-UdeG, Mexico.

Author details

Juan Hugo García-López[1]*, Rider Jaimes-Reátegui[1], Samuel Mardoqueo Afanador-Delgado[1], Ricardo Sevilla-Escoboza[1], Guillermo Huerta-Cuéllar[1], Didier López-Mancilla[1], Roger Chiu-Zarate[1], Carlos Eduardo Castañeda-Hernández[1] and Alexander Nikolaevich Pisarchik[2]

*Address all correspondence to: jhugo.garcia@academicos.udg.mx

1 Department of Exact Sciences and Technology, University of Guadalajara, Lagos de Moreno, Jalisco, Mexico

2 Center for Biomedical Technology, Technical University of Madrid, Madrid, Spain

References

[1] Digonnet M, Snitzer E. Rare earth doped fiber lasers and ampliers. In: Digonnet MJF, editor. Marcel Dekker, Chapter 5; 1993. ISBN-13: 978-0824704582, ISBN-10: 0824704584

[2] Luo LG, Chu PL. Optical secure communications with chaotic erbium-doped fiber lasers. Journal of the Optical Society of America B. 1998;**15**:2524-2530. DOI: https://doi.org/10.1364/JOSAB.1-5.002524

[3] Saucedo-Solorio JM, Pisarchik AN, Kiŕyanov A V, Aboites V. Generalized multistability in a fiber laser with modulated losses. Journal of the Optical Society of America B. 2003;**20**: 490-496. DOI: https://doi.org/10.1364/JOSAB.20.000490

[4] Pisarchik AN, Barmenkov YuO, Kiryanov AV. Experimental characterization of the bifurcation structure in an erbium-doped fiber laser with pump modulation. IEEE Journal Quantum Electronics. 2003;**39**:1567-1571. DOI: 10.1109/JQE.2003.819559

[5] Pisarchik AN, Barmenkov Yu O, Kiryanov AV. Experimental demonstration of attractor annihilation in a multistable fiber laser. Physical Review E. 2003;**68**. DOI: https://doi.org/10.1103/PhysRevE.68.066211

[6] Reátegui RJ, Kiryanov AV, Pisarchik AN, Barmenkov Yu O, Ilichev NN. Experimental study and modelling of coexisting attractors and bifurcations in an erbium-doped fiber laser with diode-pump modulation. Laser Physics. 2004;**14**:1277

[7] Pisarchik AN, Kiryanov AV, Barmenkov Yu O, Jaimes-Reategui R. Dynamics of an erbium-doped fiber laser with pump modulation: theory and experiment. Journal of the Optical Society of America B. 2005;**22**:2107. DOI: https://doi.org/10.1364/JOSAB.22.002107

[8] Huerta-Cuellar G, Pisarchik AN, Barmenkov Yu O. Experimental characterization of hopping dynamics in a multistable fiber laser. Physical Review E. 2008;**78**. DOI: https://doi.org/10.1103/PhysRevE.78.035202

[9] Pisarchik AN, Jaimes-Reátegui R. Control of basins of attraction in a multistable fiber laser. Physics Letters A. 2009;**374**:228. DOI: https://doi.org/10.1016/j.physleta.2009.10.061

[10] Huerta-Cuellar G, Pisarchik AN, Kiryanov AV, Barmenkov Yu O, Del Valle Hernández J. Prebifurcation noise amplification in a fiber laser. Physical Review E. 2009;**79**:1. DOI: https://doi.org/10.1103/PhysRevE.79.036204

[11] Pisarchik AN, Jaimes-Reátegui R, Sevilla-Escoboza R, Huerta-Cuellar G, Taki M. Rogue waves in a multiestable system. Physical Review Letters. 2011;**107**:1. DOI: https://doi.org/10.1103/PhysRevLett.107.274101

[12] Pisarchik AN, Jaimes-Reátegui R, Sevilla-Escoboza JR, Huerta-Cuellar G. Multistable intermittency and extreme pulses in a fiber laser. Physical Review E. 2012;**86**:1. DOI: https://doi.org/10.1103/PhysRevE.86.056219

[13] Ditto WL, Murali K, Sinha S. Chaos computing: Ideas and implementations. Philosophical Transactions of the Royal Society A. 2008;**366**:653-664. DOI: 10.1098/rsta.2007.2116

[14] Sinha S, Ditto W L. Dynamics based computation. Physical Review Letters. 1998;**81**;2156. DOI: https://doi.org/10.1103/PhysRevLett.81.2156

[15] Sinha S, Munakata T, Ditto WL. Flexible parallel implementation of logic gates using chaotic elements. Physical Review E. 2002;**65**:1. DOI: https://doi.org/10.1103-/PhysRevE.65.036216

[16] Sinha S, Ditto WL. Computing with distributed chaos. Physical Review E. 1999;**60**:363. DOI: https://doi.org/10.1103/PhysRevE.60.363

[17] Murali K, Sinha S, Ditto W L. Construction of a reconfigurable dynamic logic cell. Pramana. 2005;**64**:433. DOI https://doi.org/10.1007/BF02704569

[18] Murali K, Sinha S, Ditto WL. Implementation of a NOR gate by a chaotic chua's circuit. International Journal of Bifurcation and Chaos. 2003;**13**:2669. DOI: https://doi.org/10.1142-/S0218127403008053

[19] Taubes G. Computer design meets Darwin. Science. 1997;**277**:1931. DOI: https://doi.org/10.1126/science.277.5334.1931

[20] Ditto W, Sinha S, Murali K. US Patent Number 07096347. 2006

[21] Prusha BS, Lindner J F. Nonlinearity and computation: implementing logic as a nonlinear dynamical system. Physics Letters A. 1999;**263**:105. DOI: https://doi.org/10.1016/S0375-9601(99)00665-9

[22] Cafagna D, Grassi G. Dynamic behaviour and route to chaos in experimental boost converter. International Symposium on Signals, Circuits and Systems. 2005;**2**:745. DOI: 10.1109 /ISSCS.2005.1511348

[23] Chlouverakis KE, Adams MJ. Optoelectronic realisation of NOR logic gate using chaotic two-section lasers. Electronics Letters. 2005;**41**:359. DOI: http://dx.doi.org/10.1049/el:20058026

[24] Jahed-Motlagh MR, Kia B, Ditto WL, Sinha S. Fault tolerance and detection in chaotic computers. International Journal of Bifurcation and Chaos. 2007;**17**:1955-1968. DOI: https://doi.org/10.1142/S0218127407018142

[25] Murali K, Miliotis A, Ditto W L, Sinha S. Logic from circuit elements that exploit nonlinearity in the presence of a moise floor. Physics Letters A. 2009;**373**:1346. DOI: https://doi.org/10.1016/j.physleta.2009.02.026

[26] Ditto WL, Miliotis A, Murali K, Sinha S. The chaos computing paradigm. In: HeinzGeorg Schuster, editor. Reviews of Nonlinear Dynamics and Complexity. Vol. 3. Weinheim: WILEY-VCH Verlag GmbH & Co. KGaA; 2010. p. 1-35. ISBN: 978-3-527-40945-7

[27] Jaimes-Reategui R, Afanador-Delgado SM, Sevilla-Escoboza R, Huerta-Cuellar G, Hugo G-LJ, Lopez-Mancilla D, Castañeda-Hernandez C, Pisarchik AN. Optoelectronic flexible logic gate based on a fiber laser. The European Physical Journal Special Topics. 2014;**223**: 2837-2846. DOI: 10.1140/epjst/e2014-02297-4

[28] García-López JH, Jaimes-Reátegui R, Afanador-Delgado SM, Sevilla-Escoboza R, Huerta-Cuellar G, Casillas-Rodríguez FJ, López-Mancilla D, Pisarchik AN. Optoelectronic flexible logic-gate using a chaotic erbium doped fiber laser, experimental results. In: *Latin America Optics and Photonics Conference*. OSA Technical Digest (online) (Optical Society of America, 2014), paper LTu4A.36. DOI: https://doi.org/10.1364/LAOP.2014.LTu4A.36

[29] Jaimes-Reátegui R. Dynamic of Complex System with Parametric Modulation Duffing Oscillators and a Fiber Laser (Thesis). Leon, Guanajuato, Mexico: Center for Optical Research; 2004

[30] Afanador Delgado SM. Implementación opto-electrónica de una compuerta lógica dinámicamente configurable usando un láser de fibra (thesis). Lagos de Moreno, Jalisco, Mexico: CULagos, University of Guadalajara; 2014

Section 3

Light Harvesters

Chapter 7

Perovskite Solar Cells: The Challenging Issues for Stable Power Conversion Efficiency

Hilal Ahmad Reshi and Rayees Ahmad Zargar

Additional information is available at the end of the chapter

http://dx.doi.org/10.5772/intechopen.75406

Abstract

Despite the advanced processing advantages for low cost, flexible and highly efficient solar cells, the technology is still facing the challenges with regard to the stability of materials in terms of moisture, thermal, light and oxygen atmosphere. The recent discovery of lead halide perovskite has increased a surge of interest in the field of photovoltaics. The chapter highlights some ways that can improve the stability and reducing the toxicity without compromising the efficiency of perovskite. Most of the part includes the review on the actual knowledge and cutting edge research results of high efficiency perovskites. It further describes the materials (Oxides and hybrid halides) that can be used for real time solar cell applications.

Keywords: halide-perovskite, photovoltaics, solar cells

1. Introduction

The rapidly growing rate of consumption of natural resources increases the demand for clean and everlasting option capable of providing indefinite and sustainable energy. Tackling with this global energy crisis is undoubtedly one of the most substantial scientific challenges of present era. Not only this, but the levels of greenhouse gases being emitted in the atmosphere are alarming, which reveals that the existing energy trends are also problematic in terms of economic and environment point of view [1]. Utilization of renewable sources and particularly solar energy provides the most solid alternative viable long term solution to this problem. The growing awareness about the urgency and benefits of solar energy systems will automatically push the efforts towards largely decarbonized energy systems. Arguably the most abundant and renewable energy source is sunlight with over 1000 W/m^2 of energy is falling at the surface of earth at sea level on clear sunny day. As a matter of fact, the solar energy that hits our planet in 1 hour is equal to the total amount of energy consumed by all humans of the world in a year. Indeed, coverage of less than 1% of the earth's surface would be sufficient to meet the world's energy needs using the latest commercially available solar panels. However, to compete the solar energy devices with fossil fuels in utility scale power generation, the necessary requirement is to reduce the total cost of solar energy either by low cost of solar device materials or by increased efficiency. Light energy conversion applications are of different types, among them photovoltaics consists of a number of established as well as emerging technologies. The solar cell is a photoelectric device which can directly convert solar energy into electric energy and offers the light absorbing capacity, long life cycle and less maintenance requirements. The first silicon based single crystal p-n junction solar cell was published in 1954 [2]. The study then increased exponentially over a half a century moving from crystalline silicon to inorganic, dye-sensitized, polymer and now perovskite solar cells. With regard to the commercialized modules, crystalline silicon devices are currently representing the 90% of global share [3]. Research and innovation over the years have led to the thriving performances of around 25% efficiency with a lifetime of 20 years in silicon based devices [4, 5]. This increased performance has forced many countries to initiate the economic programmes for producing electrical energy from renewable sources to civil and industrial sectors. During the last few years, the retail cost of silicon based photovoltaic devices/modules has reduced by ~70% which makes it possible to generate the revenues to develop this field further. Hence it makes some real image to realize innovative photovoltaic systems that can fulfill the actual demand of pollution free sustainable and stable energy. The perovskites is the most dominant of a wide family of materials with general formula ABX_3 type in which A = organic cation, B = metallic cation and X = halide anion. The A cation is found to be somewhat larger than B. **Figure 1** represents the crystal structure of $CH_3NH_3PbI_3$ perovskite a best known as a photoabsorbing material. Several properties such as ferroelectric, ferromagnetic, antiferromagnetic, piezoelectric, semiconducting, superconducting, conducting, insulating, catalysis etc. have been found in these materials since many years [6].

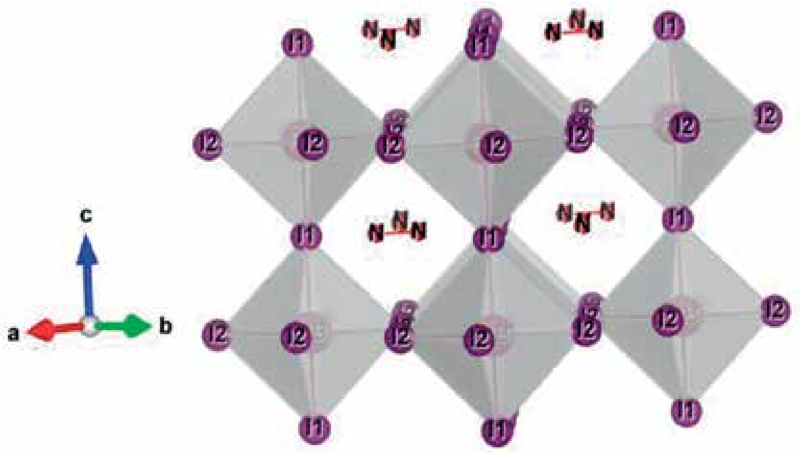

Figure 1. Typical perovskite crystal structure of $CH_3NH_3PbI_3$.

Organic solar cells have received an extensive amount of attention for renewable energy sources because of advantageous features such as low cost, flexibility, light weight and solution based fabrication [7]. However the first photovoltaic application was found in halide based perovskite $CH_3NH_3Pb(I_3, Br_3)$ by Miyasaka and his associates as an absorber material for the devices giving less than 1% power conversion efficiency for solid state cells [8]. The further optimization triggered in 2012 when the $CH_3NH_3PbI_3$ (MAPI) and its mixed halide crossed the 10% efficiency mark [9, 10]. The progress has been observed rapidly over the years and the power conversion efficiency exceeds 20% using organo-lead halide perovskite [11, 12]. The most studied perovskites in terms of multifunctional applications are oxides due to their electrical, magnetic and ferroelectric properties. Halide perovskites initially received a little attention until layered organo-metallic halide perovskites were reported to exhibit a semiconductor to metal transition with increased dimensionality [13]. In 2013, perovskite solar cell technology was declared as one of the biggest scientific breakthroughs by the editors of Science and Nature [14]. However this breakthrough observed in solution based perovskites has drawback that the high efficiency can be obtained only in lead based perovskites which is arguably a substantial hurdle for various applications due to its toxic nature, even though the amount of concentration of lead is very less. This opens a new area of research to find some alternative approach for the replacement of lead without hampering the cell efficiency, durability and stability.

For future large scale solar photovoltaic, a material is required to meet some important parameters such as the material should be earth abundant, cost effective, and non-toxic. In addition, to achieve the high power conversion efficiency, the material must meet some principle properties such as electrical, optical and some defect properties such as direct tunable bandgap, absorption coefficient, and long carrier diffusion length. Many research groups took up the challenge to substitute the lead in order to find out some new non-toxic and stable perovskite materials suitable for photovoltaic applications.

Current efforts are under way to improve the stability and durability of perovskite solar cells. There are two main strategies which deserve an immediate attention to develop the stable solar cell and that is to protect the absorber from the external assaults by developing specialized functional barrier structures and to improve the resilience and stability of the absorber itself. These strategies are possible only by either altering the elemental composition of the perovskite or by modifying the perovskite absorber with functional molecules with the purpose of making them less susceptible to moisture degradation.

Lead free perovskite photovoltaics as light harvesting semiconductors have not yet benefitted from the same intensive research effort that has propelled lead based perovskites from a power conversion efficiency of 3.8% to >20%. MAPI exhibits a number of remarkable properties that makes it an ideal contender for optoelectronic applications. The compound is a direct band-gap semiconductor with a room temperature band gap of 1.6 eV which is within the range of Shockley-Queisser gap for single junction cells [15]. Despite the processing advantages of perovskites, before the technology can be commercialized the poor stability of the organic-inorganic hybrid combinations with regard to the humidity, heat, light, and oxygen has to overcome. Recent reports have highlighted some innovative and elegant ideas which should be the main focus of future research for the design and practical applicability of photovoltaics materials [16]. Herein we highlight some recent advances in improving the chemical stability of perovskite materials by substitution of cation and anion elements. Our hope is to pave the way for the design of perovskites to realize the stable and reliable perovskite solar cells with unprecedented improvement in stability.

2. Photovoltaic effect

The absorption of photons with energy above the bandgap (hv > Eg) in a semiconducting material results the transfer of electrons from the valence band to the conduction band. In a particular material, the excited carriers will come back to the ground-state, with the energy being conserved by the emission of photons. The effect occurs when there is an asymmetric electric potential across the material and hence result the net flow of photogenerated charge carriers namely photocurrent. It is now possible to establish an asymmetric potential in a crystal such as p-n junction thereby giving a good rectification and hence better photovoltaic results. The good photovoltaic materials provide an opportunity to separate the charges as effectively as possible with minimal charge carrier relaxation by transporting them to the contacts and thus minimizing recombination between the electrons & holes. The overall power conversion efficiency represented by η of incident sunlight or power to electricity is directly proportional to the short circuit current (J_{sc}), open-circuit voltage (V_{oc}) and fill factor (FF). the overall equation can be written in mathematical form as:

$$\eta = \frac{J_{sc} V_{oc} FF}{P_{in}}$$

The potential difference developed across the cell when the terminals are not connected is known as open circuit voltage V_{oc} which depends upon the bandgap of the absorber layer. The Jsc is the short circuit photocurrent extracted when the voltage across the device is zero which depends upon the range of spectrum absorbed by the active layer in a device. The expected power at the maximum power point observed in J-V curve as a function of power is known as fill-factor.

3. Desired properties for best solar absorber

There are several key properties that generally benefit device efficiencies. Many of these properties are very difficult to measure experimentally, however these can be obtained relatively very cheaply from theoretical perspective. Here we highlight some of the key features which needs to be addressed during device fabrication.

a) Bandgap

The important property of a solar absorber is bandgap which determines the maximum theoretical power conversion efficiency. This is an intrinsic property and has eventually a direct influence on the actual performance of photovoltaic cell. The best solar cell efficiency can be achieved from the materials that possess band gap in the range of 1.1–1.56 eV. Bandgap is the property due to which we will be able to understand that whether the material is able to absorb the visible spectrum or not. How suitable the materials are for photovoltaic applications would be determined by how close the photon energy is to the bandgap of the material. One of the promising strategies to realize the absorption enhancement is the synthesis of solar cell devices by using the materials having the bandgap as quantified by well-known Shockley-Queisser limit [17]. However to achieve the maximum efficiency, the bandgap of around 1.3 eV would be highly advantageous [18].

b) Effective mass of charge carriers

Some key features for photovoltaics solar energy generation is strong solar absorption, low non-radiative carrier recombination rates and the ability to capitalize for years. One of the important features is reasonably high carrier mobility for the development of solar cell architecture as it decides the range of properties accessible by forming mixed compounds within a compatible material. High charge carrier mobility plays an important role to establish the separation of electron–hole to improve the device performance. The dispersion of band edges particularly envisages the mobility in a material which is theoretically quantified by the effective mass of a carrier giving rise to smaller effective mass and thereby improves the carrier mobility. This carrier mobility is halted by scattering defects, phonons and other charge carriers. However, mobility is not the only important property, but the lifetime of minority carriers have also been considered to be an essential parameter for novel photovoltaic materials because of their role in Shockley-Read-Hall recombination mechanism [19]. Lot of parameters are necessarily required to achieve better performance among which high mobility, diffusion length, and long carrier lifetime are at the top as for as organic–inorganic halide composition is concerned [20].

c) Optical absorption

Optical absorption is among the important parameters and is playing a vital role to the development of high efficiency solar cells. Lot of studies have investigated that how the light-absorption of solar cells can be enhanced by forming antireflective surface techniques [21]. All photovoltaic devices exhibit a certain absorption threshold, and the energy of photons incident on the surface below the threshold do not contribute significantly to electricity conversion. It is noteworthy a strong absorption that can be achieved in a material having a direct bandgap, however, the materials with indirect bandgap may also perform well if a direct transition of suitable energy is also available. Strong absorption is characterized by sudden change in the absorption coefficient. The absorption coefficient reduces below the band edge without any deep states [22]. The absorption coefficient along with the optical band gap and high power conversion efficiency makes materials promising candidates for novel solar cell applications. The knowledge of absorption coefficient in a particular region where the absorber seems to be active is of paramount importance. Concrete information about the absorption coefficient of material provides the advantage over conventional materials and hence allows the fabrication of a desirable and thin cell structure.

d) Ferroelectric and dielectric behavior

Electric response is also playing a vital role to photovoltaic absorber. Considerable efforts have been made to optimize the properties of materials for photovoltaic use within the aim of converting sunlight very efficiently to electrical energy. The process requires the effective absorption of solar radiation to create the separation of photo-excited energy carriers and hence reduce the charge recombination rate as low as possible. Ferroelectric property provides a viable route to separate charge carriers spontaneously and some noteworthy reports have also been published [23, 24]. However, most of the ferroelectric materials have wide bandgap (Eg > 2.8 eV in case of $BiFeO_3$ and Eg > 3.5 eV for Lead-Zirconate-Titanate) that is beyond the visible light spectrum region allowing the use of just a mere percentage (10–20%) of solar energy. However, the ferroelectric behavior perhaps offers most obvious benefit with regard to a high degree of charge screening, and inhibits radiative electron–hole recombination. Having large dielectric constant in ferroelectric materials enables smaller defect binding energies promoting shallow defect states. Thus ferroelectric behavior has been of considerable interest with regard to the hysteresis.

e) Defect tolerance

The physical properties of a material are generally dictated by impurities and defects. These imperfections exist fundamentally in two ways such as doping defects and impurities and create free carriers which enable charge recombination centers and charge scattering halts the mobility. Due to the strong interaction between the theory of defects and doping techniques, a lot of things have been understood about the physics and properties of defects. There are many routes that can be used to instill the defect tolerance in a compound and a specific approach can be adapted to design the device. From the application point of view an optimal material would combine the carrier concentrations with weak carrier scattering. The control on carrier concentration is the key factor in new generation quantum materials as the position of Fermi level which decides whether the specific band features are accessible. Recently, some compositions having ns^2 lone pair such as Bi^{3+} and Sn^{2+} have been reported, considered to be an excellent contenders with defect tolerance features [25].

4. Replacement of lead in perovskite structure

Concerns however have been raised about the possible environmental and legal problems associated with new designs and technology of lead based solar cell fabrication. Lead, as a matter of fact is one of the most studied materials in terms of its toxicity and is found to be hazardous in environment which damages the nervous system and can cause brain disorder. Therefore, lead is unquestionably a problem and the serious efforts are required to phase out lead from the technological materials. Without degrading the favorable photovoltaic properties by replacing lead in perovskite structures by a non-toxic or comparatively non-hazardous compared to lead would therefore be a topic of interest. In this regard, the possibility of replacing lead by different element will be explored by taking the consideration of Goldschmidt rule and some additional quantum mechanical properties. It is very important to consider a very serious parameter while replacing the natural minerals and keeping the crystal structure more or less unchanged is a difference of electronegativity [26]. In addition the formability of halide perovskites depends on some key requirements such as charge neutrality between cations and anions, stability of BX_6 octahedra and the ionic radii of A-site, B-site and the halide component. The octahedral stability can be understood by octahedral factor μ, which is the ratio between the ionic radii of B-site and halide component while as the Goldschmidt tolerance factor predicted by ionic radii derives the stability range of perovskite. Keeping these things in mind one can provide a conceptual toolbox towards replacing lead and some additional photo-physical properties of perovskite halides. Also this approach is exemplified by focusing on the ions having the ionic radii close to lead ion which should be non-toxic and relatively less expensive, of course without seriously degrading the overall performance of solar cells. Such replacement may be possible in the representative compound MAPI with comparable properties that suits the photovoltaics applications rather than single compound. Various efforts have been made to replace lead by using different ions having same or somehow near to the same ionic radii of lead which are mostly located in the immediate vicinity of lead in the periodic table. This suggests that they could be expected to have naturally a similar electronic structure. Many studies focused on the optimization of materials by testing alternatives at lead site and more than hundred unique combinations have been considered which form stable halide salts. **Figure 2** shows the combination of different solar photovoltaic absorbers used to improve the efficiency along with the stability. Thus an outstanding performance is based on the exceptional properties of halide perovskites exhibiting balanced electron–hole concentration, high absorption coefficient, direct and tunable bandgap, high charge carrier mobilities, and long carrier diffusion lengths etc.

Thus the current limitations impeding the commercialization of lead-based halide perovskite are now well known. These shortcomings are currently tackled by flood of research worldwide by using restless efforts from various research groups around the world to achieve good progress in the field. The stability issue was resolved by introducing the changes in the composition by mere loss of 5% of the initial power conversion efficiency [27]. However the toxicity issue is still an unsolved problem and many research groups took up the challenge to try the substitute of lead with other elements to solve the pending issues to make the materials stable, efficient and environmentally reliable. Therefore, some modifications

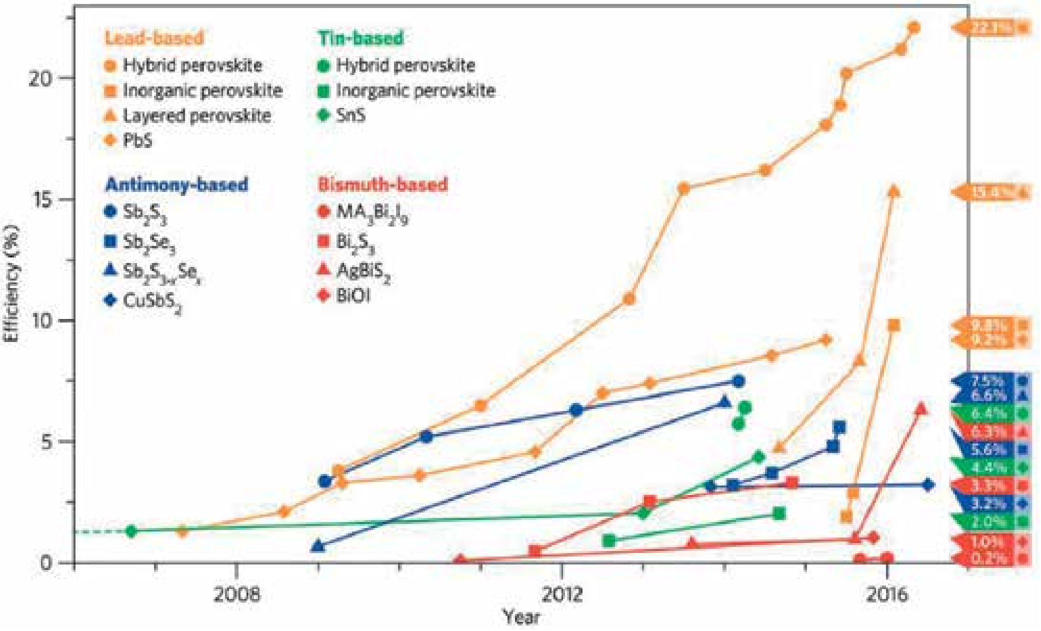

Figure 2. Improvement in the efficiency of different solar absorbers with years. [*Source*: Ref. 18].

of the well renowned MAPI compound must have the ability to increase the stability of the compound have become highly desirable. Depending upon the nature of the ions within the perovskite structure, a range of different divalent metal cations such as Pb^{2+}, Ge^{2+}, Ca^{2+}, Ba^{2+}, Cu^{2+}, Sr^{2+}, Fe^{2+}, Pd^{2+}, Sn^{2+}, Eu^{2+}, and Mg^{2+} have already been investigated at B-site of hybrid halide perovskites. By comparing the ionic radius for metallic cations with the oxidation state of +2 and after filtering with an ionic radius Pb^{2+}, as in 6-coordinated systems according to Shannon, only nine elements are found to be feasible to substitute for Pb in perovskite structure. To avoid the mixed oxidation state, structural frustration and formation of vacancies in the structure, only three elements are perhaps found the perfect possibility to substitute for lead i.e. Ba^{2+}, Ca^{2+} and Sr^{2+}. The corner sharing of BX_6 octahedra forms a three dimensional network in perovskite structure in which A-site cations occupy the 12-fold coordination to maintain the charge neutrality which is an important parameter for the stability of structure.

The most obvious choice for lead replacement is to see the group 14 metal, such as Sn or Ge and would be an important and fruitful development. Owing to their optical bandgap in the red or infrared region with outstanding carrier mobilities, these materials may constitute promising optoelectronic applications. Consequently the record efficiency for tin based halide perovskite lags behind that of lead halide perovskite. The low energy formation of tin based perovskite is because the oxidation state of tin transfers from +2 to +4 oxidation state upon exposure to ambient conditions, a transformation that does not occur easily in lead perovskites [28]. It was also noticed that tin perovskite had to be performed in nitrogen atmosphere to avoid the quick degradation of the samples. The tin based perovskites have also proved problematic making it difficult to achieve high device fill factor due to high rates of defect-mediated charge carrier recombination. Therefore, it is interesting to find other perovskite which may be more stable and reliable at ambient conditions for photovoltaic device fabrication. Beyond that, tin halide perovskites offer a variety of properties which make them attractive for use in photovoltaics provided the challenge with stability, including narrow bandgap, binding energies, and high charge mobilities than lead halides can be addressed.

The reports suggest that alkaline-earth metals such as magnesium, strontium, barium, calcium etc. can have the potential as substitutes to form perovskite structures due to their suitable ionic radii, abundance on the earth, +2 stable oxidation states similar to Pb^{2+} except toxicity [29]. The simulations performed very recently reveals that Mg^{2+} can replace lead in the structure by forming magnesium halide perovskites with optimum absorption, direct tunable bandgap within visible spectrum and low effective mass [30]. The bandgap has been found to be tunable by introducing different A-site cations. Despite the smaller ionic radius of Mg^{2+} compared to lead, theoretical calculations predicted the stable halide perovskite structure [30]. Since magnesium based halide perovskite structures have not been explored as absorbing materials in solar photovoltaics yet, therefore, this composition requires some special attention.

It is well known that Ba^{2+} has an ionic radius slightly larger than Pb^{2+} and accordingly will also have a slight variation in the tolerance factor of compositions such as $CH_3NH_3BaI_3$ and $CH_3NH_3PbI_3$. However, the density functional theory (DFT) calculations have predicted that stable Ba based perovskite materials have bandgap of 3.3 eV which is quite large as compared to Pb based compounds (1.57 eV). The reports suggest that the high bandgap is a reason of low electronegativity and low work function [29]. Also these halide perovskites have an issue of synthetic conditions due to their moisture sensitivity which hampers their synthesis formation, characterization and in particular their photovoltaic applications [30].

The best materials among the non-toxic, abundant and low cost alkaline-earth metal is none other than calcium (Ca^{2+}) with an ionic radius almost similar to lead (Pb^{2+}) and hence may be capable of filling the void as non-toxic element in halide perovskite structure [30]. However, as reported earlier, the high bandgap, instability in humid conditions, and less mobility hampers the calcium to be a suitable material for photovoltaics applications [31].

One of the obvious implementation has been done to find a lead free absorber in meso-structured perovskite solar cells such as $CsGeI_3$ and $CH_3NH_3GeI_3$. However, the power conversion efficiency values were observed to be 0.11 and 0.20% respectively [32]. After some competitive efforts made to improve the efficiency in germanium based perovskites, a power conversion efficiency of approximately 3% in meso-structured cell architecture were claimed. The value is still much less compared to the theoretically possible PCE of >27% as predicted by Qian et al. [33]. Various efforts are still on the way to improve the efficiency of the said perovskites, however, for promising photovoltaic applications and full potential of the Ge based materials is by far not fully exploited yet.

Strontium is fairly a nontoxic and highly abundant metal on earth making it relatively an inexpensive with ionic radii almost similar to lead suggesting that exchange could be possible without affecting the crystal structure. Density functional theory revealed that strontium perovskite such $CH_3NH_3SrI_3$ has similar bonding patterns leading to be a stable phase, despite the difference of electronegativity between lead and strontium [34]. The electronic properties of both Sr. and lead based halide perovskites revealed by simulation suggests that strontium has higher degree of ionic interaction as a consequence of lower electronegativity of strontium. This lower electronegativity together with the missing d-orbitals in the valence of Sr^{2+} is responsible for higher bandgap of around 3.6 eV. This is the main hurdle in Sr. based halide-perovskite that limits its possible application as an absorber material in photovoltaics technology. Another crucial issue related to $CH_3NH_3SrI_3$ is the poor stability at ambient conditions due to its hygroscopic nature.

Transition metal halide and oxide perovskite structures were studied extensively over the decades particularly of their electronic and magnetic transport, magnetic properties, phase transitions and particularly of their high abundance [35–39]. As for as the transition metal oxides/halide perovskites are concerned with regard to their optoelectronic applications, various alternatives of lead-free transition metal perovskites have been predicted to be promising replacement candidates, however, the problems associated to their chemical stability, ionic radii hinders their functionality for photovoltaics. The factors responsible for the low photovoltaic performance from copper halide perovskites are low absorption coefficient, intrinsically low conductivity and high effective mass of holes. The small ionic radii of divalent iron metal (Fe^{2+}) cation compared to lead effectively hinders the formation of three dimensional structures. Several compositions of iron halide perovskites have been studied with regard to their magnetic properties, very few research groups pay attention to the optical properties. The drawback that limits the stability of iron is its multiple oxidation states which follow the same trend like germanium and tin based perovskites. Therefore a lot of survey is required by iron halide to find its applicability as an absorber for photovoltaic applications.

Rare-earth ions have been investigated in terms of optical applications such as Eu^{2+}, Yb^{2+}, Tm^{2+}, but the applicability of these materials in optoelectronic devices is limited due to their sensitivity towards moisture. Since the photovoltaic properties of lanthanides and actinides still have not been explored, however it is expected that these families may have some interesting optical properties and might be the potential absorbers for photovoltaic devices.

The most exciting developments have been initiated in the materials science of new halide perovskites with an emphasis on alternatives to lead. In the recent developments of new perovskites and perovskite-related materials was found that double perovskites have a potential to touch the new heights in the development of photovoltaic research [40]. Recently, various groups have started to work on double perovskite structures particularly on Cs_2AgBiX_6 (CABX) family. The photoluminescence behavior of CABX has been studied by Slavney et al. and observed long decay time of the sample as reported in MAPI with an indirect bandgap of 1.95 eV which altogether is an attribute of long recombination lifetime [41]. The group also revealed stability of compound above room temperature after incorporated with bromide up to several days. A wide theoretical screening has been done using DFT calculations and observed that Ag compounds have higher bandgap while Au shares the lowest. The compounds such as Cs_2AgSbI_6, $Cs_2BiAuBr_6$ and Cs_2BiCuI_6 are those observed to have bandgap within the optimal range [42]. It is clear that double perovskite structures allows us to replace the lead in the composition, however, their stability issue and high indirect bandgap may be a big issue to be resolved before their practical application in photovoltaic technology.

5. Modifications for better and possible photovoltaic materials

The instability with respect to the phase separation of MAPI due to the low formation energy has garnered significant attention to modify the compound in a way to increase the stability due to its record breaking efficiency. However, there are growing concerns surrounding its toxicity and long term stability. Here we will discuss about the other possibilities with the aim of identifying those combinations that will likely to achieve stable and high efficiency.

The method of turning the electronic properties of MAPI is by changing the organic cation. However, the formamidinium as a successful replacement for methylammonium has rather complicated the phase formation while its large bandgap adversely affects the device performance [43]. Instead of using organic cation, inorganic cation can be a best alternative to produce a compound an all-inorganic which may have some possibility to increase the stability. Various attempts made to replace A-site with other organic/inorganic cations have almost proved to be very challenging and difficult. Therefore, to introduce the inorganic cation at A-site by achieving a high efficiency will be a remarkable step towards the stability of perovskite photovoltaics. The tuning of stability and optical properties of a material can play a crucial role to enable the device moisture tolerant with exceptional absorbing characteristics.

The bandgap along with effective mass tuning is possible by replacing the ions in the structure. By replacing the organic part of perovskite structure may be more promising than inorganic one. It has been reported earlier that replacing the methyl ammonium content slightly with formamidinium ion in lead based perovskites can decrease the bandgap somehow and there are also some theoretical arguments which suggest that smaller cation could reduce the bandgap [44]. Therefore, the bandgap of strontium based perovskite may be reduced if the organic cation would be replaced by inorganic cation or changing the cation size will directly affect the geometrical changes such as tolerance factor and octahedral tilting. Since, inorganic counterpart such as Cesium is a best cation that can replace the organic part in the structure, but experimental evidence reveals that there is a problem related to the solubility of Cesium. Although a replacement of organic cation may decrease the bandgap which is the most crucial part to achieve the high performance of perovskites for solar cell applications. Thus the rise and emergence of hybrid perovskite (MAPI) has stimulated the photovoltaic research community. The only material till date is considered to be a third generation solar absorbing material that has a potential to effectively be an alternative to silicon technology. This material clearly possesses the property combinations that demonstrate the potential of polar materials for solar energy conversion.

6. Conclusion

The approach of utilizing Goldschmidt's rules together with additional quantum mechanical considerations can provide a promising route towards replacing lead, as well as providing general insights into the photovoltaics technology of metal halide-perovskites. The materials other than lead-halide perovskites appear to be more stable and exhibit some good functionalities, however the overall power conversion efficiency of these materials is low. Therefore it is very interesting to focus on the optoelectronic properties of the lead free materials in order to achieve the environmental friendly and stable photovoltaic perovskite devices. It is noteworthy that tin based solar absorbers and the group 14 metals have similar electronic properties, but still lead based devices outperform their tin based counterparts due to the oxidation of tin which leads to the efficiency loss. Several materials show some excellent solar absorbing property but they still require some development in their optical and environmental tolerant properties before they can reach to the comparable efficiencies. Therefore, it would be consequently from both toxicological, marketing and more importantly from legal perspective very beneficial if we succeed to replace the lead in perovskite solar cells without seriously degrading their overall performance. However, the lead free material combinations with robust optoelectronic properties with perfect stability at ambient conditions cannot be ruled out in near future.

Acknowledgements

The author Dr. Hilal Ahmad Reshi is grateful to Mr. Farooq Hussain Bhat, Head, department of Physics, and Prof. M. A. Siddiqi, Honorable VC-IUST, Awantipora Kashmir for all sorts of moral and technical support throughout this tenure. Dr. Hilal is also thankful to his mentors Dr. Vilas Shelke, Novel Materials Research Laboratory, Department of Physics, Barkatullah University, Bhopal, Madhya Pradesh and Prof. S. K. Sarkar, Devices and Interfaces Lab, Energy Science and Engineering department, IIT-Bombay, Mumbai Maharashtra for useful discussion and suggestions.

Author details

Hilal Ahmad Reshi* and Rayees Ahmad Zargar

*Address all correspondence to: hilal.phy@gmail.com

Department of Physics, Islamic University of Science and Technology, Awantipora, Kashmir, India

References

[1] IEA. Energy Technology Perspectives (ETP). Paris: OECD/IEA; 2014

[2] Pfann WG, Van Roosbroeck W. Radioactive and photoelectric p-n junction power sources, Journal of Applied Physics 1954;**25**:1422-1434, Doi:10.1063/1.1721579

[3] IEA, Technology Roadmap. Solar Photovoltaic Energy. Paris: OECD/IEA; 2010

[4] Green MA, Emery K, Hishikawa Y, Warta W, Dunlop ED. Solar cell efficiency tables (version 42). Progress in Photovoltaics; Research and Applications. 2013;**21**:827-837

[5] Green MA. Silicon solar cells: State of the art. Philosophical Transactions of Royal Society A. 2013;**371**:20110413-20110414. DOI: 10.1098/rsta.2011.0413

[6] Galasso FS, Smoluchowski R, Kurti N, Structure, Properties and Preparation of Perovskite Type Compounds, International Series of Monographs in Solid State Physics. 1st ed., Pergamon: London, 1969. 220 p. ISBN: 9781483146027

[7] Service RF. Solar energy. Outlook brightens for plastic solar cells. Science. 2011;**332, 6027**(293):293. DOI: 10.1126/science.332

[8] Snaith HJ. Perovskites: The emergence of a new era foe low cost, high efficiency solar cells. Journal of Physical Chemistry Letters. 2013;**4**:3623-3630. DOI: 10.1021/jz4020162

[9] Lee MM, Teuscher J, Miyasaka Y, Murakami TN, Snaith HJ. Efficient hybrid solar cells based on meso-superstructured organometal halide perovskites. Science. 2012;**338**:643-647. DOI: 10.1126/science.1228604

[10] Kim HS, Lee CR, Im JH, Lee KB, Moehl T, Marchioro A, Moon SJ, Baker RH, Yum JH, Moser JE, Gratzel M, Park NG. Solid state submicron thin film mesoscopic solar cell with efficiency exceeding 9%. Scientific Reports. 2012;**2**:591-597. DOI: 10.1038/srep00591

[11] Saliba M, Matsui T, Seo JY, Domanski K, Correa-Baena JP, Nazeeruddin MK, Zakeeruddin SM, Tress W, Abate A, Hagfeldt A, Gratzel M. Cesium-containing triple cation perovskite solar cells: Improved stability, reproducibility and high efficiency. Energy Environment of Science. 2016;**9**:1989-1997. DOI: 10.1039/c5ee03874j

[12] Yang WS, Noh JH, Jeon NJ, Kim YC, Ryu S, Seo J, Seok SL, Cells S. High-performance photovoltaic perovskite layers fabricated through intermolecular exchange. Science. 2015;**348**:1234-1237. DOI: 10.1126/science.aaa9272

[13] Mitzi DB, Field CA, Harrison WTA, Guloy AM. Conducting tin halides with a layered organic based perovskite structure. Nature. 1994;**369**:467-469. DOI: 10.1038/369467a0

[14] Science news, newcomer juices up the race to harness sunlight. Science. 2013;**342**:1438-1439. DOI: 10.1126/science.342.6165.1438-b

[15] DInnocenzo V, Grancini G, Alcocer MJP, Kandada ARS, Stranks SD, Lee MM, Lanzani G, Snaith HJ, Petrozza A. Excitons versus free charges in organo-lead tri-halide perovskites. Nature Communications. 2014;**5**:3586-3586. DOI: 10.1038/ncomms4586

[16] Srivastava R. Perovskite as light harvester: Prospects, efficiency, pitfalls and roadmap. In: Das N, editor. Nanostructured Solar Cells. InTech; 2017. DOI: 10.5772/65052

[17] Shockley W, Queisser HJ. Detailed balance limit of efficiency of p-n junction solar cells. Journal of Applied Physics. 1961;**32**:510-519. DOI: 10.1063/1.1736034

[18] Ganose AM, Savory CN, Scanlon DO. Beyond methylammonium lead iodide: Prospects for the emergent field of ns^2 containing solar absorbers. Chemical Communications. 2017;**53**:20-44. DOI: 10.1039/C6CC06475B], 10.1039/C6CC06475B]

[19] Jaramillo R, Sher MJ, Ofori-Okai BK, Steinmann V, Yang C, Hartman K, Nelson KA, Lindenberg AM, Gordon RG, Buonassisi T. Transient terahertz photoconductivity measurements of minority-carrier lifetime in tin sulfide thin films: Advanced metrology for an early stage photovoltaic material. Journal of Applied Physics. 2016;**119**:035101. DOI: 10.1063/1.4940157

[20] Stranks SD, Eperon GE, Grancini G, Menelaou C, Snaith MJ. Electron-hole diffusion lengths exceeding 1 micrometer in an organometal trihalide perovskite absorber. Science. 2013;**342**:341-344. DOI: 10.1126/science.1243982

[21] Yu P, Chang CH, Chiu CH, Yang CS, Yu JC, Kuo HC, Hsu SH, Chang YC. Efficiency enhancement of GaAs photovoltaics employing antireflective indium tin oxide nanocolumns. Advanced Materials. 2009;**21**:1618-1621. DOI: 10.1002/adma.200802563

[22] Xing G, Mathews N, Sun S, Lim SS, Lam YM, Gratzel M, Mhaisalkar S, Sum TC. Long range balanced electron and hole-transport lengths in organic-inorganic $CH_3NH_3PbI_3$. Science. 2013;**342**:344-347. DOI: 10.1126/science.1243167

[23] Choi WS, Chisholm MF, Singh DJ, Choi T, Jellison GE. Wide bandgap tenability in complex transition metal oxides by site-specific substitution. Nature Communications. 2012;**3**:689-686. DOI: 10.1038/ncomms1690

[24] Grinberg I, West DV, Torres M, Gou G, Stein DM, Wu L, Chen G, Gallo EM, Akbashev AR, Davies PK, Spanier JE, Rappe AM. Perovskite oxides for visible light absorbing ferroelectric and photovoltaic materials. Nature. 2013;**503**:509-512. DOI: 10.1038/nature12622

[25] Brandt RE, Stevanovic V, Ginley DS, Buonassisi T. Identifying defect-tolerant semiconductors with high minority carrier lifetimes: Beyond hybrid lead halide perovskites. MRS Communication. 2015;**5**:265-275. DOI: 10.1557/mrc.2015.26

[26] Ringwood AE. The principles governing trace elements distribution during magmatic crystallization part 1: The influence of electronegativity. Geochimica et Cosmochimica Acta. 1955;**7**:189-202. DOI: 10.1016/0016-7037(55)90029-6

[27] Saliba M, Matsui T, Domanski K, Seo JY, Ummadisingu A, Zaheeruddin SM, Correa-Baena JP, Tress WR, Abate A, Hagfeldt A, Gratzel M. Incorporation of rubidium cations into perovskite solar cells improves photovoltaic performance. Science. 2016;**354**:206-209. DOI: 10.1126/science.aah5557

[28] Pyykko P. Relativistic effects in structural chemistry. Chemical Reviews. 1988;**88**:563-594. DOI: 10.1021/cr00085a006

[29] Pazoki M, Jacobsson TJ, Hagfeldt A, Boschloo G, Edvinsson T. Effect of metal cation replacement on the electronic structure of metalorganic halide perovskites: Replacement of lead with alkaline-earth metals. Physical Review B Condensed Matter and Material Physics. 2016;**93**:144105-144110. DOI: 10.1103/PhysRevB.93.144105

[30] Filip MR, Giustino F. Computational screening of homovalent lead substitution in organic-inorganic halide perovskites. Journal of Physical Chemistry C. 2016;**120**:166-173. DOI: 10.1021/acs.jpcc.5b11845

[31] Uribe JI, Ramirez D, Osorio-Guillen JM, Osorio J, Jaramillo F. CH3NH3CaI3 perovskite: Synthesis, characterization, and first principles studies. Journal of Physical Chemistry C. 2016;**120**:16393-16398. DOI: 10.1021/acs.jpcc.6b04207

[32] Krishnamoorthy T, Ding H, Yan C, Leong WL, Baikie T, Zhang Z, Sherburne M, Li S, Asta M, Mathews N, Mhaisalkar SG. Lead-free germanium iodide perovskite materials for photovoltaic applications. Journal of Materials Chemistry A. 2015;**3**:23829-23832. DOI: 10.1039/C5TA05741H

[33] Qian J, Xu B, Tian W. A comprehensive theoretical study of halide perovskites ABX_3. Organic Electronics. 2016;**37**:61-73. DOI: 10.1016/j.orgel.2016.05.046

[34] Jacobsson TJ, Pazoki M, Hagfeldt A, Edvinsson T. Goldschmidt's rules and strontium replacement in lead halogen perovskite solar cells: Theory and preliminary experiments on $CH_3NH_3SrI_3$. Journal of Physical Chemistry C. 2015;**119**:25673-25683. DOI: 10.1021/acs.jpcc.5b06436

[35] Reshi HA, Singh AP, Pillai S, Para TA, Dhawan SK, Shelke V. X-band frequency response and electromagnetic interference shielding in multiferroic $BiFeO_3$ nanomaterials. Applied Physics Letters. 2016;**109**:142904-142904. DOI: 10.1063/1.4964383

[36] Needham GF, Willett RD, Franzen HF. Phase transitions in crystalline models of bilayers. 1. Differential scanning calorimetric and x-ray studies of $(C_{12}H_{25}NH_3)2MCl_4$ and $(NH_3C_{14}H_{29}NH_3)2MCl_4$ salts (M = Mn2+, Cd2+, Cu2+). The Journal of Physical Chemistry. 1984;**88**:674-680. DOI: 10.1021/j150648a012

[37] Reshi HA, Pillai S, Bhuwal D, Shelke V. Nanostructure induced metal-insulator transition and enhanced low-field magnetoresistance in $La_{0.7}Sr_{0.3}MnO_3$ systems. Journal of Nanoscience and Nanotechnology. 2013;**13**:4608-4615. DOI: 10.1166/jnn.2013.7136

[38] Reshi HA, Pillai S, Yadav RS, Para TA, Deshpande UP, Shripathi T, ShelkeV. Kondo-like electronic transport and ferromagnetic cluster-glass behavior in $La_{0.7}Sr_{0.3}MnO_3$ nanostructures. RSC Advances. 2015;**5**:85950-85956. DOI: 10.1039/c5ra12042j

[39] Boix PP, Agarwala S, Koh TM, Mathews N, Mhaisalkar SG. Perovskite solar cells: Beyond methylammonium lead iodide. Journal of Physical Chemistry Letters. 2015;**6**:898-907. DOI: 10.1021/jz502547f

[40] Giustino F, Snaith HJ. Towards lead-free perovskite solar cells. ACS Energy Letters. 2016;**1**:1233-1240. DOI: 10.1021/acsenergylett.6b00499

[41] Slavney AH, Hu T, Lindenberg AM, Karunadasa HI. A bismuth-halide double perovskite with long carrier recombination lifetime for photovoltaic applications. Journal of the American Chemical Society. 2016;**138**:2138-2141. DOI: 10.1021/jacs.5b13294

[42] Volonakis G, Filip MR, Haghighirad AA, Sakai N, Wenger B, Snaith HJ, Giustino F. Lead-free halide double perovskites via heterovalent substitution of noble metals. Journal of Physical Chemistry Letters. 2016;**7**:1254-1259. DOI: 10.1021/acs.jpclett.6b00376

[43] Amat A, Mosconi E, Ronca E, Quarti C, Umari P, Nazeeruddin MK, Gratzel M, De Angelis F. Cation-induced bandgap tuning in organohalide perovskites: Interplay of spin-orbit coupling and octahedra tilting. Nano Letters, 2014;**14**:3608-3616. DOI: 10.1021/nl5012992

[44] Walsh A. Principles of chemical binding and band gap engineering in hybrid organic-inorganic halide perovskites. Journal of Materials Chemistry C. 2015;**119**:5755-5760. DOI: 10.1021/jp512420b

Edited by Ruby Srivastava

The book "Recent Developments in Optoelectronic Devices" is about the latest developments in optoelectronics. This book is divided into three categories: light emitting devices, sensors, and light harvesters. This book also discusses the theoretical aspects of device design for iridium complexes as organic light emitting diodes (OLEDs), strategies for developing novel nanostructured materials, silicon-rich oxide (SRO) electroluminescent devices, and multifunctional optoelectronic devices developed on resistive switching effects. The worldwide participation of authors has contributed to the unifying effect of science. Furthermore, interested readers will also find information on the screen printed technology using semiconductor devices, nonlinear phenomena in quantum devices, experimental set up of optoelectronics flexible logic gate to realize logic operations, autonomous vehicles, and the latest developments in perovskites as solar cells.

Published in London, UK

IntechOpen

ISBN 978-1-83881-672-8